Alma Mater Studiorum · Università di Bologna

**Scuola di Scienze**
**Dipartimento di Fisica e Astronomia**
**Corso di Laurea Magistrale in Fisica**

# Electronic properties of Transition Metal Oxide layers for applications in organic solar cells

**Relatore:**
**Prof.ssa Daniela Cavalcoli**

**Correlatore:**
**Prof.ssa Nadine Witkowski**

**Presentata da:**
**Chiara Labanti**

Anno Accademico 2017/2018

# Abstract

Transition Metal Oxides, like Molybdenum and Titanium oxides, are highly promising materials to develop applications in solar cell production as charge transport layers.

This thesis presents a work developed between the Physics and Astronomy Department of the University of Bologna and the Institute of the NanoSciences of Paris (INSP) at Sorbonne University - Paris 6 in collaboration with the University of Southern Denmark, which aimed at understanding and tailoring oxide properties in order to improve electron and hole transport in thin films.

The performed experiments involved both structural characterization with Atomic Force Microscopy (AFM) and electrical and chemical studies, like Kelvin Probe Force Microscopy (KPFM), X-ray and Ultraviolet Photoelectron Spectroscopy (XPS/UPS) as well as X-ray Photoemission Electron Microscopy (XPEEM) realized during a beamline session at SOLEIL synchrotron facility in Saint-Aubin (France).

The main results of this research include the identification of surface evolution with grain growth for molybdenum oxide deposited on silicon, the stability of Mo and Ti oxides on Indium Tin Oxide (ITO) inferred from a lower number of grains in AFM maps, the increase of work function when materials undergo cycles of annealing treatment up to 450°C and the interesting appearance of domains of polycrystallites on titanium oxide surface after heating.

Different analyses carried out under illumination allowed to investigate the effects of Ultraviolet and X-ray beam exposure and to identify the oxide deposition techniques and the sample characteristics which are more suitable to reduce electrical property degradation due to light damage.

# Sommario

Gli Ossidi di Metalli di Transizione, come quelli di Molibdeno e di Titanio, sono materiali molto promettenti per lo sviluppo di applicazioni per il trasporto di carica nella fabbricazione di celle solari.

Questa tesi presenta un lavoro realizzato tra il Dipartimento di Fisica e Astronomia dell'Università di Bologna e l'Istituto delle NanoScienze di Parigi della Sorbona - Paris 6 in collaborazione con la Southern Denmark University, che mira a comprendere e modificare le proprietà di tali ossidi per il miglioramento del trasporto di elettroni e lacune in film sottili.

Il progetto di ricerca è stato portato a termine ricorrendo a varie tecniche di caratterizzazione strutturale, come la Microscopia a Forza Atomica (AFM), elettrica e chimica, tra cui la Microscopia Kelvin Probe (KPFM), la Spettroscopia di Fotoemissione a Raggi X e Ultravioletti (XPS/UPS) e la Microscopia a Fotoemissione di Elettroni a Raggi X (XPEEM) realizzata presso la sorgente di sincrotrone SOLEIL di Saint-Aubin (Francia).

I principali risultati di questo studio includono l'identificazione dell'evoluzione della superficie con la crescita di grani per l'ossido di molibdeno su silicio, la stabilità degli ossidi di molibdeno e titanio su Ossido di Indio e Stagno (ITO) dedotta dal minor numero di aggregati visibili nelle mappe AFM, l'aumento della funzione lavoro quando i materiali sono sottoposti a cicli di riscaldamento (*annealing*) fino a 450°C e l'interessante comparsa di domini di policristalliti sulla superficie dell'ossido di titanio ad alta temperatura.

Differenti analisi con esposizione a radiazioni hanno permesso di investigare gli effetti di luce ultravioletta e raggi X sugli ossidi e di identificare la tecnica di deposizione e le caratteristiche dei materiali più adatte per ridurre la degradazione delle proprietà elettriche causate dalla luce.

# Acknowledgements

This work would not have been possible without the guide of my supervisor and co-supervisor, Prof. Daniela Cavalcoli and Nadine Witkowski, and the precious collaboration of all the researchers, lab technicians and doctoral students in Paris and Bologna who have helped me to handle new investigation techniques and overcome problems and difficulties during the experiments.

In particular I want to thank Hervé Cruguel, Sébastien Royer, Erwan Dandeu of the Institute of the NanoSciences of Paris, Christophe Méthivier of the Laboratory of Surface Reactivity of Sorbonne University, Stefan Stanescu, Sufal Swaraj, Adrien Besson, Brice Sarpi and Rachid Belkhou for the reliable and kind support on HERMES beamline, Mehrad Ahmadpour and Prof. Morten Madsen of the University of Southern Denmark for the essential partnership in sample fabrication and measurements at SOLEIL synchrotron and Maria Antonietta Fazio and Tobias Cramer of the Physics and Astronomy Department at the University of Bologna.

This thesis has been developed in the context of an Erasmus+ exchange project and I would like to remember all the academic and administrative staff who made it possible and gave me the opportunity to enlarge my horizons and building new skills in an international environment, especially Prof. Enrico Campari and Prof. Max Marangolo, coordinators of Bologna-Paris relationships.

My gratitude is also addressed to all the people who welcomed and supported me during my stay in Paris, especially the nuns of the Foyer de la Jeune Fille.

Finally, a special thank to my family and friends because they have always trusted in me during all my study career and have remembered me my capabilities even when difficulties made it tough to continue working with passion.

# Contents

# Introduction

Recent years have seen a growing development of Transition Metal Oxide use in photoelectronic technology due to an adaptable energy band structure, suitable for coupling with other materials in multi-layered device structures.

In particular, this thesis is focused on the application of these compounds in organic and hybrid photovoltaic cells, in which they are used as buffer layers in order to assist hole or electron transport and extraction. The wide variety of their electronic properties, such as Work Function, make it possible to choose proper candidate materials for different organic semiconductors employed as active layers in solar cells.

Even though a well-established theoretic knowledge of Transition Metal Oxide crystalline and electronic structure is available[1][2] and some specific compounds - as Titanium Oxide $TiO_2$ [3][4] - have been thoroughly analyzed by several experimental methods, a lack of data is still present in the case of other ones - like Molybdenum Oxide $MoO_3$, investigated by a limited number of studies[5][6].

The aim of this work is a deeper comprehension of charge transport characteristics of Titanium and Molybdenum Oxides, by means of different measurement techniques, in order to relate hole and electron conduction to sample morphology and to understand how synthesis procedures and post-growth treatments can enhance their performances as buffer layers.

After *Chapter 1*, which generally illustrates physics and chemistry of Transition Metal Oxides as well as their use for charge extraction in solar cells, and *Chapter 2*, presenting theoretic background and previous experimental results on them, *Chapter 3* provides an explanation of the deposition techniques the considered samples were synthesized by.

Subsequently, *Chapter 4* introduces the electronic, chemical and structural characterization methods by means of which the research was carried out.

The full set of experimental results on Molybdenum and Titanium Oxides are separately displayed and analyzed in *Chapter 5*, with a further classification by experimental technique.

Finally, *Chapter 6* offers a general conclusion and suggests future development directions for the topic.

The work is completed by additional details on Kelvin Probes Force Microscopy experiments: *Appendix A* compares various operation modes, whereas *Appendix B* is an insight into boundary effects and adhesion measurements.

# Chapter 1

# Physics and applications of Transition Metal Oxides

## 1.1 Energy Level Alignment in organic electronic devices

A really promising and fast developing research field in condensed matter Physics is the theoretical study and realization of organic electronic devices, such as organic light-emitting diodes (OLEDs), organic photovoltaic cells (OPVs) and organic field-effect transistors (OFETs). Improving the performances of these technologies is the present challenge that many scientists are trying to overcome. In particular, one of the main features of organic electronic devices is the multi-layered structure with a succession of several interfaces, which determines the creation of as many energy barriers. The ability to reduce them in order to allow charge carriers to flow easily in the device is crucial to achieve a high performance technology in this field.

This thesis especially focuses on molybdenum and titanium oxides for organic photovoltaic applications. These materials, proving suitable for charge-extracting layers in OPVs, belong to a wider class of compounds, called Transition Metal Oxides (TMOs), spanning a broad range of work functions (WF) and other crucial physical properties for attaining a low power consumption in interface barriers.

In fact, electrical resistance at interfaces depends on energy level alignment (ELA) at the contact between the two compounds, typically a conductive electrode and an organic semiconductor. We can refer to the Fermi level of the former both as donor and as acceptor level, whereas in the latter we should distinguish between the highest occupied molecular orbital (HOMO), which plays the role of donor, and the lowest unoccupied molecular orbital (LUMO), which instead constitutes the acceptor level.

In an OPV simple configuration there is only an active organic semiconductor junction, where charge carriers are produced, contacted on both sides by two metallic electrodes, the hole-collecting and the electron-collecting ones, extracting charges from HOMO donor and LUMO acceptor states respectively, as shown in figure 1.1. In the regime of nonreactive or weakly reactive interfaces[1], when no hybridization between electrode and organic orbitals is present, energy alignment only depends on electrode work function and semiconductor HOMO and LUMO levels: as visible in figure 1.2, in a specific WF range there is a linear proportionality between the work functions of electrodes and the energy barrier carriers should overcome, so that this regime is called of *vacuum-level*

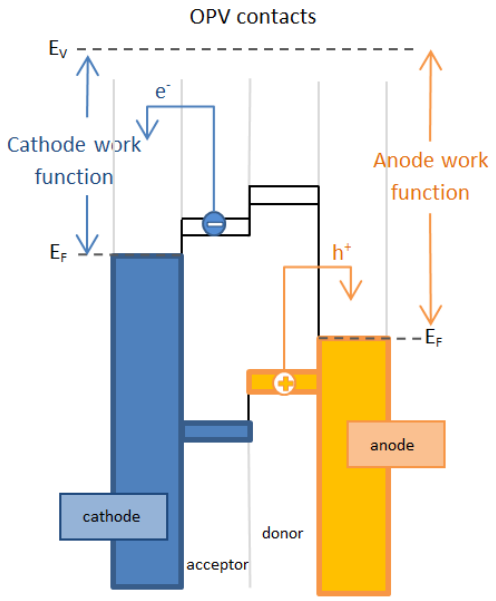


Figure 1.1: Energy band scheme for an OPV device: the active layers, with a *p*-*n* junction (acceptor and donor semiconductors), in contact with two metallic electrodes (cathode and anode). The arrows represent the charge flow, respectively from the acceptor LUMO level to the cathode Fermi energy $E_F$ and from the donor HOMO level to the anode $E_F$ for electrons and holes. Electrode work functions are defined as the energy differences between metallic $E_F$ and vacuum level $E_V$ (after [1]).

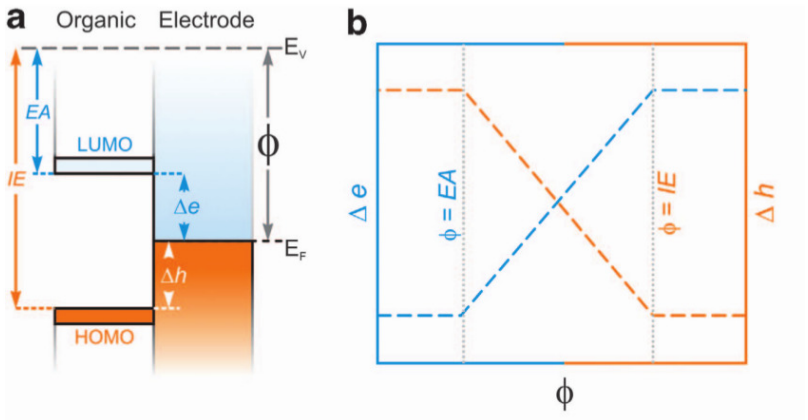


Figure 1.2: (a) Energy band scheme for an organic SC/metallic electrode interface, with indications of HOMO, LUMO, ionization energy (IE) and electron affinity (EA) of organic side; Fermi level ($E_F$) and work function ($\Phi$) of the metallic one; vacuum level ($E_V$), hole- and electron-injection barriers ($\Delta$h and $\Delta$e) of the system. (b) Graph of the relation between electrode work function $\Phi$ and hole-/electron-injection barrier. In the central region of *vacuum-level alignment* the energy needed by holes (electrons) to overcome potential barrier at the interface linearly decreases (increases) as $\Phi$ grows. When electrode work function gets higher (lower) than *Fermi level pinning* threshold, $E_F$ of the system equals SC ionization energy (electron affinity) and charge-injection barriers become constant (from [1]).

*alignment*[1] - even if respective vacuum levels are not always totally aligned.

In this context, when electrode work function is higher (lower) than a specific threshold, HOMO (LUMO) level of the organic molecules keeps being aligned with metallic $E_F$, regardless of any further increase (decrease) of electrode work function: this phenomenon is the so-called *Fermi level pinning*, illustrated in the constant regime in figure 1.2b. Causes of this fact should be traced back to the balance between interface electric potential - due to molecular ionization and capacitive effects - and contact surface potential - governed by work function - reached over (under) the pinning threshold.

In order to minimize the interface resistance and the device driving voltage, the anode and cathode energy levels should be as aligned as possible with HOMO and LUMO, respectively. Many technologies and methods such as electrode surface treatments have been being developed to achieve this goal: this is the reason why this thesis focuses its attention on the effects of introducing a thin TMO buffer layer between the semiconductor and the electrode.

## 1.2 Transition Metal Oxide physical and chemical features

Since TMOs cover a great extent in work function scale (see figure 1.3), their appropriate use can tailor interface energy levels according to different kinds of semiconductor. Among compounds such as defective $ZrO_2$ (WF = 3.5 eV) and $V_2O_5$ (WF = 7.0 eV)[1], molybdenum oxides with different stoichiometries fall into the category of high work function materials (WF can exceed 6.8 eV for stoichiometric $MoO_3$ [1]), so that they are suitable for hole-extracting buffer layers, whereas titanium oxide ($TiO_2$), with a lower WF of around 5 eV[1], is appropriate for electron-extracting ones.

From a chemical point of view, metal-oxygen (M-O) bonds in TMOs could be treated according to *crystal field theory* as a negative charge transfer from $M^{x+}$ to $O^{2-}$ or in terms of *ligand field theory* as a combination of oxygen 2p and metal d molecular orbitals (MO), both leading to similar results unless correlation effects between electrons are considerably strong.

In the case of extended crystals, the broadening of orbital levels determines band structure creation and hybridization of O2p and metal d orbitals. In fact, their overlap integrals are different from zero and they jointly contribute to total density of states (DOS) in the solid, even it is possible to continue distinguishing a dominant contribution of O2p or d to the character of every band so that these labels can still be used. For example, valence band maximum levels in TMOs arise from oxygen 2p orbitals, whereas the bottom of CB mainly consists of metallic d states.

In this context, MO filling determines the insulating, semiconductor or conductive character of TMOs so that they can be grouped in different classes: from $d^0$ oxides with empty conduction band to reduced oxides with an increasing occupancy of it and a metallic character, up to a $d^{10}$ semiconductor configuration.

Structural defects, metal or oxygen vacancies, changes in oxidation state and other TMO features resulting in intra-gap levels are crucial to establish the Fermi energy position and the *p*-type or *n*-type nature of every compound. In particular, in the case of $d^0$ oxides as $MoO_3$ and $TiO_2$, a native presence of oxygen vacancies determines the appearance of a defect band inside the energy gap below CB minimum, so that these oxides can be regarded as *n*-type semiconductors.

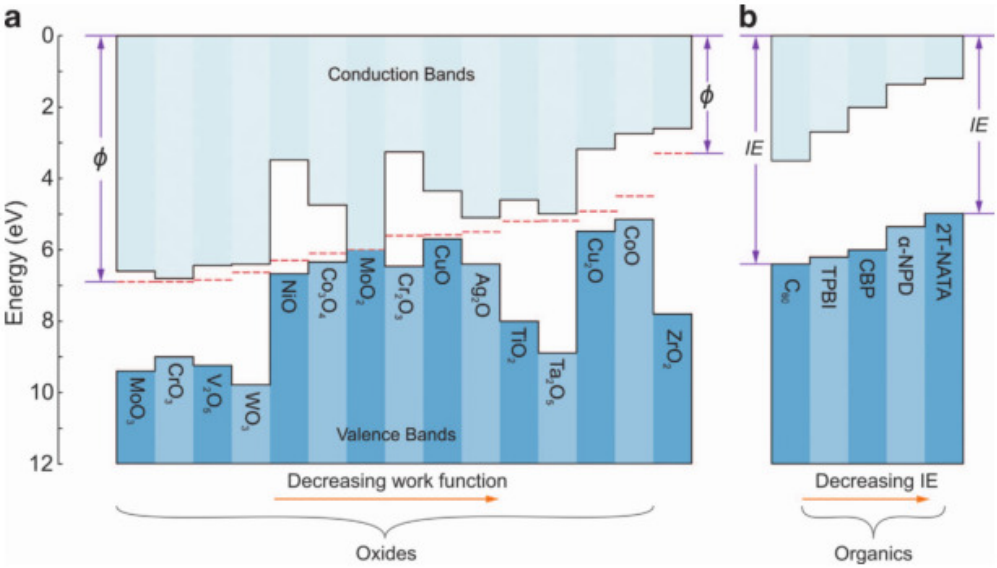


Figure 1.3: Examples of different transition metal oxide (a) and organic semiconductor (b) energy band diagrams. The variety of work functions suggests the importance of a careful study in order to tailor the best TMO-semiconductor interfaces for OPV devices. In the scheme, TMO valence and conduction bands, Fermi levels and work functions ($\Phi$) are shown, together with semiconductor ionization energies (after [1]).

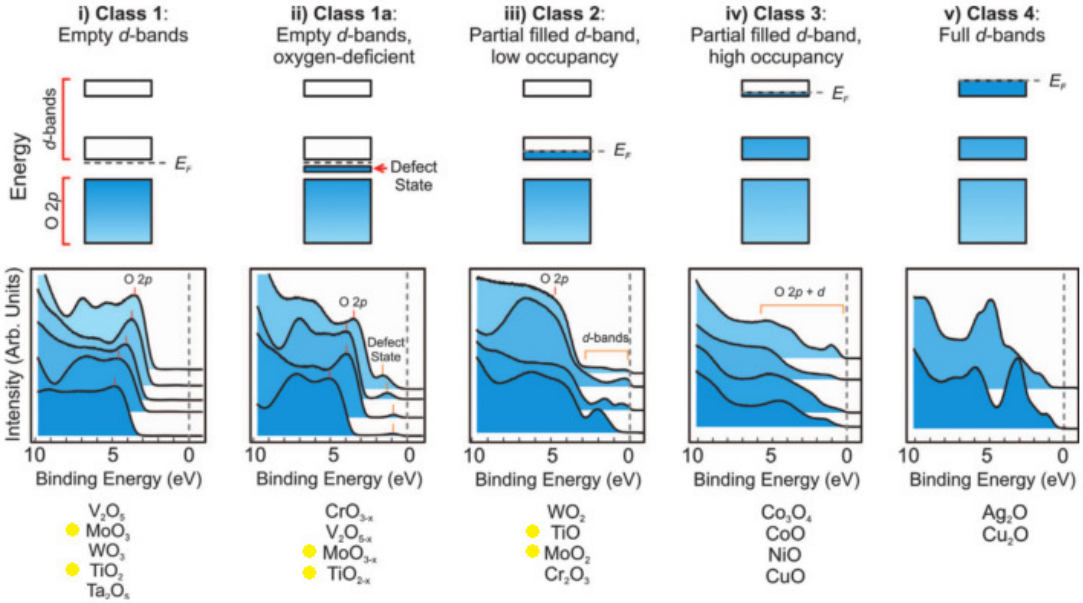


Figure 1.4: Different TMO classes: energy band diagrams (top) and photoemission spectra from valence band (bottom). Molybdenum and titanium oxide stoichiometries are highlighted. The metallic character of the compounds varies with the occupancy of d-band and intra-gap defect states (after [1]).

Figure 1.4 shows a summary of different TMO energy configurations related to intra-gap state filling.

## 1.3 Transition Metal Oxides as buffer layers for charge extraction

According to the specific electronic structure of different TMOs, it is possible to use them as buffer layers, allowing a single type of carrier to pass (hole-selective or electron-selective layers).

For instance, a $p$-type oxide with a high work function is suitable for hole-selective buffer layers in anode contact:

1. it is $p$-type, so that its Fermi energy is closer to valence than to conduction band;
2. its high work function makes the oxide $E_F$ pin to organic semiconductor HOMO level.

These two facts make it easier for holes to flow from active semiconductor layer to metallic contact through TMO valence band so that an OPV device could improve its performances.

On the other hand, an appropriate oxide should also have a greater band gap than HOMO-LUMO difference, so that electron barrier crossing is prevented.

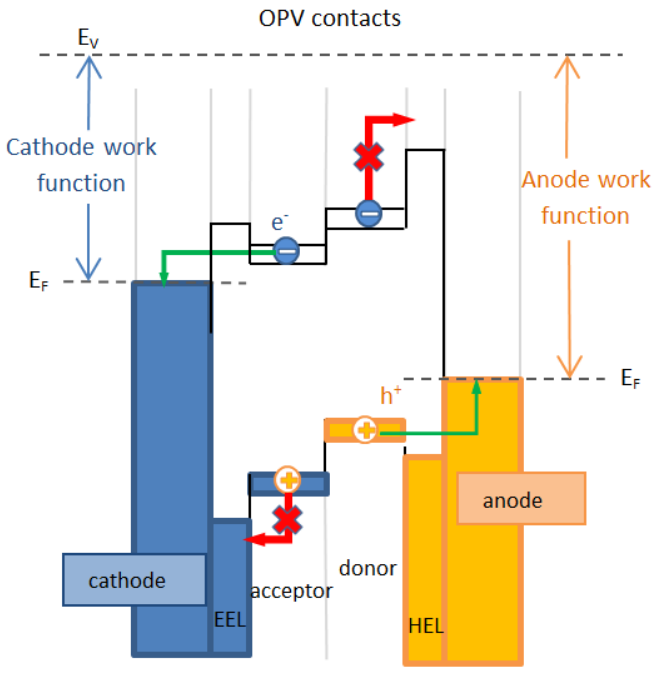


Figure 1.5: Energy band scheme of charge-selective layers in OPV devices: electron-extracting layer (EEL) for the cathode and hole-extracting layer (HEL) for the anode. In the former case, an $n$-type oxide with a large band gap and low work function is represented, in the latter a $p$-type oxide with a large band gap and high work function (after [1]).

Vice versa we can address the cathode buffer layer:

1. it is $n$-type, so that its Fermi energy is closer to conduction than to valence band;
2. its low work function makes the oxide $E_F$ pin to organic semiconductor LUMO level.

Thus, excited electrons can easily flow from semiconductor LUMO to cathode through TMO conduction band and the OPV device performances are improved. The oxide band gap should be greater than HOMO-LUMO difference, so that hole barrier crossing is prevented.

A graphical scheme of energy band structure in an OPV device with the presence of buffer layers for holes and electrons is shown in figure 1.5.

It is important to underline that the dominant factor to determine hole- or electron-selective properties is the oxide work function rather than the $p$- or $n$-type character. For example, an $n$-type semiconductor like $MoO_x$ acts as a hole buffer layer due to its very high work function and the charge flow takes place through the intra-gap defect band below CB minimum. On the other hand, the same defect band in $TiO_2$ assists the passage of negative charges due to the oxide low work function, so that the material has electron-selective characteristics.

## 1.4 Interface energy level and OPV devices performances

As previously said, the presence of a buffer layer is useful to attain the energy level alignment between an organic semiconductor, where carriers are dissociated thanks to the electric field at a donor-acceptor junction, and the $E_F$ of a conductive electrode, which extracts charges from the system. This is crucial not only to decrease contact resistance and energy losses in the carrier extraction process, but also to increase device efficiency. In fact, an OPV cell *power conversion efficiency* $\eta_p$ can be defined as the ratio between the maximum power density $P_{max}$ generated and the incident light power density $P_{in}$ on the device[7]:

$$\eta_p = \frac{P_{max}}{P_{in}} = \frac{J_{SC} V_{OC} FF}{P_{in}}.$$

$J_{SC}$ is the current density which flows through the external circuit when the cell electrodes are in short-circuit (*short-circuit current density*): it is ideally the same as the *photogenerated current* $I_{ph}$, divided by the device area. $V_{OC}$ is the voltage when no current flows in the circuit (*open-circuit voltage*), corresponding to the highest voltage the cell can provide.

The fill factor $FF$ is defined as

$$\frac{P_{max}}{J_{SC} V_{OC}},$$

ratio between the maximum power the device is able to deliver and the product $J_{SC} \times V_{OC}$, so that power conversion efficiency $\eta_p$ can be expressed in terms of these quantities. The solar cell operating parameters can be referred to the equivalent circuit in figure 1.6[8]. Whereas $J_{SC}$ can be maximized improving light absorption and carrier collection by different junction configurations, $V_{OC}$ is directly related to HOMO-LUMO energy gap at the semiconductor junction (*photovoltaic energy gap* $E_{PVG}$), as visible in figure 1.7. Recent experimental results[9] state that this link could be semi-empirically expressed as

$$eV_{OC} = E_{PVG} - 0.47eV,$$

where $e$ is the electron charge and where the precise physical meaning of the 0.47 eV energy offset is still to be completely understood.

In order to tailor a high $E_{PVG}$ junction it is important to have a high ionization energy (IE) donor and a low electron affinity (EA) acceptor. TMO buffer layers and their help in energy level pinning to electrodes can control and stabilize HOMO and LUMO and maximize $E_{PVG}$.

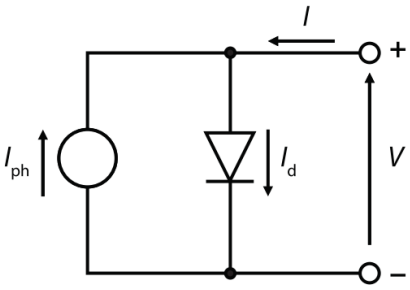


Figure 1.6: An illuminated solar cell can be represented by a current source of photogenerated charges ($I_{ph}$) and an ideal $p$-$n$ junction diode in parallel in which the current $I_d$ flows (after [8]).

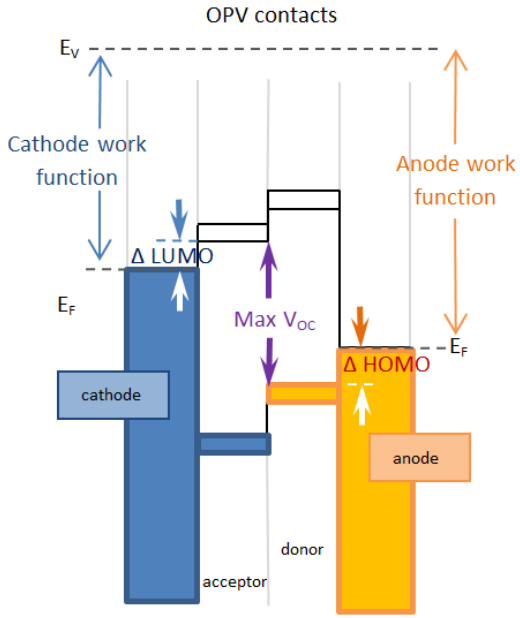


Figure 1.7: Band diagram scheme for an OPV device. Cathode and anode work functions together with differences between electrode $E_F$ and semiconductor energy levels ($\Delta$LUMO and $\Delta$HOMO) are represented. The maximum $V_{OC}$ is shown as the HOMO-LUMO difference at the $p$-$n$ junction (after [1]).

# Chapter 2

# Transition metal oxides: background and research objectives

## 2.1 A model for Transition Metal Oxide work function

Since a full control on TMO work function is crucial to tailor suitable band structures for *Fermi level pinning* to HOMO/LUMO of desired organic semiconductors for high-performance OPV devices, it is worth having an insight into electronic properties of these compounds to understand the origin of their work function. In particular, M.T. Greiner[2] proposed a theoretic model for dilute defects in oxides with empty d band in their stoichiometric form, explaining the role of different factors which have an influence on TMO work function. Generally speaking, a wide range of causes are involved in determining oxide electronic properties, like surface roughness, crystalline phase and direction, radiation exposure, adsorbate presence, impurities and stoichiometry - which affect both electron chemical potential and surface dipole.

In the case of an $n$-type oxide whose defects are mainly due to oxygen vacancies as $MoO_x$, the main factors changing the energy needed by a charge to exit the material are the decrease of cation electronegativity after reduction and the rise of donor concentration, so that WF can be expressed as

$$WF = WF_0 + \Delta WF_\chi + \Delta WF_d, \tag{2.1}$$

where $WF_0$ is the work function of reference near-stoichiometric compound and $\Delta WF_\chi$ and $\Delta WF_d$ are its modifications due to cation electronegativity and donor concentration, respectively. They can be rewritten in a more explicit way analyzing the factors they depend on. In the notation of Kröger-Vink, the reaction to produce oxygen vacancies is

$$O_O^x + 2M_M^x \longrightarrow v_O^{\bullet\bullet} + 2M_M' + \frac{1}{2}O_{2(gas)},$$

in which $O_O^x$ and $M_M^x$ are ions of oxygen and metal in a stoichiometric oxide with their normal charge, $v_O^{\bullet\bullet}$ is the oxygen vacancy with two positive charges and $M_M'$ the reduced metallic cation after acquiring an electron more. Considering the example of substoichiometric molybdenum oxide $MoO_{3-x}$, the same reaction is expressed by

$$O_O^x + 2Mo^{6+} \longrightarrow v_O^{\bullet\bullet} + 2Mo^{5+} + \frac{1}{2}O_{2(gas)}. \tag{2.2}$$

Firstly, reduced $MoO_{3-x}$ has an increasing percentage of $Mo^{5+}$, whose work function is lower than $Mo^{6+}$ cation, so that the development of Fermi energy expression considering also the role of oxidation states for binary compounds $A_mB_n$

$$E_F = (\chi_A^m \chi_B^n)^{1/(m+n)}$$

leads to

$$\Delta WF_\chi = E_F = ((\chi_{Mo^{6+}})^{1-2x}(\chi_{Mo^{5+}})^{2x}(\chi_{O^{2-}})^{3-x})^{1/(4-x)}, \tag{2.3}$$

where $\chi_{Mo^{6+}}$, $\chi_{Mo^{5+}}$ and $\chi_{O^{2-}}$ are electronegativities of different ions. Equation (2.3) expresses a linear proportionality between the degree of oxygen deficiency $x$ and work function change $\Delta WF_\chi$ (the trend is shown in figure 2.1b).
A second effect of oxide reduction is the concentration increase of donor states, whose ionization promotes negative charges into conduction band (CB), raises Fermi level and decreases work function of the material. Since Photoemission Spectroscopy data reveal that the dominant kind of defect in stoichiometric $MoO_x$ is O-vacancy and that they determine Fermi energy $E_F$ to be between 0.39 and 0.59 eV below conduction band minimum $E_c$ ($n$-type semiconductor), it is possible to relate Fermi level to electron concentration in conduction band $n^e$ by

$$E_F - E_c = -kTln(\frac{n^e}{N_c}), \tag{2.4}$$

where $N_c$ is the effective CB minimum density of states, k the Boltzmann constant ($1.38\times10^{-23}$J·K$^{-1}$ = $8.62\times10^{-5}$eV·K$^{-1}$), T the absolute temperature and free carrier density in CB is expressed as

$$n^e = \sqrt{N_v N_c exp(\frac{-E_g}{kT})}, \tag{2.5}$$

being $N_v$ the effective DOS in VB and $E_g$ the energy gap width.
From (2.4) and (2.5) it results

$$E_F - E_c = -\frac{1}{2}kTln(\frac{N_v}{N_c}exp(-\frac{E_g}{kT})),$$

but since negative charges derive from both O2p orbitals of VB and intra-gap defect states, the two contributions should be taken into account, so that

$$E_F - E_c = -\frac{1}{2}kTln(\frac{N_v}{N_c}exp(-\frac{E_g^{(0)}}{kT}) + \frac{N_d}{N_c}exp(-\frac{E_g^{(d)}}{kT})), \tag{2.6}$$

with $N_d$ the effective DOS in defect band and $E_g^{(0)}$ and $E_g^{(d)}$ the energy positions of respectively O2p orbitals and defect states below CB minimum. In this equation $N_d$ can be expressed by cation concentration $[Mo^{5+}]$.

From the O-vacancy creation reaction (2.2), the equilibrium constant K can be written as

$$K = \frac{[v_O^{\bullet\bullet}][Mo^{5+}]^2}{[O_O^x][Mo^{6+}]^2} p_{O_2^{1/2}} \cong \frac{1}{2}[Mo^{5+}]^3 p_{O_2^{1/2}}$$

because $[O_O^x][Mo^{6+}]^2 \sim 1$ for dilute defects and $[Mo^{5+}] = 2\,[v_O^{\bullet\bullet}]$. From the theory of reaction thermodynamics a final expression for cation concentration is therefore

$$[Mo^{5+}] = \sqrt{2}exp(-\frac{\Delta H_{vO}}{3kT})p_{O_2^{-1/6}}, \tag{2.7}$$

being $\Delta H_{v_O}$ the formation enthalpy of O-vacancies and $p_{O_2}$ the gas-phase oxygen partial pressure. Using the approximation $\Delta H_{v_O} \sim 0.55$ eV[10], $p_{O_2} = 1$ for a slow equilibrium with gas in the vacuum chamber where the reaction takes place and T = 850 K of oxide deposition temperature, an O-deficiency of $x \approx 5{\times}10^{-7}$ for stoichiometric $MoO_3$ is obtained.

Equations (2.6) and (2.7) highlight a steep initial decrease of WF when donor concentration rises in the vicinity of stoichiometry, visible in figure 2.1c. Since defect state energy is only few tenth of electron-volts below CB whereas VB maximum made of O2p orbitals is 3.0-3.2 eV from it, it is reasonable to consider only carries coming from intra-gap states and a final expression for donor-concentration-related work function evolution is

$$\Delta WF_d = -\frac{1}{2}kTln(\frac{[Mo^{5+}]^{(d)}}{[Mo^{5+}]^{(0)}}), \tag{2.8}$$

with $[Mo^{5+}]^{(d)}$ and $[Mo^{5+}]^{(0)}$ the cation densities in defective and nearly stoichiometric $MoO_x$, respectively. In this case the underlying assumption is that valence, conduction and defect levels in band scheme remain constant with O-deficiency increase, which is correct for dilute donor regime.

From (2.1), (2.3) and (2.8) an equation accounting for the influence of different factors on work function changes is finally extracted:

$$WF = WF_0 + ((\chi_{Mo^{6+}})^{1-2x}(\chi_{Mo^{5+}})^{2x}(\chi_{O^{2-}})^{3-x})^{1/(4-x)} - \frac{1}{2}kTln(\frac{x}{x_0}), \tag{2.9}$$

where $x$ and $x_0$ are O-vacancy concentrations in defective and reference near-stoichiometric oxides. Using the aforementioned values of $x_0 = 5{\times}10^{-7}$ and T = 850 K and ionic electronegativities of $\chi_{Mo^{6+}} = 6.4$ eV, $\chi_{Mo^{5+}} = 5.4$ eV and $\chi_{O^{2-}} = 11.3$ eV[11], the outcome is the work function trend versus O-deficiency shown in figure 2.1a.

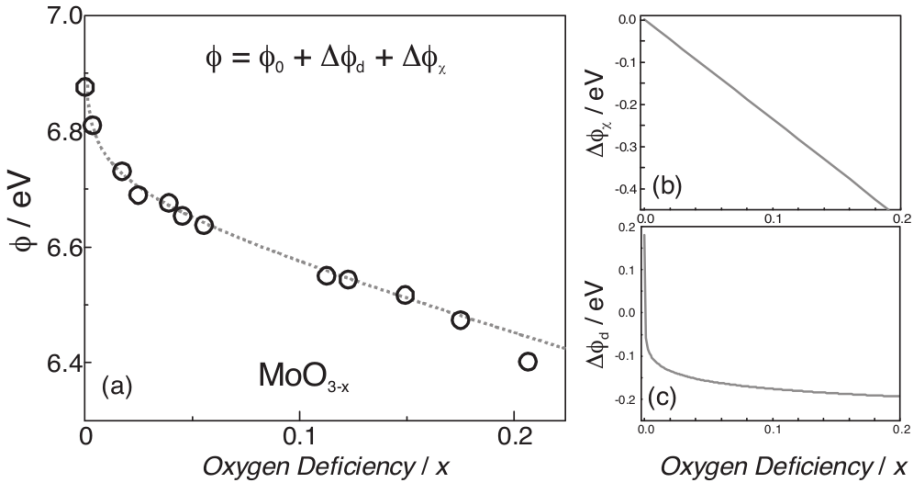


Figure 2.1: Charts of work function $\phi$ evolution versus oxygen deficiency $x$ in non-stoichiometric molybdenum oxide $MoO_{3-x}$ (a), with details of respective contributions of electronegativity (b) and donor state concentration (c) (from [2]). In graph (a) the dashed line represents work function trend according to model equation (2.9), whereas the black circles are experimental data reported in ref. [2].

## 2.2 Previous research on $MoO_x$

Among TMOs, molybdenum oxide is notably promising as a suitable compound for hole-extracting layers in OPV devices, because of its high work function and transparency. The most important step on the way of interface engineering for electronics is the ability to tailor $MoO_x$ energy levels to fit different organic semiconductors.

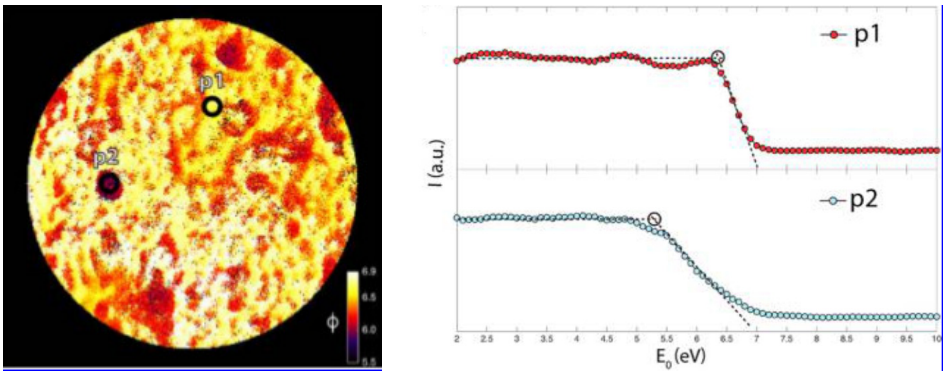


(a) (b)

Figure 2.2: Work function LEEM measurements for different sites on molybdenum oxide surface. LEEM analysis is performed varying the low-energy electron beam landing energy: when it reaches the value of the sample work function a drop off in the elastically reflected electron intensity image (a) is observed. This map is acquired with an aperture of 10.5 $\mu$m at a landing energy of 6.0 eV and the technique can give a lateral spatial resolution of ∼15 nm. The color scale ranges from 6.9 eV of light yellow to 5.5 eV of dark blue. I/V curves for sites p1 and p2 (b) allow to extract respective work functions of 6.5 and 5.5 eV (after [6]).

In this context, previous studies have investigated the relation between stoichiometry, morphology and band diagram in molybdenum oxide. It is important to specify that the oxide is referred to as $MoO_x$ because O:Mo ratio could vary, but the canonical stoichiometry for this material is $MoO_3$: three oxygen atoms for every transition metal one, resulting in a molybdenum oxidation state of $Mo^{6+}$.

In different experiments[5][6] $MoO_3$ has been compared to substoichiometric and superoxidized compounds ($MoO_x$ with $x \sim 2.57$ and 3.16, respectively), deposited by DC-reactive sputtering with appropriate oxygen pressures in the chamber controlled environment. Several characterization techniques were employed, such as Low-Energy Electron Microscopy (LEEM) to map work function inhomogeneities on the surface, Low-Energy Electron Diffraction (LEED) to check the sample crystallinity, High-Resolution Transmission Electron Microscopy (HRTEM) to study the oxide morphology, Auger Electron Spectroscopy (AE) and X-ray Photoelectron Spectroscopy (XPS) to analyze surface chemical composition.

Some results should be highlighted as a starting point for the experiments presented in this thesis.

In particular, post-deposition ultra-high vacuum annealing at 500°C has different effects depending on O:Mo ratio and LEEM can analyze them both from a structural and an energetic point of view (an example of LEEM results can be seen in figure 2.2):

1. After annealing at 500°C, $MoO_{2.57}$ has a flat topography and a homogeneous work function of $WF_{MoO_{2.57}} = 6.4$ eV.

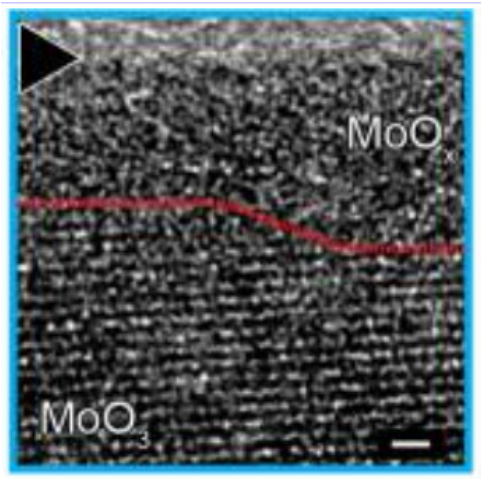


Figure 2.3: High-Resolution TEM micrograph after annealing at 500°C of $MoO_x$ sample: detail of the surface layer. The red dotted line highlights the separation between the top nanometers of disordered non-stoichiometric film ($MoO_x$) and a high-quality crystalline substrate ($MoO_3$). Scale bar of 1 nm (from ref. [6]).

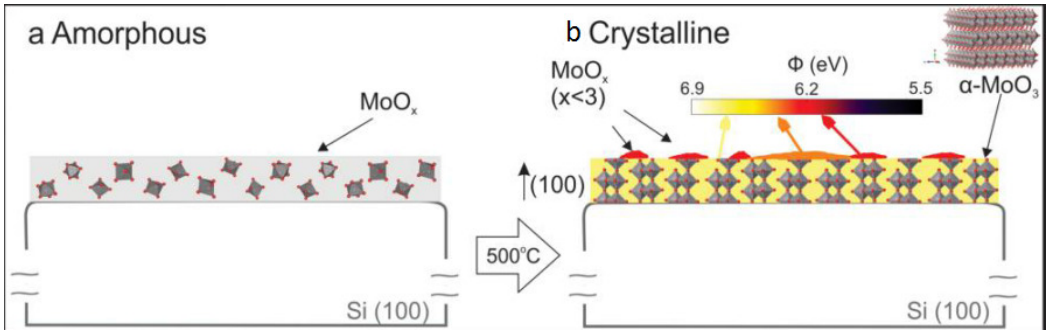


Figure 2.4: Schematic illustration of previous results of LEEM. Work function changes in initial amorphous $MoO_3$ (a) after ultra-high vacuum annealing at 500°C (b) are interpreted as due to the formation of a crystalline underlayer ($\alpha$-$MoO_3$ with molecules positioned along (100) direction, as shown in the upper right detail) and a substoichiometric overlayer ($MoO_x$ with $x<3$) whose work function ranges from ~5.5 eV to ~6.6 eV (after [6]).

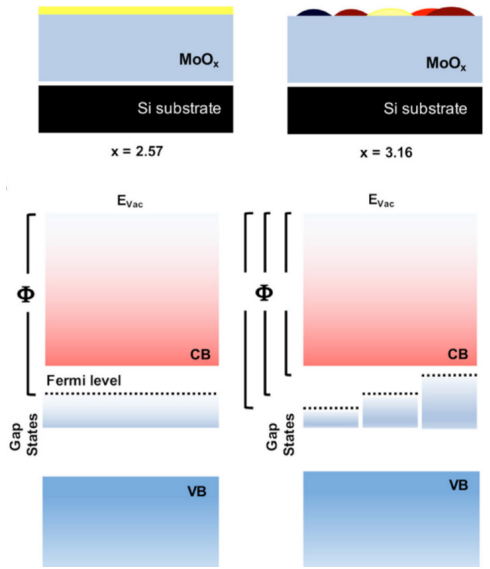


Figure 2.5: Surface morphology schemes (top) and band diagrams (bottom) for substoichiometric and superoxidized $MoO_x$. Differences of work function ($\Phi$) can be explained by the filling of intra-gap defect states, which reduces it and enhances metallic character of the oxide. Whereas $MoO_{2.57}$ has one oxidation state only, $MoO_{3.16}$ develops many surface nanoaggregates with different levels of gap-state filling (after [5]).

2. As resulting from HRTEM data (figure 2.3) and summarized in the scheme in figure 2.4, annealing $MoO_3$ - specifically, superoxidized samples - determines the separation between a crystalline substrate of orthorhombic $\alpha$-$MoO_3$ and nanometric amorphous grains with both stoichiometric and reduced $MoO_x$ (i.e. rich in oxygen vacancy defects); these surface zones have respective work functions of 6.6 eV and 5.5-6.0 eV.

3. The oxygen abundance in $MoO_{3.16}$ stimulates grain nucleation on the surface: the aggregates tend to have a work function up to 6.5 eV and a stoichiometric composition, whereas lower WF flat zones are associated with reduced oxide (with a work function of $\sim$6.1 eV).

4. Reduction process could be interpreted as a filling of 4d-band intra-gap states, which increases metallic character of the compound and decreases molybdenum oxidation state from $Mo^{6+}$ to $Mo^{5+}/Mo^{4+}$, however preserving a high work function (figure 2.5). This mechanism has been confirmed by UPS and XPS measurements[5][6].

Thus it seems that partially reduced $MoO_x$ is suitable for anode buffer layers because of its high and uniform work function combined with a nearly metallic and conductive behavior which can improve carrier extraction, whereas the associated crystalline substrate helps to increase charge mobility. In this thesis, the focus will be therefore on the physical and chemical $MoO_x$ properties and on their evolution with annealing temperature and other experimental parameters.

## 2.3 A further insight into $TiO_2$

This compound has a well-known structure with a canonical $TiO_2$ stoichiometry (which can vary in a $TiO_x$ form) and investigations on it have collected a large amount of data during the years[3][4][12][13]. Like $MoO_x$, it could be employed as a buffer layer in solar cells, but it is rather suitable for enhancing electron transport as cathode buffer layers, due to its $n$-type nature and lower work function (of 4.9 eV and 5.1 eV for the two main phases, rutile and anatase[13]).

Therefore, this thesis also presents some results extracted from the analyses of different $TiO_2$ samples. In particular, previous Photoemission Electron Microscopy (PEEM) and X-ray Absorption Spectroscopy (XAS) studies have been carried out on this material, showing the different electronic properties of the two phases[13]. Analyzing a film of anatase with embedded rutile nanocrystals, it was discovered that X-ray PEEM and UV-PEEM maps have reversed contrast, as shown in figure 2.6. Since the high-energy X-ray photons are not sensitive to slight work function differences, XPEEM map light and dark regions are mainly due to nanocrystal morphology which deviates ejected electrons. Conversely, UV photons match $TiO_2$ work function and the light regions of the resulting surface map correspond to lower work functions and higher density of states in valence band. Both these characteristics were measured for rutile in relation to anatase by Conductive AFM and Ultraviolet Photoelectron Spectroscopy. Research outcomes suggest that staggered band alignment at rutile-anatase interfaces in multi-phase $TiO_2$ is likely to induce a better charge separation and an improvement of electronic properties for photovoltaic applications.

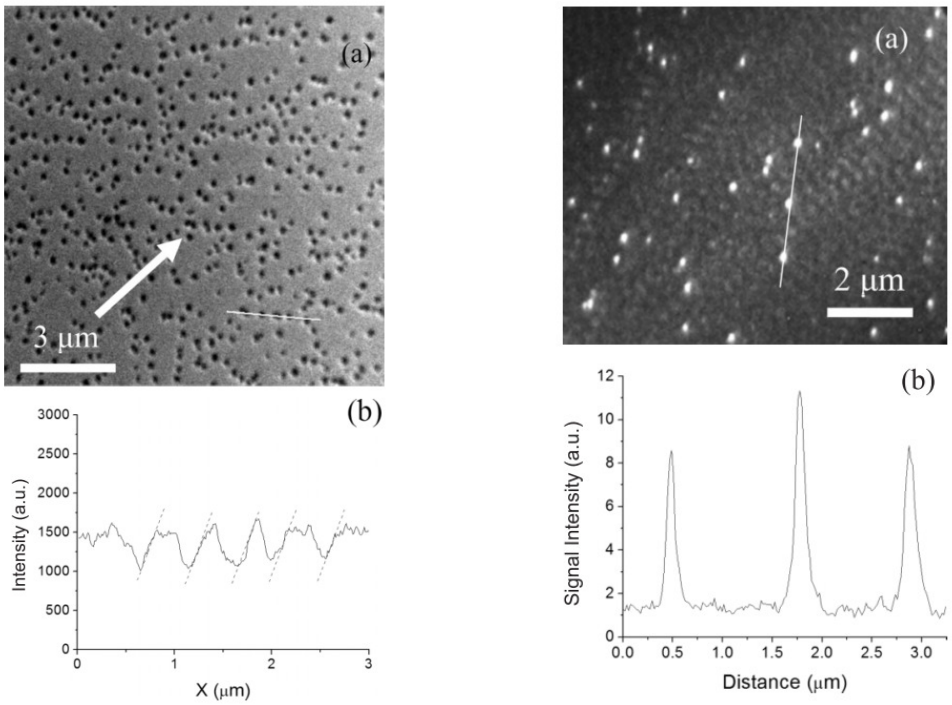


(a) *XPEEM surface map (a) and intensity profile (b), revealing the lower emission from rutile nanocrystals.*

(b) *UV-PEEM surface map (a) and intensity profile (b), revealing the higher emission from rutile nanocrystals.*

Figure 2.6: X-ray and Ultraviolet Photoemission Electron microscopy results for the same sample of two-phase $TiO_2$ (after [13]).

Another recent study[12] analyzed the effect of UV light and molecule absorption on titanium oxide and measured the changes in photoluminescence. This phenomenon takes place in defect sites, where photon-induced electron-hole couples tend to recombine. The results reveal that ultraviolet irradiation flattens the band diagram of $n$-type $TiO_2$, reducing the depletion layer width. The increased number of available recombination sites enhances the photoluminescence, which negatively affects photovoltaic performances of the oxide. On the other side, oxygen could play a role in reducing recombination process in $TiO_2$. It was demonstrated that it can be reversibly absorbed, increasing the upward band bending and deepening the depletion layer, or irreversibly integrated into the oxide structure, healing $O_2$ vacancy defects and reducing photoluminescence, thus enhancing $TiO_2$ properties for electronic applications.

# Chapter 3

# Synthesis techniques

In order to have a deep comprehension of the Transition Metal Oxide sample characteristics, it is important to introduce and illustrate the two different methods used for deposition, reactive DC-sputtering and thermal evaporation. Synthesis was carried out by an engineering research team at the Mads Clausen Institute of the University of Southern Denmark (SDU), in which we collaborated during the development of this thesis with Dr. Madsen and Dr. Ahmadpour.

## 3.1 Reactive DC-sputtering

Reactive DC-sputtering is a Physical Vapor Deposition (PVD) method which allows to control many synthesis parameters[14]. The deposition is performed in a vacuum chamber with a pressure of around $10^{-8}$ mbar, where a high electric field of radio frequencies ionizes argon, the so-called *carrier gas* of the process. The atoms to be deposited are initially on a negative biased target, so that they can be hit and knocked-off by the gas positive ions ($Ar^+$). The sputtered species are therefore guided inside the vacuum system and attracted towards the final deposition film by a positive voltage applied to the latter. In the present case target is made of molybdenum atoms and an oxygen flow is introduced inside the chamber environment, so that a chemical reaction takes place and molybdenum oxide could be finally deposited.

This technique offers the advantage of monitoring and setting a range of conditions, notably sputtering power, carrier gas flow rate - to maintain the suitable chamber pressure, the oxygen flow rate - crucial to modify O:Mo ratio in oxide stoichiometry and to engineer O-vacancy presence - and temperature - important to influence compound properties. Other relevant positive aspects of DC-sputtering are satisfactory surface coverage, film homogeneity and thickness control (thanks to a quartz crystal microbalance providing tenth-of-an-angstrom thickness sensitivity).

Even if oxide structures synthesized by this technique are usually characterized by short-range order, suitable post-growth treatments can be realized to effectively improve crystalline structure and enhance transport properties at the interface with semiconductor active layers and with metallic electrodes, as discussed in details in the following chapters.

## 3.2 Thermal evaporation

Thermal evaporation is an alternative PVD technique suitable for direct deposition of molybdenum oxide in the form of powder[14].

It takes place inside a vacuum chamber, with a pressure of $10^{-8}$ mbar in the case of SDU facility. The materials to be deposited are contained in crucibles that are heated by a high electrical current so that evaporation is realized. The molecules are deposited on final target layers on the top of the chamber, mounted upside down on a rotating sample holder to enhance film uniformity.

Even if this method is easily realizable, it does not allow a precise control on O:Mo ratio in the film and on oxide crystalline structure, typically resulting in amorphous layers with weak conductive properties.

# Chapter 4

# Characterization techniques

First of all, it is important to illustrate the instruments and techniques employed to investigate the samples. Their aim is both structural and electronic characterization of $MoO_x$ and $TiO_2$, varying from the analysis of crystalline morphology to the detection of different chemical elements or the study of energy levels in the oxides.

## 4.1 KPFM

Kelvin probe force microscopy (KPFM) combines classical Kelvin probe technique[15] with standard atomic force microscopy (AFM)[16], in order to probe the contact potential difference (CPD) between the sample surface and a conductive tip at the nanometric level. Its strength consists in giving information about both morphology and energy in an intuitive visual form - a surface image.

### 4.1.1 Principles of operation

A Bruker NanoScope MultiMode 8 Scanning Probe Microscope was used (a picture is visible in figure 4.1); it is hence useful to explain its operating principles.

A typical KPFM measurement is performed by a two-step procedure:

1. a standard AFM scan that records surface topography keeping tip oscillation amplitude or frequency constant thanks to a feedback loop (amplitude or frequency modulation, indicated as AM or FM);

2. the so-called *lift scan*, which follows the previous morphology and detects surface potential changes.

CPD is defined as

$$V_{CPD} = \frac{WF_t - WF_s}{e},$$

where tip and sample work functions are referred to as $WF_t$ and $WF_s$ and $e$ is the elementary charge (see figure 4.2). When the metallic AFM tip and the sample are not connected, their vacuum levels are aligned but their Fermi energies are not. Contact allows charge exchange and respective $E_F$ align, creating an electric field proportional to $V_{CPD}$, which can be measured applying to the tip an appropriate voltage to counteract the tip-sample force. In KPFM technique both a direct and an alternating voltage ($V_{DC}$ and $V_{AC}$) are used, so that the total potential difference $\Delta V$ is[17]


Figure 4.1: Bruker MultiMode 8 Atomic Force Microscope, with the appropriate scanner mounted on the head to perform KPFM technique.

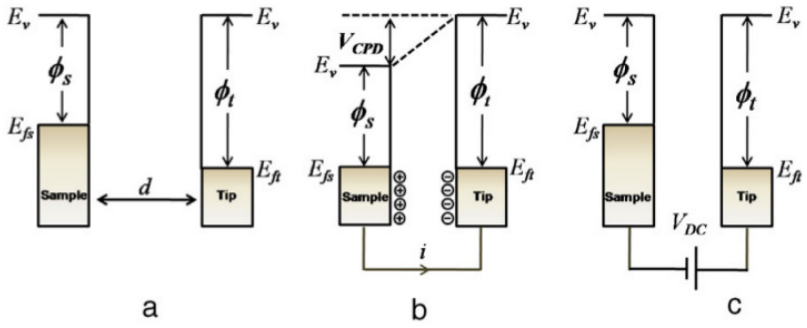


Figure 4.2: Operating principles of Kelvin probe technique. When tip and sample are separated their vacuum levels $E_v$ are aligned (a); when a contact between them is made their Fermi levels $E_{fs}$ and $E_{ft}$ align and contact potential difference $V_{CPD}$ can be detected, equal to the work function difference $\phi_t$-$\phi_s$ (b); a suitable voltage $V_{DC}$ can equal $V_{CPD}$ and make the vacuum levels align again (c) (after [15]).

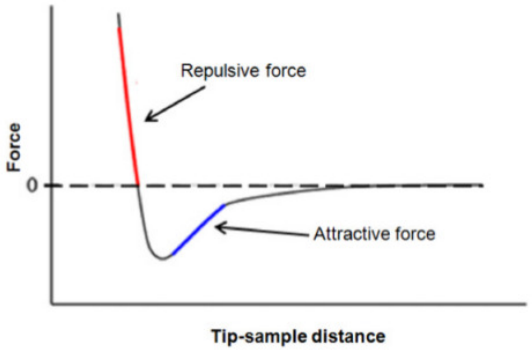


Figure 4.3: Force-distance curve for tip-sample system. It is possible to distinguish repulsive and attractive regions, with respectively positive and negative force (after [15]).

$$\Delta V = V_{DC} + V_{AC} sin(\omega t) \pm V_{CPD}, \tag{4.1}$$

where $\omega$ is $V_{AC}$ frequency and $V_{CPD}$ is added (+) if $V_{DC}$ is applied to the sample and subtracted (-) if it is applied to the tip.

Modelling the tip-sample system as a parallel plate capacitor, its electrostatic force $F_{es}$ expression is

$$F_{es}(z) = -\frac{1}{2}\Delta V^2 \frac{dC(z)}{dz}, \tag{4.2}$$

where dC/dz is the capacitance gradient and z direction is normal to the sample area.

According to (4.1) and (4.2), $F_{es}$ has three components:

1. $F_{DC} = -\frac{\partial C(z)}{\partial z}[\frac{1}{2}(V_{DC} \pm V_{CPD})^2]$,
   which is the static cantilever deflection (DC term);

2. $F_{\omega} = -\frac{\partial C(z)}{\partial z}(V_{DC} \pm V_{CPD}) V_{AC} sin(\omega t)$,
   the component with the same frequency as $V_{AC}$ voltage ($\omega$ term);

3. $F_{2\omega} = \frac{\partial C(z)}{\partial z}\frac{V_{AC}^2}{4}[cos(2\omega t) - 1]$,
   useful for capacitance microscopy ($2\omega$ term).

The measurements displayed in this thesis make use of AM mode in the lift scan, since the three force components are detected using cantilever deflection and $V_{DC}$ is adjusted to nullify the amplitude of $F_{\omega}$: this enables to map $V_{CPD}$ all over the sample surface. In order to separate topographical and electrical data collected by the same tip, $\omega$ of $V_{AC}$ is normally higher than mechanical oscillation frequency of the cantilever. Moreover, morphology is extracted from the first resonance frequency tip response and $V_{CPD}$ from the second. Amplitude modulation mode directly detects the electrostatic force (figure 4.3), whereas frequency modulation passes through force gradient. Thus, due to the respective force and force gradient trends - the latter is steeper and goes more rapidly to zero, AM mode ensures a wider detection range, but also a worse spatial resolution because results should take account both of tip and cantilever interactions with the sample. In fact, modelling the AFM tip as a cone[17], it is possible to calculate that in AM mode only less than 50% of CPD information is gathered by the tip for a 5 nm lift height and the result is instead an average over the whole area covered by the cantilever. On the other side, FM mode can get a 10 nm resolution, collecting more than 50% of CPD data up to 15 nm upon tip end, but this parameter rapidly degrades when the scan height grows to hundreds of nanometers.

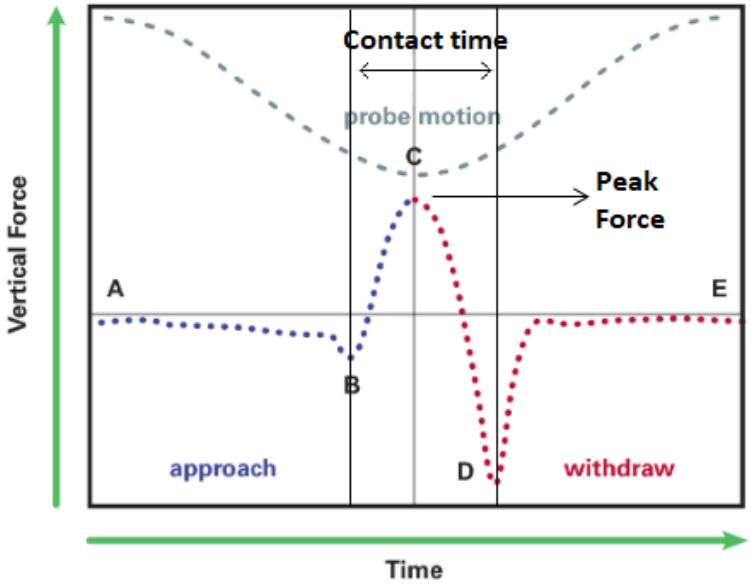


Figure 4.4: Schematic representation of an approach-withdraw cycle in Peak Force KPFM mode: the probe motion on the top and the force curve on the bottom[18]. During the tip spatial motion towards the sample the force decreases in the attractive regime (A-B) and starts to grow in the repulsive one - up to Peak Force C, corresponding to the less tip-sample distance. This maximum interaction level does not typically exceed 10 pN before the tip retracts. During withdraw, adhesion forces mainly due to water particles increase tip-sample attraction (D) until the tip oscillation could start again (E). The tip-sample Contact time is limited to 20-200 $\mu$s between the start and the end of interaction in the system (from B to D).

### 4.1.2 Peak Force mode

The presented measurements make use of a particular operation mode: Peak Force KPFM-AM. It is a Bruker[17][18] improvement for AFM measurements that, when combined with Kelvin probe principles, allows to gain better resolution and accuracy in potential data. For AFM topographical scans, simple Tapping mode is a semi-contact method and it involves tip oscillation over the sample surface near its resonance frequency and a feedback mechanism to keep the oscillation amplitude constant. Also in Peak Force, which is a development of Tapping mode, the tip oscillates near the sample and the mutual interaction is monitored, but it is withdrawn by a feedback loop when force reaches a level of 10 pN, as can be seen in figure 4.4: this reduces Contact time to 20-200 $\mu$s[19] and enables better interaction control (up to the piconewton order) and image resolution in order to avoid tip and sample damage, especially for organic and biological systems.

Therefore, Peak Force KPFM-AM has been chosen as a preferential scanning method for the measurements illustrated in this thesis, even if a comparison with standard Tapping mode will be later discussed. The main parameters to adjust during the acquisition are the image size, the number of samples per line, the scan rate and the height of the lift scan. Moreover, it is possible to introduce a potential offset during CPD mapping.

## 4.2 XPS and UPS

Molybdenum oxide samples were also analyzed with X-ray and Ultraviolet Photoelectron Spectroscopy, using the lab photon sources in the Laboratory of Surface Reactivity (LRS) of Sorbonne University.

The main differences between these techniques and XPEEM discussed below are the spatial resolution - the emitted electrons in XPS/UPS are collected from all the surface under the beam - and the fixed photon energy instead of the tunable $h\nu$ in synchrotron XPEEM.

The use of X-ray or UV photons as well as the application of a sample bias is suitable for different purposes in the analysis. In the case of XPS and UPS with no bias, the experimental configuration is shown in figure 4.5: their aim is to obtain core and valence band electron binding energies, respectively.

Photons start to extract electrons of a specific element when they match the binding energy $E_B$ of the orbital to be analyzed, according to

$$E_K = h\nu - E_B - WF_S,$$

where $E_K$ represents the kinetic energy of the photoelectrons and $WF_S$ is the sample work function.

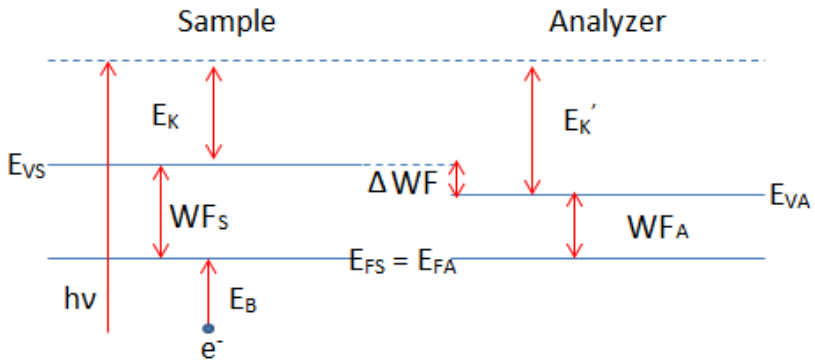


Figure 4.5: Band diagram scheme for the sample-analyzer system in XPS/UPS, with the indication of sample and analyzer work functions $WF_S$ and $WF_A$ and their difference $\Delta$WF; their vacuum levels $E_{VS}$ and $E_{AS}$ and Fermi energies $E_{FS}$ and $E_{AS}$; photoelectron kinetic energies at sample and analyzer $E_K$ and $E_K^{'}$; binding energy $E_B$ of the electron $e^-$ and photon energy $h\nu$.

The kinetic energy detected in the analyzer can be then expressed as

$$E_K^{'} = h\nu - E_B - WF_A,$$

where photon energy $h\nu$ and the analyzer work function $WF_A$ are experimental parameters, while $E_K^{'}$, the electron kinetic energy entering the analyzer, is measured. An example of an XPS overview of different elemental peaks for $MoO_x$ is provided in figure 4.6.

Conversely, negative sample polarization in UPS is necessary to allow all the electrons ejected by the beam to enter the analyzer without being stopped (which would happen if the analyzer vacuum level $E_{VA}$ was higher than the sample $E_{VS}$). In this regime, from

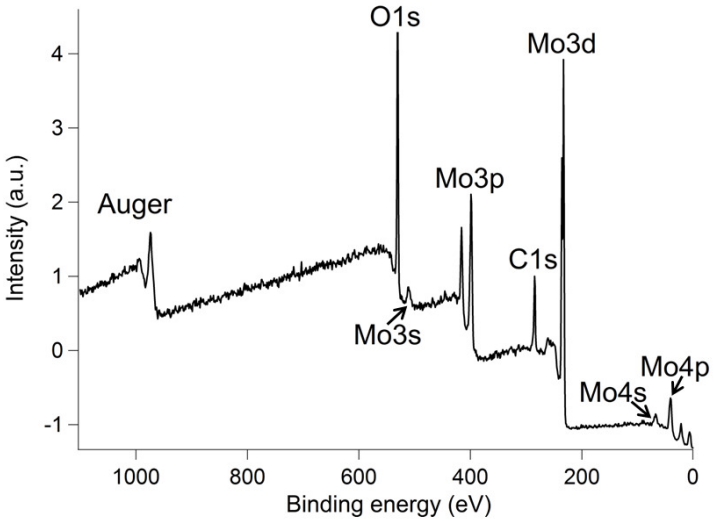


Figure 4.6: Overview of XPS spectra relative to the sputtered $MoO_x$ sample on ITO at room temperature. The main peaks are labelled with the corresponding elemental orbitals.

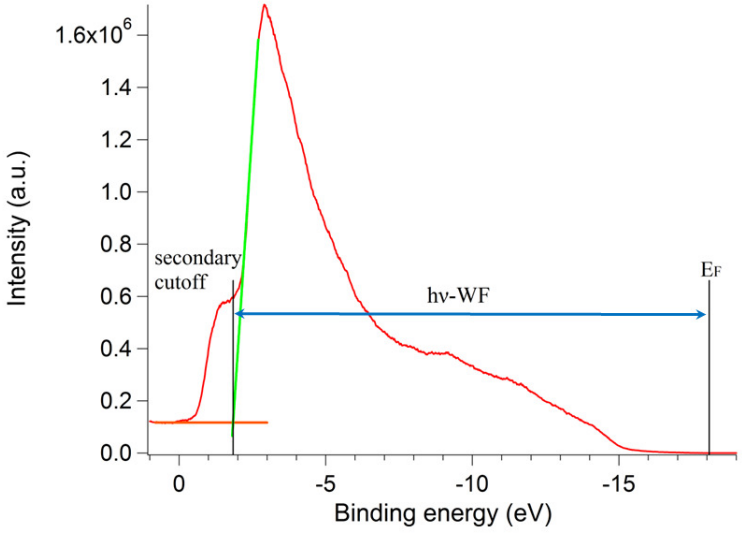


Figure 4.7: Example of work function extraction from a secondary cutoff graph, in the case of $MoO_x$ sputtered on ITO and annealed at 150°C, setting a -18 V bias. The reference Fermi level $E_F$ has been determined in a previous measurement on a Au111 sample.

the difference between the secondary cutoff $E_{SC}$ and the valence band edge ($E_{F,ref}$ of a reference metallic sample) the surface work function can be obtained:

$$E_{SC} - E_{F,ref} = h\nu - WF_S. \tag{4.3}$$

An example of the work function extraction procedure is shown in figure 4.7, where the secondary electron energy $E_{SC}$ is obtained from the intersection between the linear fit on the main cutoff slope and the horizontal tangent to the background intensity.

## 4.3 Synchrotron techniques

### 4.3.1 LEEM

Low Energy Electron Microscopy (LEEM), performed at SOLEIL synchrotron facility, is an investigation method sharing some characteristics with XPEEM, but it is based on electrons rather than photons. An electron gun could be focused on the sample instead of the X-rays and the analyzer collects the charges reflected by the surface. In this case the

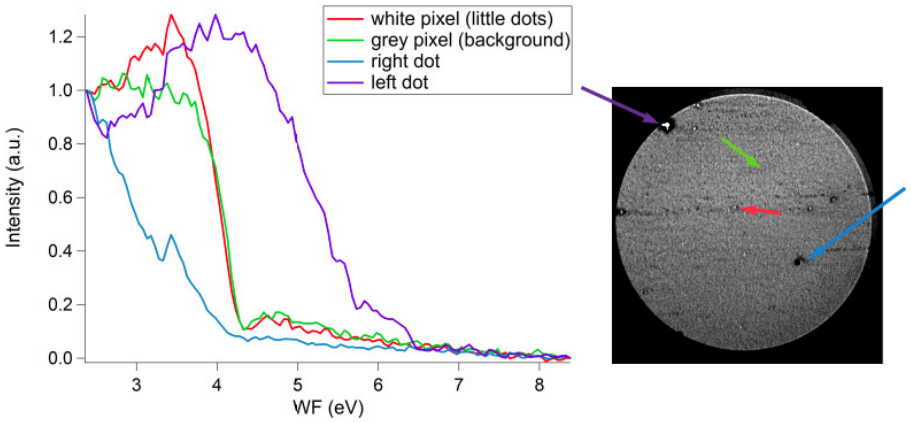


Figure 4.8: LEEM spectra of different surface sites indicated on the overall sample map. The measurements are referred to sputtered $TiO_2$ heated at ~100°C. FOV = 20 $\mu$m; STV = 0.75 eV.

charge energies are varied recording a series of 2D maps: when the electrons overcome the work function $WF_S$, a drop in the reflected intensity is observed. It is hence possible to visualize work function differences on the material, as well as to analyze single pixels or ROIs, even if extraction of quantitative data about absolute work functions requires a precise calibration procedure with determination of cathode WF by a reference sample. The cutoff position on the spectra can be obtained from the intersection between the cutoff linear fit and the tangent to the high intensity region before the drop.

The example in figure 4.8 shows how it is possible to analyze single pixels to detect different work functions on the surface.

### 4.3.2 XPEEM

In order to go further in the sample characterization and to understand in detail the structural and chemical properties of the oxides, a series of measurements has been performed beamline HERMES at the SOLEIL synchrotron facility. The experimental technique called XPEEM (X-ray Photoemission Electron microscopy, a scheme is provided in figure 4.9) is based on the electron ejection from the sample surface due to the photoelectric effect, but it has the advantage of an enhanced spatial resolution. In fact, electrons are not collected from the whole sample as in traditional XPS, but it is possible to detect the surface point where they come from up to a resolution of 15 nm. The small solid angle acceptance of the apparatus is reached by applying a -20 kV bias between the sample and the electrostatic lenses, as explained in the following. This allows to study in detail the properties of different surface regions and to detect texture and crystallinity changes during the annealing process or beam exposure.

In the experimental set-up, the synchrotron beam collides onto the sample surface from an undulator which tunes the photon energy $h\nu$, extracting charges when matching their $E_B$. A potential of -20 kV is then applied to the ejected electrons to accelerate them towards the analyzer, where they are focused by means of electrostatic lenses. During every scan a voltage applied to the sample (Start Voltage STV) is varied to select the electrons according to their kinetic energy (therefore to their binding energy in the sample). Finally, a specific software collects the data and displays them as a series

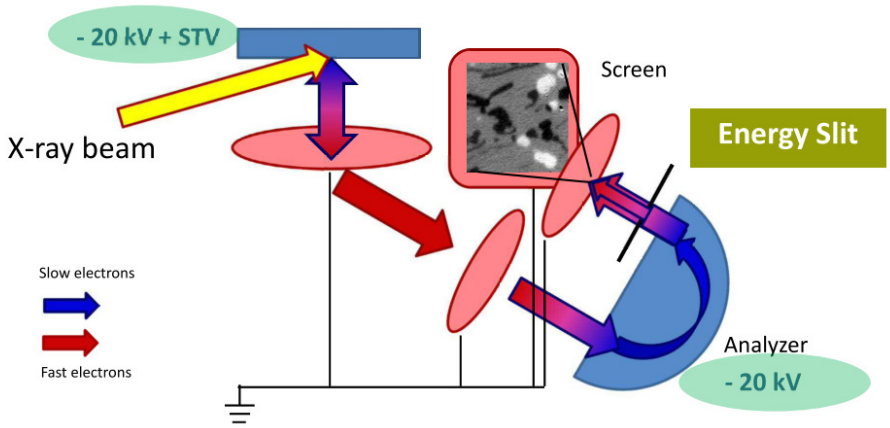


Figure 4.9: XPEEM apparatus scheme. The high voltage (-20 kV) between the sample and the electrostatic lenses accelerates the charges emitted by X-rays and collects only the ones ejected with a specific direction (perpendicular to the surface). The further sample-analyzer potential (Start Voltage STV) selects the kinetic energy of the electrons arriving on the detector. The typical set-up has a fixed energy acceptance slit and the emission spectrum is acquired by changing the STV (after [20]).

of images where the color scale represents the intensity of the charge emission for every surface point. It is possible to select a special region of interest (ROI) to obtain its intensity vs voltage chart with the associated emission peaks.

The technique allows to acquire information from the image plan as in an electron microscope, with a well-resolved detection of which surface position the charges are emitted from, as for the data presented in this thesis. Since every scan results in a collection of successive images at different kinetic energies, it is also possible to analyze the behavior of sample sites in different ranges, for example detecting an inversion of the contrast between points.

### Information acquired by XPEEM

**Sample element orbitals** Unlike the XPS performed with a laboratory X-ray source which provides photon with fixed energies, the synchrotron beam can be set at different $h\nu$ in order to investigate the orbitals of sample elements. Every measurement only scans a limited energy range around the peak of interest and the results do not include overview graphs with all the chemical species. Figure 4.10 provides an example of how powerful XPEEM is in spatially and chemically resolving the sample features: on a surface region with a diameter of 20 $\mu$m it is possible to highlight a lack of molybdenum in a small portion of it. Even if the performed measurements presented in this thesis did not reach the theoretical one of 15 nm, a resolution of $\sim$100 nm was estimated.

**Secondary electron cutoff** Acquiring secondary electron cutoff spectra allows to obtain the work function of the sample regardless of the photon energy, which always has some degree of uncertainty due to different factors such as beamline set-up, calibration procedure and measurement resolution.

The cutoff corresponds to the electrons leaving the samples with a zero kinetic energy. When no potential difference STV is applied between the sample and the analyzer, their

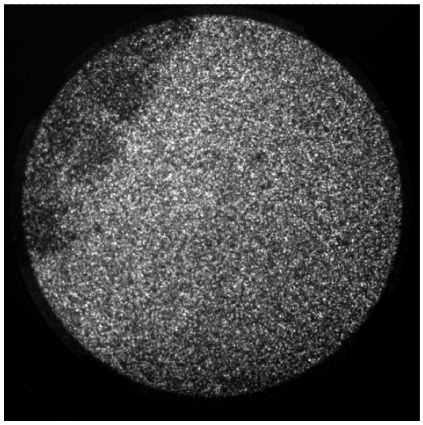

(a) *XPEEM surface map of $MoO_x$ sample (FOV = 20 $\mu m$), acquired at a photon energy of 400 eV and at an STV of 164.13 eV, corresponding to the $Mo3d_{3/2}$ peak. On the left a region with a low content of molybdenum is visible, probably due to a scratch in the oxide layer.*

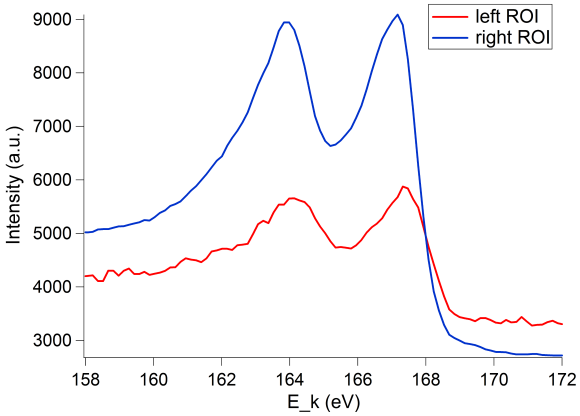


(b) *The two spectra are referred to the left and right (main) surface regions shown in (a). The respective low and high Mo contents provide different intensities in the 3d peaks.*

Figure 4.10: XPEEM analysis of a $MoO_x$ sample, 30 nm thick, sputtered on ITO at room temperature and heated at ∼100°C in the beamline preparation chamber.

Fermi levels $E_F$ are aligned - as in XPS of figure 4.5 - and when an electron is extracted from the surface it enters the analyzer with a surplus of kinetic energy only due to the sample-analyzer work function difference Δ WF:

$$E_K^{'} = E_K + \Delta WF = h\nu - E_B - WF_S + \Delta WF = h\nu - E_B - WF_A,$$

where $E_K$ and $E_K^{'}$ are the electron kinetic energies leaving the sample and entering the analyzer. It is worth specifying that the electron could gain or lose its kinetic energy according to whether the sample vacuum level $E_{VS}$ is higher or lower than the analyzer one $E_{VA}$. Therefore, in order to derive the sample work function $WF_S$, both the measurement of $E_K^{'}$ and the knowledge of $E_B$ and $h\nu$ are required.

Increasing the voltage bias, sample band diagram is shifted and the Fermi energies no more aligned. It is thus necessary to take into account the STV contribution to $E_K^{'}$ measured in the analyzer:

$$E_K^{'} = E_K + \Delta WF - STV.$$

When STV exactly balances the difference ΔWF, no kinetic energy is gained by the electron when captured in the analyzer. If the emission spectrum is acquired varying the bias around this value, the STV where the first electrons appear - the cutoff - corresponds to the relationship:

$$STV = WF_S - WF_A,$$

providing the sample work function with the only knowledge of the instrument parameter $WF_A$.

It is useful to remember that in XPEEM measurements the photon energy $h\nu$ is fixed, whereas STV is continuously scanned. When STV = ΔWF is verified, all the charges

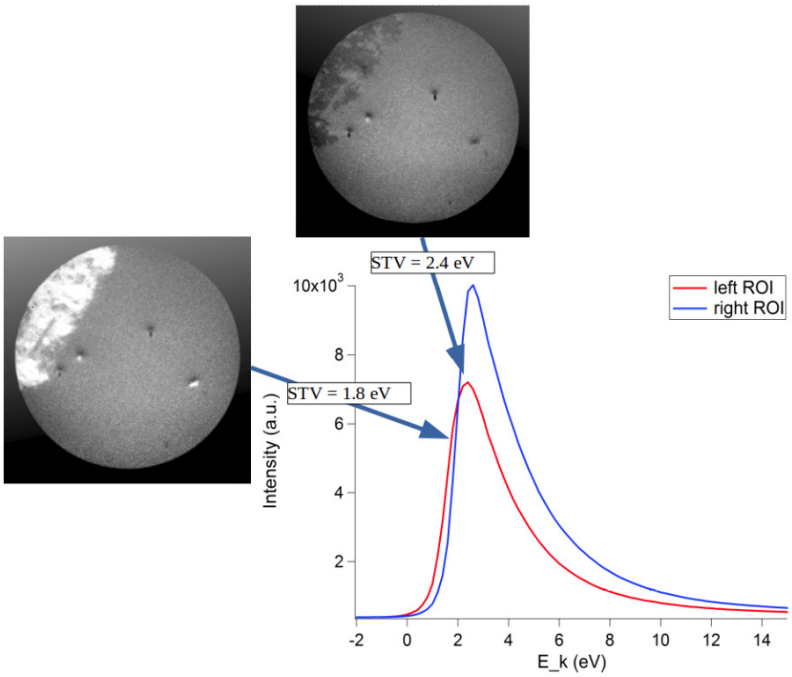


Figure 4.11: XPEEM maps acquired with two different STV and secondary electron cutoffs referred to left and right ROIs (scratched and molybdenum-rich, respectively) on sputtered 30 nm thick $MoO_x$ sample, heated at ~100°C. Scanning the kinetic energy interval it is possible to appreciate the contrast inversion due to different work functions on the surface. FOV = 20 $\mu$m, photon energy = 400 eV.

ejected from the sample can be detected, up to the deepest level permitted by the photon $h\nu$ - taking into account the binding energy $E_B$ and the second-order scattering events.

In a similar way to the element orbitals, scanning secondary electron energies provides sub-micrometer resolved information about the sample characteristics. The example in figure 4.11, referred to the same field of view (FOV) with a molybdenum-poor zone as in figure 4.10, shows the contrast inversion due to different work functions on the surface. Even if the extraction of quantitative data is not straightforward and requires the knowledge of analyzer $WF_A$, this kind of measurement reveals differences in electronic structure within narrow sample areas.

**Valence band** Scanning another appropriate energy interval and lowering the photon energy (for example, to 100 eV for our experimental set-up), it was possible to detect the most external electron ejected from the valence band. This technique provides important information about the sample conductive properties and its metallic nature.

### 4.3.3 XAS

For the analysis of $TiO_2$ samples also X-ray Absorption Spectroscopy was performed, whereas molybdenum oxide is not suitable for this technique due to a different cross section of Mo orbitals. This method was employed as a preparatory technique to locate Ti2p peaks on the energy scale, but the accuracy in $TiO_2$ edge position and the huge amount of XAS data about this compound in literature makes absorption spectra interesting themselves.

Whereas in a typical XAS set-up the light beam is sent on the surface and the transmitted photons are analyzed tracing back to the attenuation coefficient vs energy graph (as shown in figure 4.12a), an alternative technique relying on charge emission was used, illustrated in figure 4.12b. In fact, when X-rays are absorbed by the sample, they eject primary electrons and trigger a series of disexcitation processes toward the

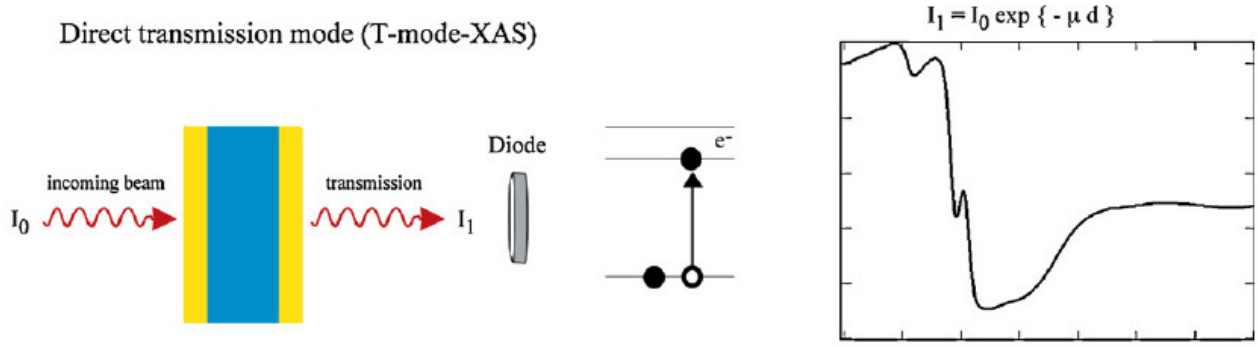


(a) *Transmission X-ray Absorption Spectroscopy: the apparatus measures the radiation intensities of the incident and transmitted beams ($I_0$ and $I_1$, respectively). The former stimulates electron excitations in the material resulting in the re-emission of the latter, as can be seen in the band diagram. On the right, a graph of the detected radiation intensity, collapsing when the incoming photon energy matches the sample absorption edges.*

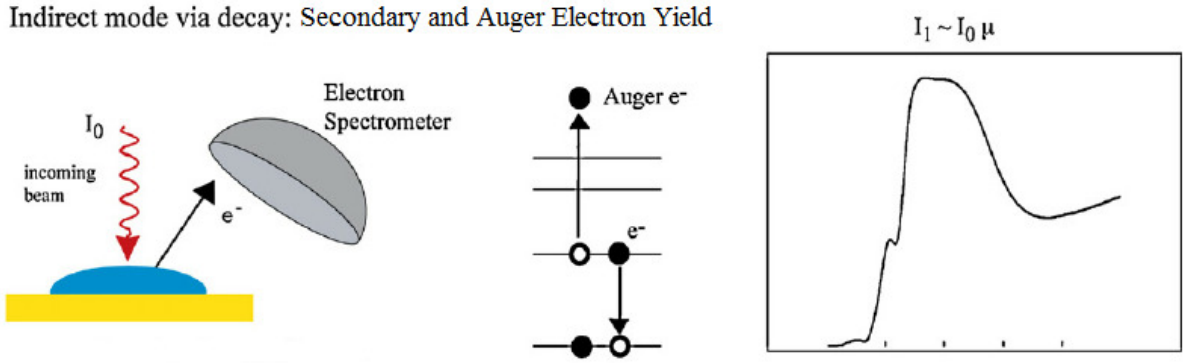


(b) *Secondary/Auger X-ray Absorption Spectroscopy: the apparatus detects the electron yield from the charge emission triggered by the incoming photon beam. The latter stimulates electron excitations in the material resulting in a chain of disexcitation processes with secondary and Auger emissions (an example is visible in the band diagram). On the right a graph of the detected electron beam intensity, upsurging when the incoming photon energy matches the sample absorption edges.*

Figure 4.12: Transmission and Secondary/Auger Electron Yield X-ray Absorption Spectroscopy, with the illustration of typical experimental set-ups, energy band schemes and intensity spectra (after [21]).

stable configuration. The intensity of secondary and Auger electrons emitted during the relaxation is directly linked to the absorption features at different $TiO_2$ edges. Adjusting the undulator parameters to scan a photon energy interval with fixed STV, it is therefore possible to analyze with precision the titanium oxide absorption peaks. At the same time, thanks to the coupling with the XPEEM technique, a 2D map is acquired to record the intensity of secondary/Auger emission for every point on the sample surface.

For the measurements presented in this thesis, the focus was only on absorption peaks from secondary electrons, which provide important information about $TiO_2$ structure and allow to detect crystalline phases as rutile and anatase.

# Chapter 5

# Results and discussion

This chapter addresses at first molybdenum oxide samples, providing an explanation of the different experimental techniques used for their characterization as well as the obtained results. Afterward studies performed on titanium oxide will be presented.

## 5.1 Molybdenum oxide

### 5.1.1 KPFM

#### Protocol

KPFM technique was employed to map both topography and surface potential of molybdenum oxide. Different series of samples were analyzed, all deposited on a square substrate of ∼1 cm×1 cm by the research team at University of Southern Denmark:

1. two samples sputtered on highly doped silicon in 2015, ∼50 nm thick:
   (a) XPS1, a substoichiometric $MoO_x$ with $x \sim 2.6$;
   (b) XPS2, a nearly stoichiometric $MoO_x$ with $x \sim 3$.
2. Four $MoO_x$ samples deposited on ITO (Denmark, end of 2017), ∼30 nm thick, previously analyzed by XPS and UPS as explained later in section 5.1.2:
   (a) SP30RT, sputtered at room temperature;
   (b) SP30-350, sputtered and *in situ* annealed with a slow process (30' at 90°C, 30' at 150°C, 30' at 250°C and 10' at 350°C);
   (c) SP30RT450, sputtered at room temperature and flash annealed in the XPS vacuum chamber at 450°C;
   (d) TH30RT350, thermal deposited at room temperature and annealed in the XPS chamber up to 350°C.

Since the aim of this study was to extract absolute work function data, a reference sample of gold on mica (∼1 cm×1 cm) was prepared by repeated cycles of sputtering and 500°C annealing in the ultra-high vacuum preparation chamber of the Institute of the NanoSciences of Paris. The crystallization in the form of Au111 was checked by LEED analysis.


Figure 5.1: The platelet with the welded metallic tubes containing the contact filament (on the left) and the same platelet with the contacted $MoO_x$ sample on a glass substrate ready for KPFM measurements (on the right).

The sample holder for KPFM was also fabricated: a glass square stuck on a tungsten platelet, next to which two metallic tubes containing the contact filament for the sample were spot welded (see figure 5.1).

Acquisition parameters were chosen:

1. Samples per line: 512;
2. Scan rate: 1 Hz;
3. Lift scan height: 5 nm for the first series of XPS1 and XPS2 measurements because of a previously checked surface roughness of 2-3 nm for Au and not annealed $MoO_x$; 50 nm for the following measurements of all the samples because a growing roughness with annealing temperature was expected[5][6].
4. Scan size: typically 500 nm×500 nm or 2 $\mu$m×2$\mu$m.

The microscope operated in Peak Force - Amplitude Modulation Tapping mode, even if comparison with other instrumental protocols are illustrated in appendix A. In particular, Surface Potential KPFM Tapping mode and the application of different voltages between the tip and the sample were tested.

After their first KPFM exam, XPS1 and XPS2 sample were put in the preparation chamber and annealed from 300°C to 500°C (for XPS2) or 600°C (for XPS1). They were measured again after every annealing step. The initial operating procedure consisted in a series of Au-XPS1- XPS2-Au scans. Nevertheless, last data of XPS1/XPS2 and all the ones of $MoO_x$ on ITO were collected by only molybdenum oxide scanning, as it was impossible to compare KPFM maps of two samples acquired in different tip approaches. In fact, uncontrollable changes of measurement conditions induced modifications of tip-sample interaction and therefore of topography and potential results, so that it proved impossible to extract absolute quantitative data from the maps.

XPS1 and XPS2 annealing cycles consisted in heating the sample in the ultra-high vacuum chamber by means of resistive heating at subsequent temperatures of 300°C, 350°C, 400°C, 450°C and 500°C. XPS1 was also finally annealed at 600°C. Among the different KPFM images, the focus was put on height and potential maps. Complementary information could also be extracted from adhesion data (further details are illustrated in appendix B).

The interesting physical quantities extracted from data by Gwyddion software image analysis were

- *surface roughness* (height differences on the surface due to corrugation),

- *grain dimension* (in terms of diameter, when such features appeared)

from height map;

- *average surface potential*,
- *difference between average potentials* on Au and $MoO_x$ surfaces (for XPS1/XPS2 only)
- *potential contrast* (CPD differences between different sites on a single sample)

from potential map.

Average potential level on $MoO_x$ and Au/$MoO_x$ potential difference conspicuously changed whenever a new measurement was performed, with oscillations of more than 500 mV without any regularity. For example, potential of XPS1 could range from less than -300 mV to ∼-50 mV, XPS2 potential from ∼-350 mV to ∼250 mV and Au/$MoO_x$ potential difference from ∼-130 mV to ∼370 mV. It was therefore decided not to consider absolute CPD values nor Au/$MoO_x$ CPD differences, but to focus just on potential contrast. As a consequence, for the last series of measurements ($MoO_x$ on ITO) a gold reference was not even planned.

Gwyddion software was used to elaborate acquired images by methods like flattening, line averaging, polynomial background removal and profile extraction[22]. It is useful to illustrate how physical quantities were calculated and how their associated error was estimated. With regard to grain diameter, three different methods were tested:

- direct image segmentation by thresholding, which did not give any good result because of blurry grain boundaries and different height of the aggregates;
- profile analysis (profile tracing and evaluation of horizontal distance between peaks and valleys), which was not straightforward due to small-scale features;
- direct diameter tracing and measuring on the image, which proved to be the most reliable method.

After acquiring various images on the same sample at different surface sites, the analysis was performed on the best-quality ones (with low degree of thermal drift and potential map readability). The diameters of many surface aggregates were traced and measured, trying to include every grain size proportionally to its abundance; then mean and standard deviation were calculated. An example of this procedure is visible in figure 5.2. This method allows to detect and manually select the more representative features of the materials and prevents somehow arbitrary values that an automatic computer analysis risks extracting. This is particularly true in the case of surfaces with little grains clustering together in the form of aggregates as the ones under examination.

The analysis procedure employed for every annealing temperature to extract surface roughness and potential contrast implied

1. tracing about ten profiles of representative steps on the collection of images for every sample, as can be seen in figures 5.3a and 5.3c in height and potential maps;
2. calculating differences between the highest and the lowest point in the profiles (an example for topography and CPD is shown in figure 5.3b and 5.3d);

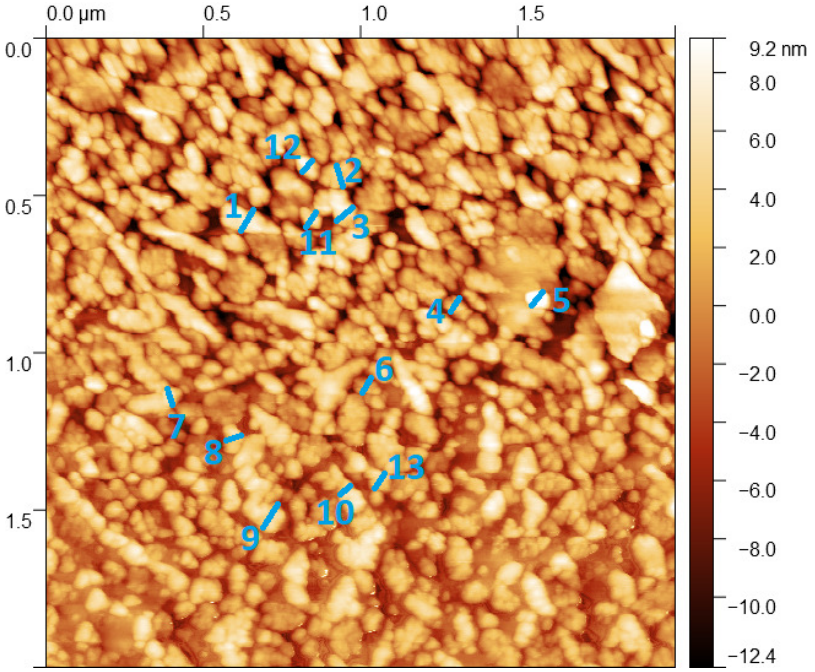


Figure 5.2: Example of average grain diameter calculation on topographical 2 $\mu$m×2 $\mu$m image of a $MoO_x$ sample (450°C annealed XPS1). In this case, thirteen profiles were traced trying to capture representative grains; the measured diameters were then averaged with values extracted from the other images of the same sample. Color scale from -12.4 nm (black) to 9.2 nm (white).

3. associating an error to the two extremes according to the perceivable profile fluctuation around the chosen heights (two scale divisions if the profile was reasonably stable) and summing the two uncertainties to get the whole roughness error;

4. calculating the weighted average and its associated error to obtain the final roughness evaluation.

This method depends on the difficulty in quantitative data extraction from images and results in a large error bar associated to every measure.

It is worth specifying that what is called *roughness* in this study is not the quantity typically calculated by image processing software - often referred to as *RMS roughness*, which is the root mean square of height irregularities, computed from data variance[23]. In fact, this quantity takes into account the totality of height variations on the surface and it is difficult to select only features due to grain boundaries. It was therefore preferred to individually select and analyze step profiles of relevant structures to obtain a reliable estimation of grain height.

In order to double-check results, KPFM measurements were repeated at Physics and Astronomy Department of the University of Bologna, using a Park instrument. Three different samples were taken into consideration, all 30 nm thick, prepared in Denmark at the end of 2017:

- $MoO_x$ on ITO, thermal deposited at room temperature;
- $MoO_x$ on ITO, thermal deposited and *in situ* annealed at 350°C;
- $MoO_x$ on silicon, sputtered and *in situ* annealed at 350°C.

The acquisition was performed at a 0.4 Hz scan rate, with 512 samples per line and 2 $\mu$m×2 $\mu$m maps were recorded. The different operating principle of Park microscope allowed to carry out the whole measurement with a single scan on every line. After image treatment by line averaging, grain sizes were obtained with the aforementioned method, while for roughness the difference between the minimum and the average surface height

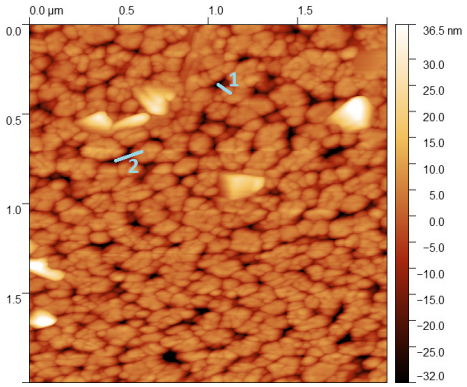


(a) *Two profiles were traced on this topographical image, trying to capture whole steps from the grain center to a background site far away from the grain, in order to avoid boundary effects. The highest grains (in light yellow with this color map) have been considered as peculiar features to be analyzed separately, not as normal grains to be included in the average roughness calculation. Size: 2 µm×2 µm; color scale from -32.0 nm (black) to 36.5 nm (white).*

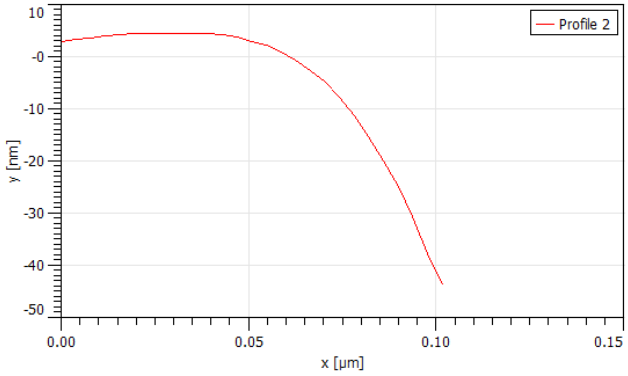


(b) *Profile corresponding to step 2 in the topographical map 5.3a. The level difference between the highest and the lowest points was evaluated to be 47 nm and an error of two vertical scale divisions was associated to every point (total error of 4 nm).*

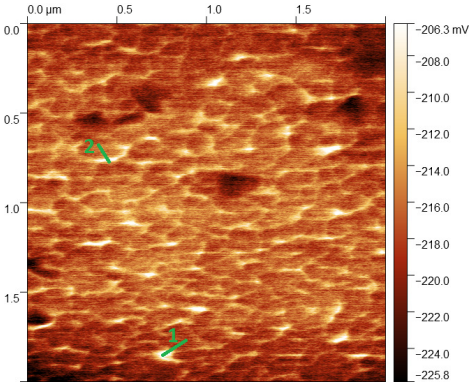


(c) *Two profiles were traced on this potential image, trying to capture whole steps from the 'potential grain' center to a background site far away from the grain, in order to avoid boundary effects. The lowest potential areas (dark brown in this color map) were considered as peculiar features to be analyzed separately, not as normal CPD steps to be included in the average potential roughness calculation. Size: 2 µm×2 µm; color scale from -225.8 mV (black) to -206.3 mV (white).*

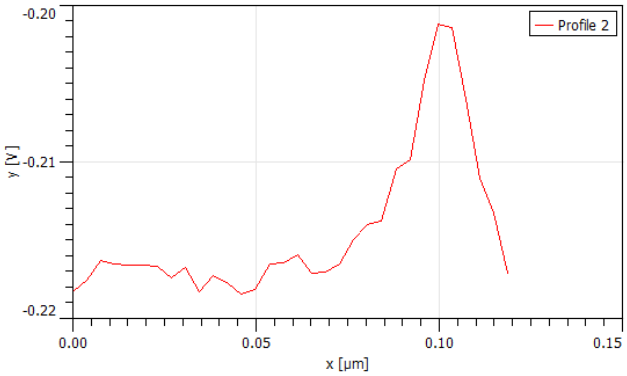


(d) *Potential profile corresponding to step 2 in the CPD map 5.3c. The level difference between the highest and the lowest points was evaluated to be 17 mV and an error of two vertical scale divisions was associated to every point (total error of 4 mV).*

Figure 5.3: Example of profile tracing and roughness estimation on a height and potential images of a $MoO_x$ sample (500°C annealed XPS1).

calculated by Gwyddion analysis software was considered - which proved to be a reliable estimation compared to the analysis of selected grain profiles.

In the case of potential maps, it was not possible to distinguish any kind of feature on the surface, so that different horizontal and vertical profiles were traced to extract mean CPD. Since we knew the microscope tip composition (Au), we could derive an estimation of sample work function $WF_{sample}$ applying the relationship

$$\Phi_{sample} - \Phi_{Au} = 5.30eV - WF_{sample},$$

where $\Phi_{sample}$ and $\Phi_{Au}$ are surface potentials measured on $MoO_x$ and on a test gold sample by the same tip and 5.30 eV is a reference value for Au work function[24].

Unlike work function measurements performed with the first instrument, it has been chosen to present these ones because of the better stability verified for a series of maps, whereas the results should be regarded as rough estimations due to the high level of noise in the images and technical impossibility to heat samples at 100-200°C in vacuum to desorb carbon contaminants.

### Results

In figures 5.4-5.8 images of XPS1/XPS2 and $MoO_x$ on ITO are shown both for height and potential maps, following the annealing steps they underwent. For XPS1 and XPS2 two sizes of image can be seen, 500 nm×500 nm and 2 $\mu$m×2 $\mu$m: surface aggregation at the highest annealing temperatures made it more useful to acquire a wider map.

For both XPS1 and XPS2, samples are quite flat at room temperature and their CPD is homogeneous (figures 5.4a e b, 5.6a e b). During the annealing procedure some interesting features appear on the surface and nanoaggregates form and expand, with a corresponding contrast in potential maps. However, this process is more evident in the case of nearly stoichiometric XPS2.

On the other hand, molybdenum oxide on ITO shows similar surface grains both in shape and in size for every annealing stage and CPD is almost flat in every measurement (figure 5.8), except for SP30-350, with grains slightly different from other samples in shape (figure 5.8b).

Figure 5.9 presents surface morphology maps for the three $MoO_x$ samples measured in Bologna, whereas potential images are not reported due to their uniform high level of noise in which no interesting structure could be detected.

### Discussion

In tables 5.1-5.3 grain diameter, surface roughness and potential contrast are summarized according to either different annealing temperatures or sample name.

| XPS1 | $T_{room}$ | 300°C | 350°C | 400°C | 450°C | 500°C | 600°C |
|---|---|---|---|---|---|---|---|
| Grain diameter (nm) | 28±7 | 21±5 | 25±5 | 46±18 | 71±16 | 80±30 | 110±60 |
| Roughness (nm) | 2.3±1.2 | 7±3 | 10±4 | 9±3 | 22±11 | 40±10 | 59±7 |
| Potential contrast (mV) | homogeneous | 8±5 | 4±2 | 5±4 | 17±12 | 17±10 | 15±10 |

Table 5.1: XPS1 sample: physical quantities measured by KPFM.

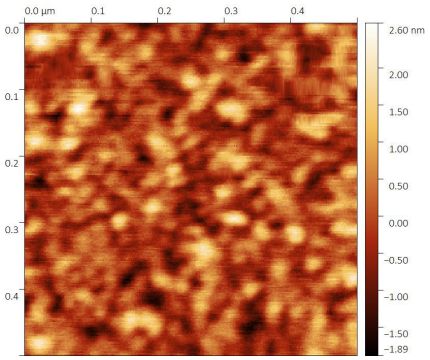


(a) *Morphology map of room temperature (not annealed) sample, treated by line averaging and horizontal scar removal; color scale from -1.89 nm (black) to 2.60 nm (white).*

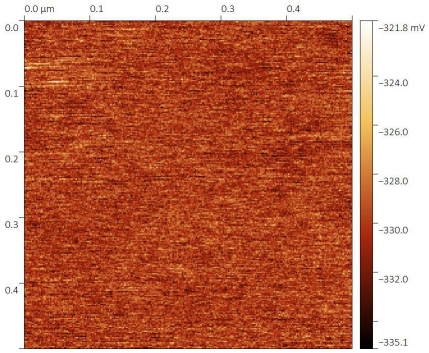


(b) *Potential map of room temperature (not annealed) sample, treated by flattening and line averaging; color scale from -335.1 mV (black) to -321.8 mV (white).*

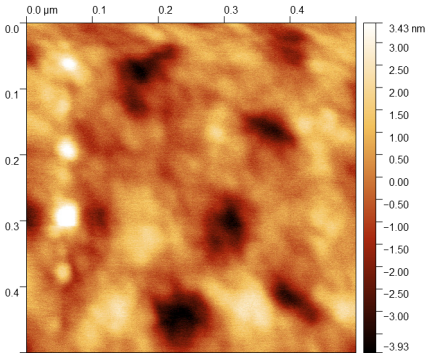


(c) *Morphology map of sample annealed at 300°C. The image was treated by line averaging; color scale from -3.93 nm (black) to 3.43 nm (white).*

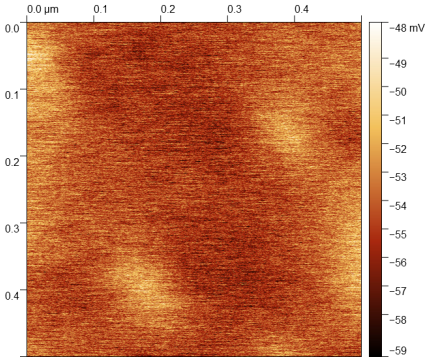


(d) *Potential map of sample annealed at 300°C. The image was treated by line averaging; color scale from -59 mV (black) to -48 mV (white).*

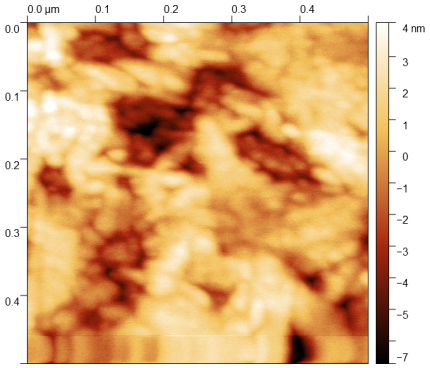


(e) *Morphology map of sample annealed at 350°C. The image was treated by line averaging; color scale from -7 nm (black) to 4 nm (white).*

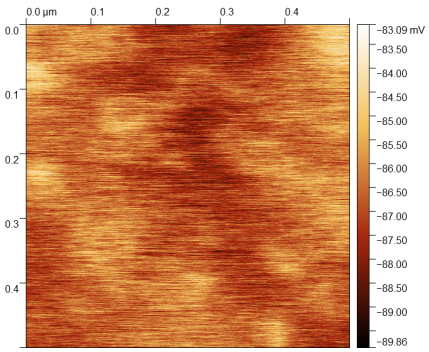


(f) *Potential map of sample annealed at 350°C. The image was treated by line averaging; color scale from -89.86 mV (black) to -83.09 mV (white).*

Figure 5.4: Height and potential maps of substoichiometric XPS1, during annealing steps from RT to 350°C (size: 500 nm×500 nm).

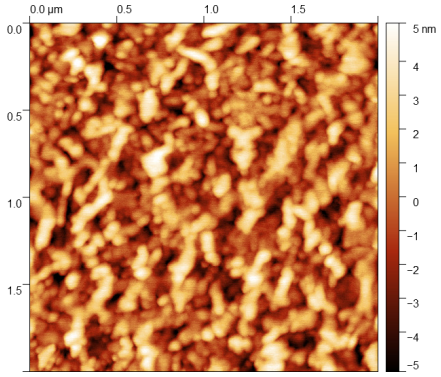


(a) *Morphology map of sample annealed at 400°C. The image was treated by line averaging; color scale from -5 nm (black) to 5 nm (white).*

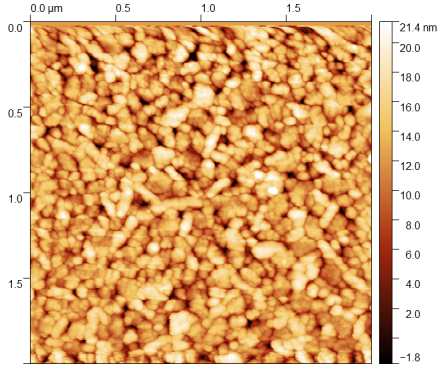


(b) *Morphology map of sample annealed at 450°C. The image was treated by line averaging; color scale from -1.8 nm (black) to 21.4 nm (white).*

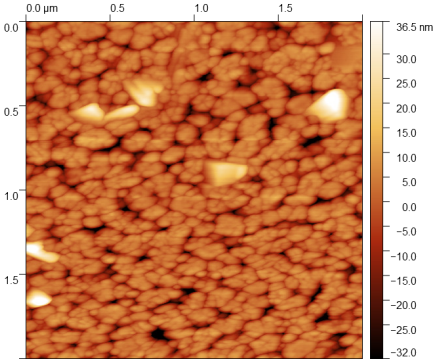


(c) *Morphology map of sample annealed at 500°C. The image was treated by line averaging; color scale from -32.0 nm (black) to 36.5 nm (white).*

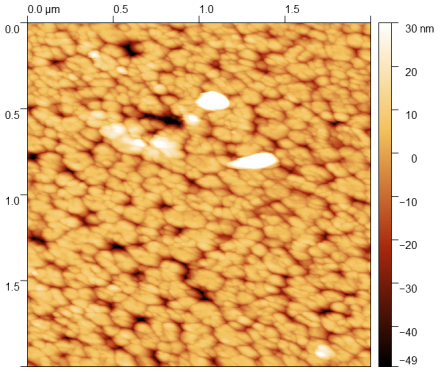


(d) *Morphology map of sample annealed at 600°C. The image was treated by line averaging; color scale from -49 nm (black) to 30 nm (white).*

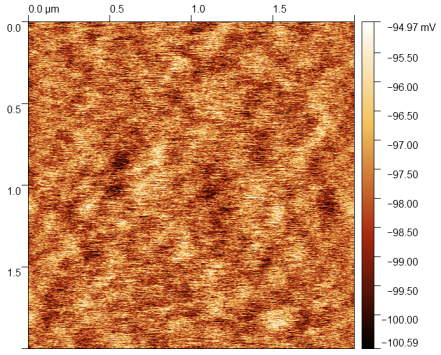


(e) *Potential map of sample annealed at 400°C. The image was treated by line averaging; color scale from -100.59 mV (black) to -94.97 mV (white).*

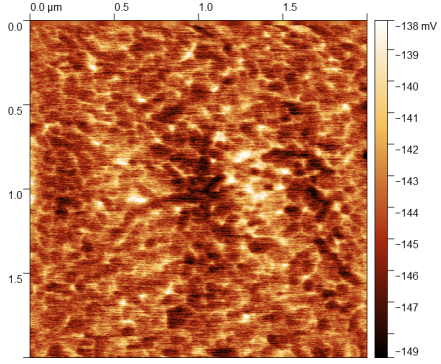


(f) *Potential map of sample annealed at 450°C, treated by line averaging; color scale from -149 mV (black) to -138 mV (white).*

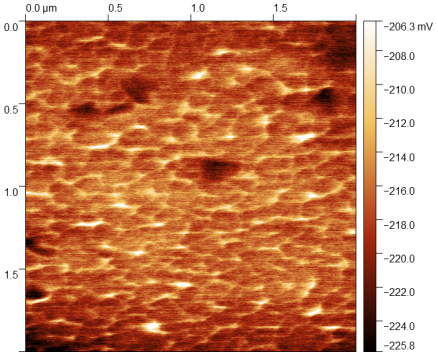


(g) *Potential map of sample annealed at 500°C, treated by flattening; color scale from -225.8 mV (black) to -206.3 mV (white).*

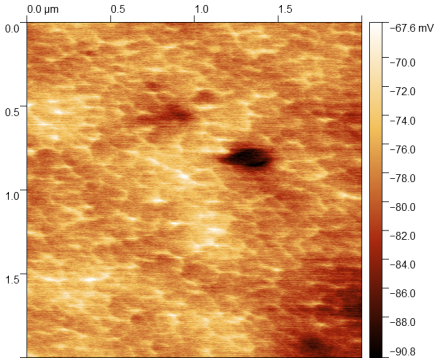


(h) *Potential map of sample annealed at 600°C, treated by line averaging; color scale from -90.8 mV (black) to -67.6 mV (white).*

Figure 5.5: Height and potential maps of substoichiometric XPS1, during annealing steps from 400 to 600°C (size 2 $\mu$m×2 $\mu$m).

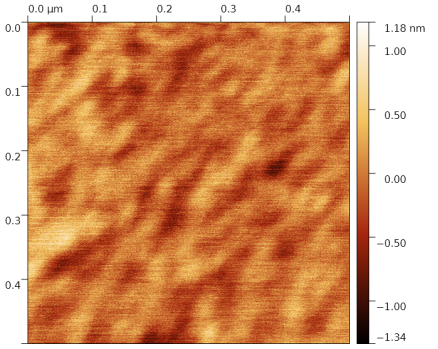


(a) *Morphology map of room temperature (not annealed) sample. The image was treated by line averaging; color scale from -1.34 nm (black) to 1.18 nm (white).*

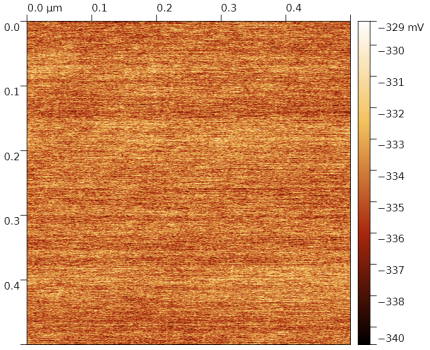


(b) *Potential map of room temperature (not annealed) sample, treated by flattening; color scale ranges from -340 mV (black) to -329 mV (white).*

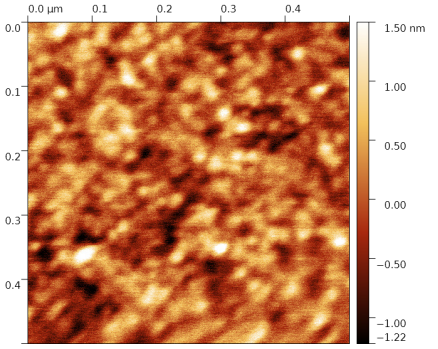


(c) *Morphology map of sample annealed at 300°C. The image was treated by line averaging; color scale from -1.22 nm (black) to 1.50 nm (white).*

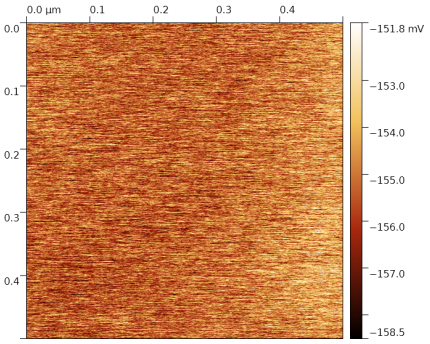


(d) *Potential map of sample annealed at 300°C, treated by line averaging; color scale from -158.5 mV (black) to -151.8 mV (white).*

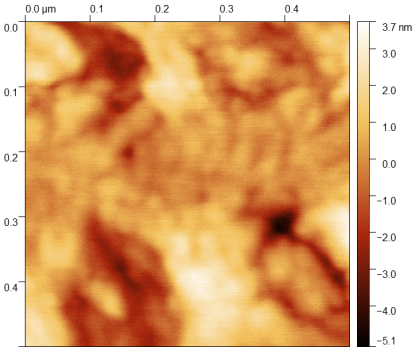


(e) *Morphology map of sample annealed at 350°C. The image was treated by line averaging; color scale from -5.1 nm (black) to 3.7 nm (white).*

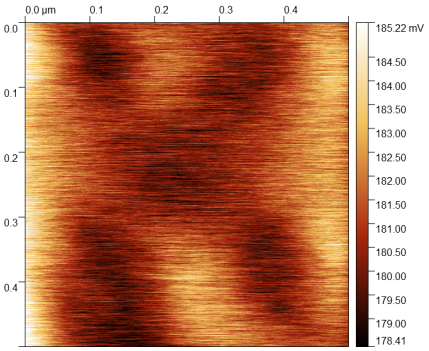


(f) *Potential map of sample annealed at 350°C. The image was treated by flattening and line averaging; color scale from 178.41 mV (black) to 185.22 mV (white).*

Figure 5.6: Height and potential maps of nearly stoichiometric XPS2, during the annealing steps from RT to 350°C (size: 500 nm×500 nm).

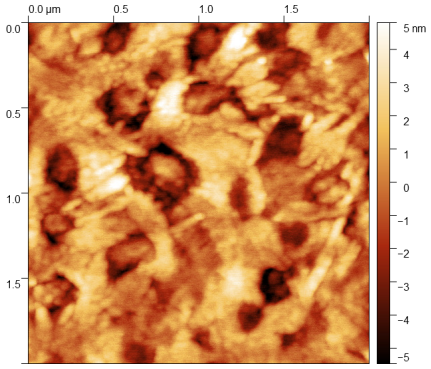


(a) *Morphology map of sample annealed at 400°C. The image was treated by line averaging; color scale from -5 nm (black) to 5 nm (white).*

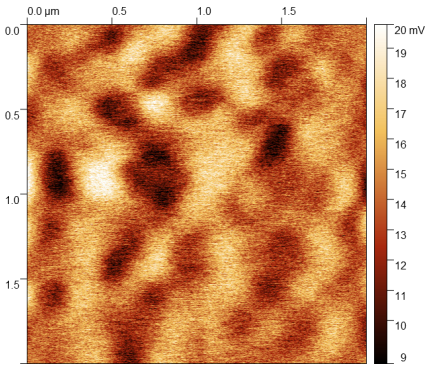


(b) *Potential map of sample annealed at 400°C. The image was treated by line averaging; color scale from 9 mV (black) to 20 mV (white).*

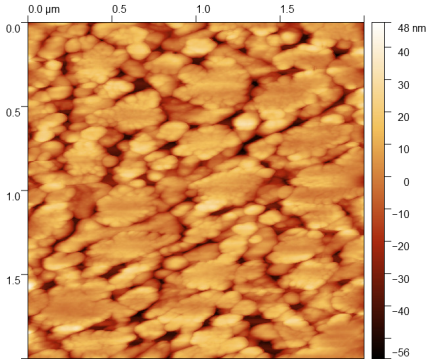


(c) *Morphology map of sample annealed at 450°C. The image was treated by line averaging and horizontal scar removal; color scale from -56 nm (black) to 48 nm (white).*

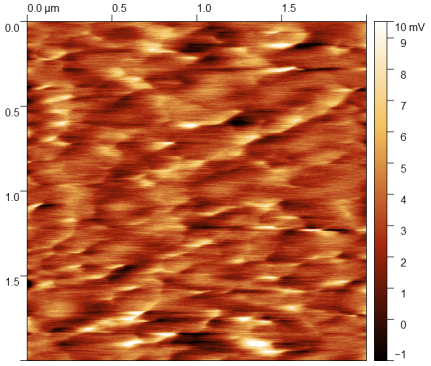


(d) *Potential map of sample annealed at 450°C. The image was treated by line averaging; color scale from -1 mV (black) to 10 mV (white).*

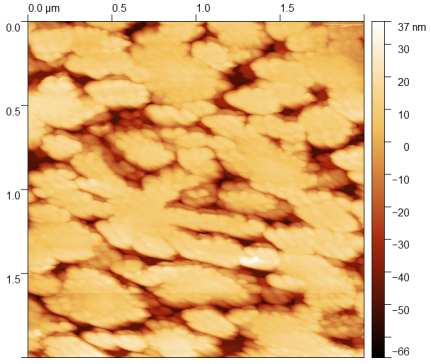


(e) *Morphology map of sample annealed at 500°C. The image was treated by polynomial background removal; color scale from -66 nm (black) to 37 nm (white).*

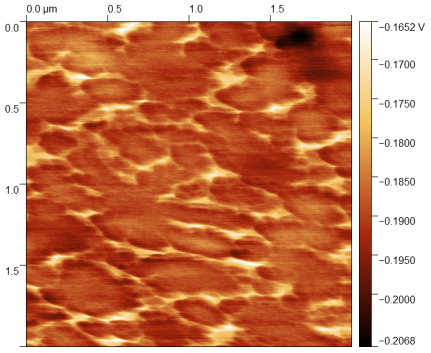


(f) *Potential map of sample annealed at 500°C. The image was treated by line averaging; color scale from -206.8 mV (black) to -165.2 mV (white).*

Figure 5.7: Height and potential maps of nearly stoichiometric XPS2, during the annealing steps from 400 to 500°C (size: 2 $\mu$m×2 $\mu$m).

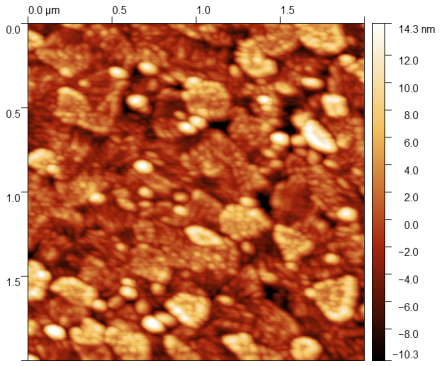


(a) *Morphology map of not annealed sputtered sample (SP30RT); color scale ranges from -10.3 nm (black) to 14.3 nm (white).*

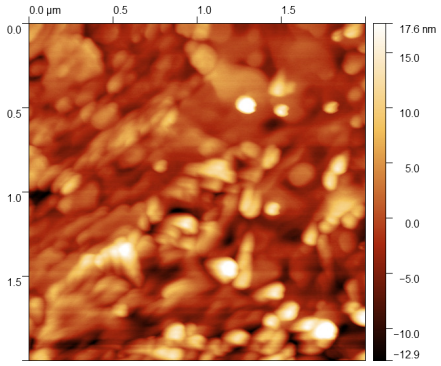


(b) *Morphology map of sputtered sample in situ annealed at 350°C (SP30-350); color scale ranges from -12.9 nm (black) to 17.6 nm (white).*

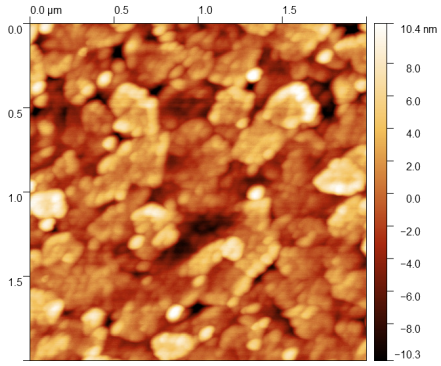


(c) *Morphology map of 450°C flash annealed sputtered sample (SP30RT450); color scale ranges from -10.3 nm (black) to 10.4 nm (white).*

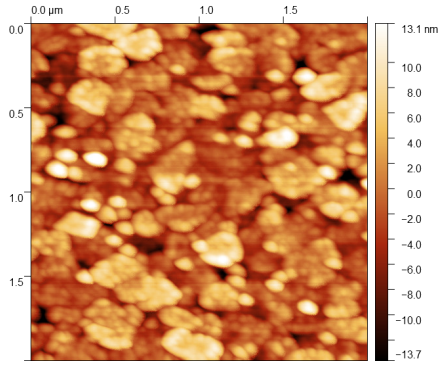


(d) *Morphology map of 350°C annealed thermal deposited sample (TH30RT350); color scale ranges from -13.7 nm (black) to 13.1 nm (white).*

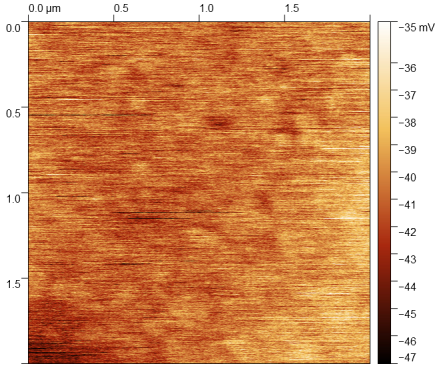


(e) *Potential map of not annealed sputtered sample (SP30RT); color scale ranges from -47 mV (black) to -35 mV (white).*

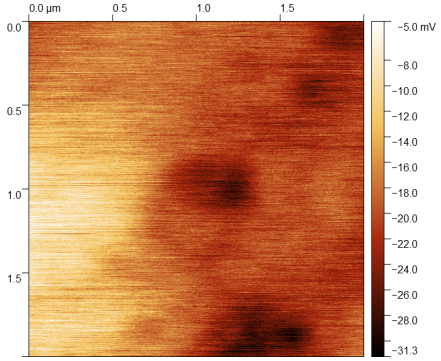


(f) *Potential map of sputtered sample in situ annealed at 350°C (SP30-350); color scale from -31.3 mV (black) to -5.0 mV (white).*

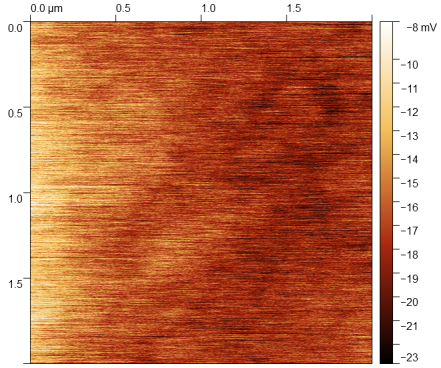


(g) *Potential map of 450°C flash annealed sputtered sample (SP30RT450); color scale ranges from -23 mV (black) to -8 mV (white).*

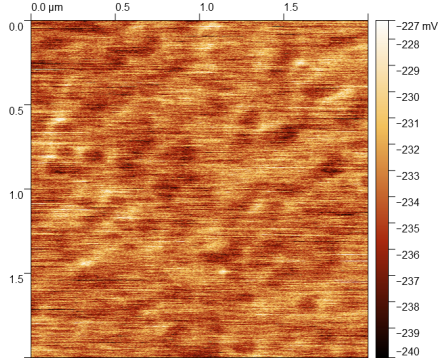


(h) *Potential map of 350°C annealed thermal deposited sample (TH30RT350); color scale ranges from -240 mV (black) to -227 mV (white).*

Figure 5.8: 2 $\mu$m×2 $\mu$m KPFM images of 30 nm thick $MoO_x$ on ITO samples. All the images are treated by line averaging.

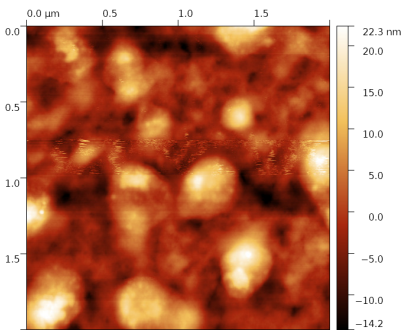


(a) *Morphology map of room temperature thermal deposited sample on ITO. The image was treated by line averaging; color scale from -14.2 nm (black) to 22.3 nm (white).*

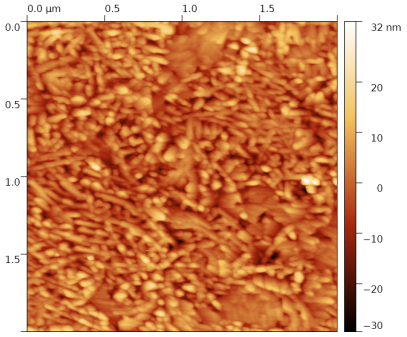


(b) *Morphology map of thermal deposited sample annealed at 350°C on ITO. The image was treated by line averaging; color scale from -30 nm (black) to 32 nm (white).*

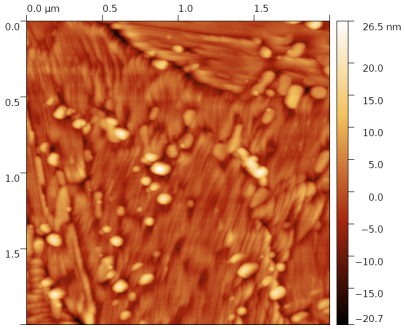


(c) *Morphology map of sputtered sample annealed at 350°C on silicon. The image was treated by line averaging; color scale ranges from -20.7 nm (black) to 26.5 nm (white).*

Figure 5.9: Height maps of different 30 nm thick $MoO_x$ samples, obtained at the University of Bologna (size: 2 $\mu$m×2 $\mu$m).

| XPS2 | $T_{room}$ | 300°C | 350°C | 400°C | 450°C | 500°C |
|---|---|---|---|---|---|---|
| Grain diameter (nm) | 21±3 | 21±3 | 27±5 | 44±12 | 110±60 | 220±70 |
| Roughness (nm) | 1.8±0.9 | 2.7±0.8 | 8±2 | 9±3 | 59±18 | 59±19 |
| Potential contrast (mV) | homogeneous | homogeneous | 7±5 | 11±9 | 10±7 | 22±9 |

Table 5.2: XPS2 sample: physical quantities measured by KPFM.

| 30 nm $MoO_x$ on ITO | SP30RT | SP30-350 | SP30RT450 | TH30RT350 |
|---|---|---|---|---|
| Grain diameter (nm) | 37±11 | 90±20 | 63±11 | 56±13 |
| Aggregate diameter (nm) | 160±30 | | 190±50 | 170±40 |
| Roughness (nm) | 19±6 | 15±5 | 15±5 | 22±6 |
| Potential contrast | hom. | hom. | hom. | hom |

Table 5.3: Physical quantities of 30 nm thick $MoO_x$ samples on ITO measured by KPFM.

For high temperatures, the diameter of large grains was considered: even if it is still possible to distinguish subgrains inside them, the significant event is that aggregates melt together. Nevertheless, in the case of $MoO_x$ on ITO, table 5.3 displays dimensions of both aggregates and elemental grains within them.

In the case of comparison measurements carried out in Bologna, a summary of morphology and potential results is visible in table 5.4. Since the values only aim at providing a double-check confirmation of the ones obtained in Paris, any detailed error analysis has not been carried out. For the sample deposited on silicon the grain size data are referred to round structures distinguishable on the topography in figure 5.9c, even though the surface is unexpectedly dominated by filament-like grains with a length between 250 and 650 nm and a width of ∼20 nm, which was not observed in XPS1 and XPS2 morphologies.

In any case, the order of magnitude of the present morphological properties is in satisfactory agreement with the results of KPFM performed at INSP, so that we can confirm their reliability. Also extracted values of oxide work function are in the same range of the more rigorous ones from UPS reported below in section 5.1.2, but caution is required in the evaluation of these data due to the high noise levels which could not be removed changing experimental parameters, the considerable presence of surface contamination in air and the difficulty to choose a unique reference value for gold work function - a wide range of data can be found in literature according to measurement method and conditions and crystalline structure of samples[24]. At this regard, further procedures of surface treatment like vacuum annealing combined with polymeric coating are still ongoing in order to reduce sample coverage of adsorbates in KPFM measurements in air.

| | Th RT on ITO | Th 350°C on ITO | Sp 350°C on Si |
|---|---|---|---|
| Grain diameter (nm) | 170 | 50 (aggregates ∼ 200) | 70 |
| Roughness (nm) | 16 | 25 | 24 |
| Work function (eV) | 5.4 | 5.3 | 5.3 |

Table 5.4: Physical quantities of 30 nm thick $MoO_x$ samples measured by KPFM at the University of Bologna.

To highlight the influence of thermal treatment, plots 5.10a and 5.10b display how grain diameter and roughness evolve with annealing temperature for $MoO_x$ deposited on silicon (XPS1 and XPS2). Up to ∼400°C the two samples have similar topographical characteristics and surfaces are quite flat. The turning point in annealing cycle is around 400°C: from here onwards nanoaggregates grow larger and surface corrugation continues increasing. Moreover, XPS2, with a greater oxygen content in its stoichiometry, reveals more apparent features than substoichiometric XPS1, for example a double roughness at 450°C and a triple grain diameter at 500°C. This fact is consistent with previous research conclusions[5][6] and suggests an important role of oxygen in triggering and helping grain nucleation.

XPS1 and XPS2 potential data are not as clear to analyze and no definitive conclusion could be extrapolated within error intervals. In this context a more precise experimental technique is needed, even if it seems that potential differences between surface sites increase during annealing in relation to morphology changes (other potential contrast

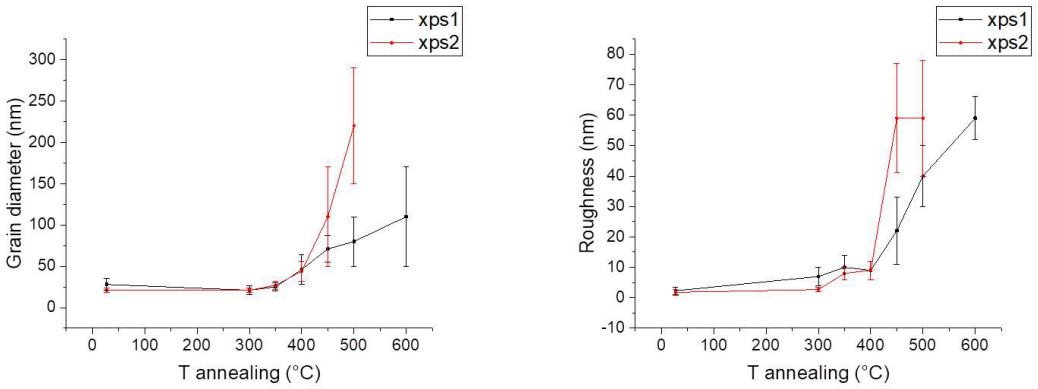


(a) *Grain size evolution according to annealing temperature for XPS1 and XPS2.*

(b) *Surface roughness evolution according to annealing temperature for XPS1 and XPS2 .*

Figure 5.10: Topography evolution during annealing treatment on XPS1 and XPS2.

measurements on XPS2 annealed at 500°C as explained in appendix A gave values of (29±6) mV and (31±8) mV).

However, it can be hypothesized that CPD differences on the sample are caused by capacitive artifacts directly linked to topographical features. In fact, surface valleys and peaks can act as 'physical traps' for charges or channel their distribution on the sample, so that potential maps closely resemble morphology ones.

In any case, some of the CPD scans seem to reveal further differences on the surface which do not mirror oxide topographical structure: for example, zones of low and high potential larger than surface grains (hundreds of nanometers) are slightly distinguishable in figure 5.5f and 5.5h referred to XPS1 sample. Nonetheless, the important presence of adsorbates such as carbon contaminants makes it difficult to reach any conclusion about the relation between these areas of different potential and the substoichiometric grains with a variety of work functions demonstrated in ref. [6].

About the discrepancies between data extracted for silicon and ITO-deposited samples, a screening effect determined by Si can be assumed. In fact, the correspondence between topography and potential maps grows more evident with annealing temperature for Si-deposited samples, whereas CPD maps remain almost flat in the case of ITO.

Further more, silicon substrate differs from ITO in its flatness that allows deposited oxide to develop grain features during annealing according to its own aggregation mechanisms, whereas the already corrugated ITO surface limits this process. Examples of ITO AFM maps revealing closely resemblance to the topography of subsequently deposited $MoO_x$ are shown in ref. [26].

As a consequence, roughness is stable during annealing for ITO-deposited samples at around 20 nm, which does not result in potential contrast, while peak-valley differences on Si reach ∼60 nm for the last annealing steps, so that clearer correspondence in CPD maps can be detected due to the aforementioned capacitive artifacts. This systematic study therefore reveals the role of the substrate in determining morphological and electrical properties of the samples.

Appendix B provides a more detailed discussion about the influence of grain boundaries in potential measurements and additional elements extracted by adhesion map analysis.

As to $MoO_x$ on ITO, the annealing temperatures of 350°C and 450°C were chosen

because in this interval XPS1/XPS2 showed the most important roughness and grain size changes. On the contrary, these properties are quite constant regardless of the deposition technique on ITO. In fact, according to table 5.3 and to the images in figure 5.8, the four samples do not exhibit a clear evolution during the annealing treatment nor any difference between thermal deposited and sputtered $MoO_x$, inside the error bar range. The grain size - especially aggregate dimension - does not evidently change during heating. Besides, topographical roughness is similar for every sample and potential maps are almost flat, revealing a very homogeneous surface despite of thermal treatment.

As already stated, for oxides deposited both on silicon and on ITO, the difficulty to detect any potential feature might be due to the amount of carbon contamination on the surface, since KPFM is not used in vacuum or under controlled atmosphere: absolute CPD values are therefore not reproducible nor reliable and potential contrast evolution during annealing is limited to few millivolt.

In general, KPFM results suggest that photoemission studies as XPS and synchrotron XPEEM are crucial to enhance CPD measurement resolution, to achieve absolute surface work function values and to provide a deeper insight into chemical sample characteristics and their evolution during annealing.

### 5.1.2 XPS/UPS

#### Protocol

Different ITO-deposited $MoO_x$ samples were studied - the ones already mentioned in section 5.1.1. In the presentation of the following results, the series of measurements on RT sputtered $MoO_x$ is regarded as unique even if annealing at different temperatures was performed on separate samples up to 450°C.

The series of measurements involved:

1. an overview of a large energy interval under monochromatic X-rays ($K_{\alpha_1}$ aluminum emission line, with $h\nu = 1486.70$ eV);

2. detailed scans around the energies of different elements (especially Mo3d and O1s, but also carbon C1s to check the level of contamination);

3. UPS scan for valence band measurement ($h\nu = 21.22$ eV);

4. UPS secondary electron cutoff scan with a sample bias of -18 V for work function extraction;

5. XPS scan after UPS measurements, to analyze the effect of UV exposure.

After spectra acquisition, all XPS and UPS data were plotted versus binding energy $B_E$. Fermi level was located by gold reference (Au111) calibration to provide a fixed zero for $B_E$ scale: it is worth noting that this is not the samples' $E_F$, which varies during annealing treatment with valence band and intra-gap state evolution, as explained in the following.

Molybdenum peaks were analyzed by multiple Voigt function fit and subtraction of Shirley background (a model whose intensity is proportional to the total peak area summed over the range of lower binding energies[27]), the percentages and energy positions of different oxidation states - $Mo^{6+}$, $Mo^{5+}$ and $Mo^{4+}$ - were finally extracted and are summarized in table 5.5.

Experimental error was estimated at 133 meV from Fermi energy width of Ag reference for UPS and at 0.6 eV from fwhm (full width at half maximum) of $Ag3d_{5/2}$ peak for XPS. Moreover, the presence of carbon contaminants was observed from the peak C1s around an energy of 284.2 eV, as visible in figure 5.11 for the annealing cycle of sputtered $MoO_x$.

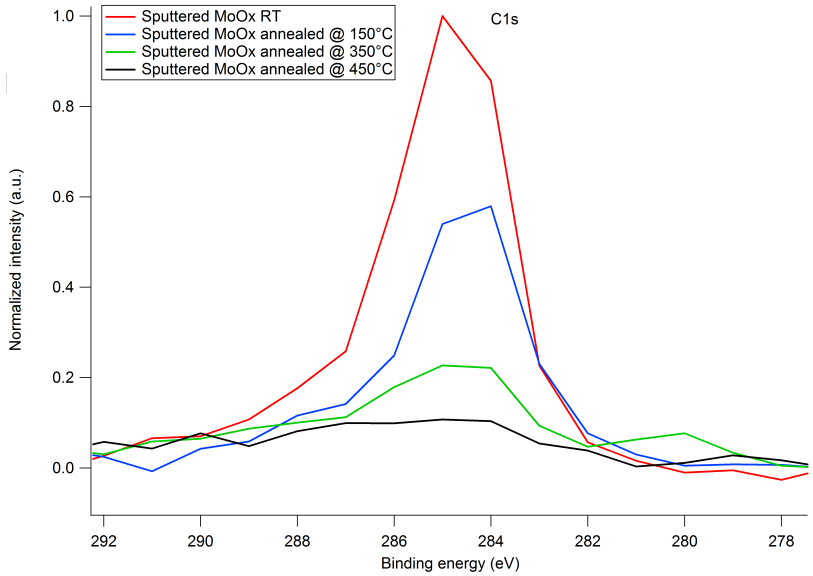


Figure 5.11: Evolution of C1s peak for the RT sputtered $MoO_x$ at different annealing temperatures. It is evident the decrease of the carbon peak during sample heating.

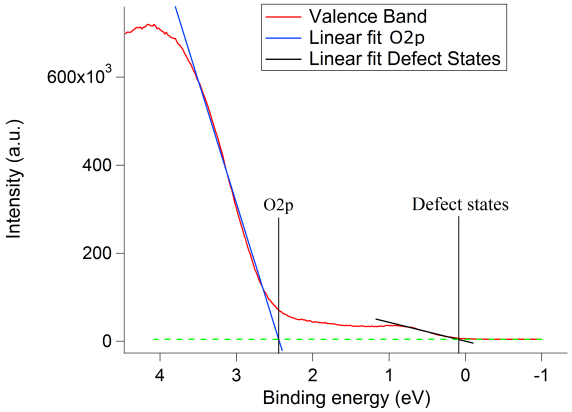


Figure 5.12: Zoom on the valence band edge for RT sputtered $MoO_x$ annealed at 450°C. Two different linear fits are needed to detect the respective energies of valence orbitals arising from O2p and defect states (from the intersection with the background intensity).

From secondary electron cutoff of UPS measurements with sample bias, the oxide work functions can be obtained using the expression 4.3 in section 4.2. As in the example provided in figure 4.7 (section 4.2), in order to extract the position of secondary electron cutoff only the main slope was considered, whereas the minor edge at lower binding energies is probably due to ITO substrate.

From UPS scans at zero potential it appears that valence band edge is not well defined and that in addition to a sharp cutoff there is at least another structure at lower binding energies (as in the example in figure 5.12). Separate linear fits are thus needed to extract their positions, expressed relatively to gold $E_F$ determined in the same experimental conditions.

In order to compare some of the XPS/UPS data with analogue results from literature referred to samples on silicon[25] we also analyzed previous measurements performed at LRS in 2016 for $MoO_x$ on Si[6], calculating work functions and O:Mo ratios. Two different samples were considered, thermal deposited and sputtered ones, both of which underwent annealing at 210°C and 500°C. The experimental protocol was similar to the one described above, with the only difference that calibration was made with Ag Fermi level and a bias of -10 eV was applied for secondary cutoff spectra.

### Results

The series of charts in figure 5.13, referred to thermal deposited $MoO_x$, shows the evolution of Mo3d spin-orbit double peak after every annealing step (room temperature, 150°C and 350°C) and compares the oxidation states before and after UV exposure at 21.22 eV. Similar graphs have been obtained for sputtered oxides. Extracted quantitative results are displayed in table 5.5.

In the figure 5.13a two peaks, at high and low binding energies, respectively correspond to $Mo3d_{3/2}$ and $Mo3d_{5/2}$ orbitals. Red areas are fit results for $Mo^{6+}$ oxidation degree, the unique component in a stoichiometric $MoO_3$, whereas blue ones refer to $Mo^{5+}$, which produces shoulder features in the low $E_B$ region of the total fit function (envelope in black dashed line) for experimental data (green solid line). This is linked to oxide reduction and associated chemical shift.

At high annealing temperatures, as for figure 5.13e, an additional feature attributed to $Mo^{4+}$ states occurs at even lower binding energies, an evidence of further reduction in the sample.

From the provided example it is clear that peaks change during thermal treatment. The initial well-defined shapes become broader with right shoulder appearance, especially evident at 350°C. Also peak positions evolve: whereas for raw sample (fig. 5.13a) an almost total correspondence between experimental $Mo3d_{3/2}$/$Mo3d_{5/2}$ and $Mo^{6+}$ fit components is visible at approximated energies of 233 and 236.2 eV, the total peaks move to the right on $E_B$ scale with increasing heating temperature, due to the growing proportion of $Mo^{5+}$ and $Mo^{4+}$ oxidation states. Slight changes with displacement to lower binding energies and increased percentages of reduced states can also be seen comparing spectra before and after beam exposure at equivalent temperatures.

### Discussion

In table 5.5 results of spectra analysis are summarized, with a classification according to the sample (thermal, sputtered, *in situ* annealed sputtered) and the annealing temperature or UV beam exposure. The first columns display oxidation state percentages, binding energies and peak full width at half maximum (fwhm) from multi-Voigt fit. Oxide stoichiometry is expressed as O:Mo ratios of peak to peak percent concentrations, extracted by CasaXPS analysis of overview spectra. In a similar way, carbon content is described by the percent C:O ratio. The table also provides work functions and valence band positions, with a further distinction between oxygen and defect state VB, as explained in detail below.

Similarly, table 5.6 summarizes results for O:Mo ratio and work function in the case of thermal deposited and sputtered oxide samples on silicon substrate, for every step of their annealing treatment.

Different observations can be made on the data reported in the tables.

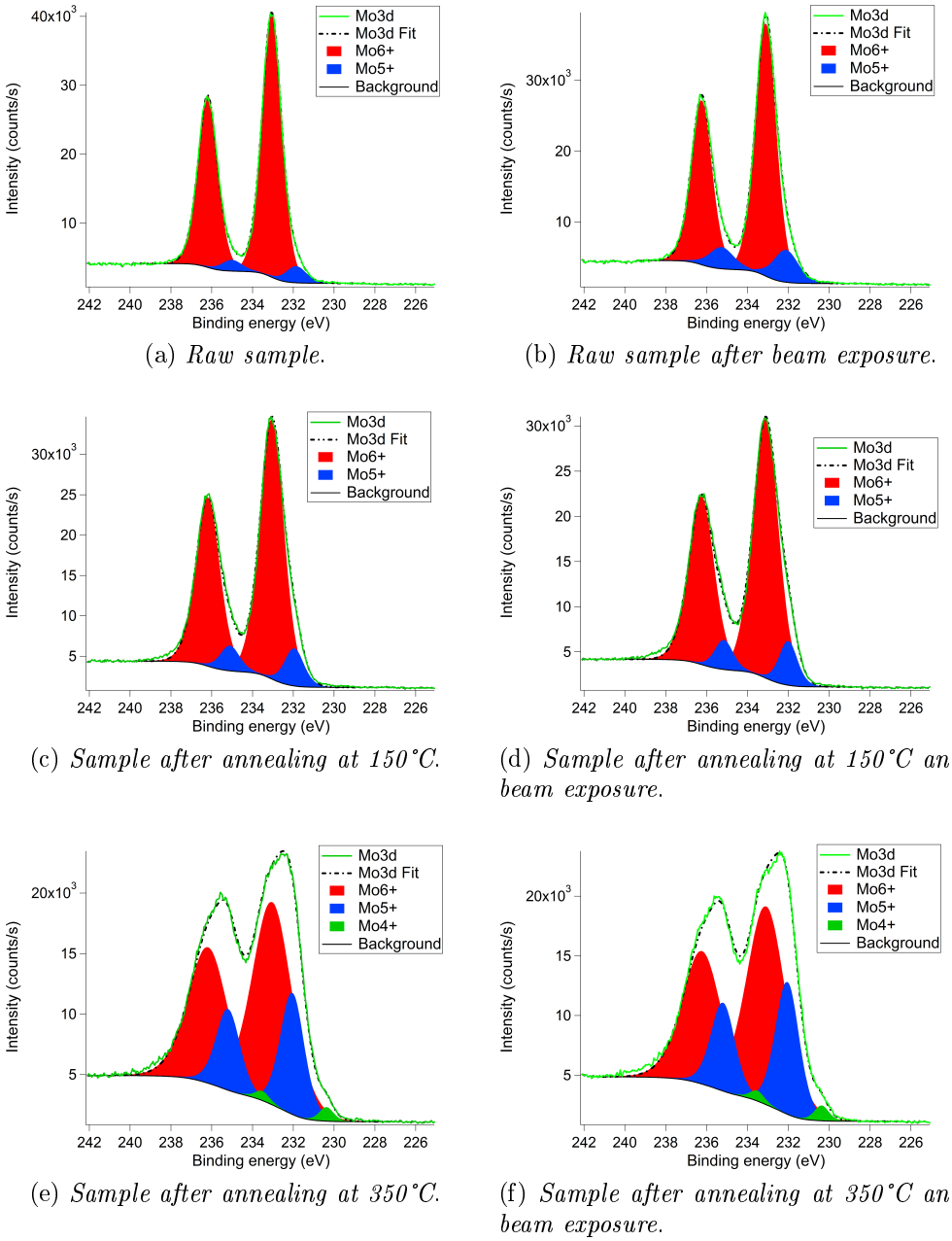


(a) *Raw sample.*

(b) *Raw sample after beam exposure.*

(c) *Sample after annealing at 150°C.*

(d) *Sample after annealing at 150°C and beam exposure.*

(e) *Sample after annealing at 350°C.*

(f) *Sample after annealing at 350°C and beam exposure.*

Figure 5.13: XPS spectra of Mo3d orbitals for thermal deposited $MoO_x$ sample. The series of images follows the evolution of oxidation states according to UV beam exposure (from left to right) and annealing cycle (from top to bottom). Every chart shows experimental Mo3d data, Voigt functions fitting different oxidation states, Shirley background and the envelope resulting wave.

| T (°C) | peak area (%) - Mo3d$_{5/2}$ | | | | B$_E$ (eV) | | fwhm 6+/5+/4+ (eV) | O:Mo | C:O (%) | WF (eV) | VB$_O$ (eV) | VB$_{def}$ (eV) |
|---|---|---|---|---|---|---|---|---|---|---|---|---|
| | Mo$^{6+}$ | | Mo$^{5+}$ | | Mo$^{4+}$ | | | | | | | |
| **Thermal** | | | | | | | | | | | | |
| raw | 94 | 233.1 | 6 | 231.9 | | | 1.12/1.14/– | 2.54 | 64.9 | 4.74 | 2.94 | 0.41 |
| raw + UV | 87 | 233.1 | 13 | 232.1 | | | 1.18/1.38/– | | | | | |
| 150 | 89.6 | 233.1 | 10.4 | 232.0 | | | 1.36/1.09/– | 2.96 | 27.8 | 4.84 | 2.89 | 0.34 |
| 150 + UV | 89.2 | 233.1 | 10.8 | 232.0 | | | 1.45/1.03/– | | | | | |
| 350 | 72.5 | 233.1 | 25.8 | 232.1 | 1.7 | 230.4 | 2.27/1.35/0.80 | 3.42 | 14.6 | 5.50 | 2.95 | 0.14/0.45 |
| 350 + UV | 70 | 233.1 | 28 | 232.1 | 2 | 230.4 | 2.25/1.35/0.80 | | | | | |
| **Sputtered** | | | | | | | | | | | | |
| raw | 100 | 233.1 | | | | | 1.00/1.20/– | 2.53 | 78.9 | 4.32 | 3.09 | 0.57 |
| raw + UV | 97.9 | 233.2 | 2.1 | 231.4 | | | 1.05/1.20/– | | | | | |
| 150 | 99.2 | 233.0 | 0.8 | 231.7 | | | 1.00/1.20/– | 2.60 | 44.5 | 4.92 | 2.82 | 0.39 |
| 150 + UV | 97.5 | 233.1 | 2.5 | 231.7 | | | 1.10/1.20/– | | | | | |
| 350 | 63.9 | 233.1 | 36.1 | 232.2 | | | 1.45/1.40/– | 3.01 | 13.7 | 5.38 | 2.68 | 0.27 |
| 450 | 80.2 | 233.1 | 19.8 | 232.1 | | | 1.45/1.30/– | 2.88 | 6.8 | 6.15 | 2.52 | 0.17 |
| 450 + UV | 81.1 | 233.1 | 18.9 | 232.1 | | | 1.45/1.30/– | | | | | |
| **Sputtered *in situ* annealed** | | | | | | | | | | | | |
| raw | 92.2 | 233.2 | 5.6 | 231.8 | 2.2 | 230.7 | 0.86/1.00/1.11 | 2.34 | 28.0 | 4.74 | 2.94 | 0.32 |
| 200 | 88.3 | 233.3 | 10.3 | 231.8 | 1.4 | 230.4 | 0.94/1.25/1.00 | 2.53 | 14.3 | 5.34 | 2.80 | 0.04 |
| 200 + UV | 88.1 | 233.3 | 9.7 | 231.8 | 2.2 | 230.5 | 0.94/1.20/1.11 | | | | | |

Table 5.5: Experimental results for $MoO_x$ samples deposited on ITO analyzed by XPS and UPS. Percentages and binding energies of oxidation states, full width at half maximum of different oxidation state peaks, O:Mo ratio, carbon contents and work functions are shown for every step of thermal treatment and before and after beam exposure.

| T (°C) | O:Mo ratio | WF (eV) |
|---|---|---|
| Thermal | | |
| raw | 2.62 | 4.41 |
| 210 | 3.13 | 5.36 |
| 500 | 3.46 | 6.11 |
| Sputtered | | |
| raw | 2.55 | 4.40 |
| 210 | 2.85 | 5.11 |
| 500 | 3.23 | 6.23 |

Table 5.6: Experimental results for $MoO_x$ samples deposited on silicon analyzed by XPS and UPS. O:Mo ratios and work functions are shown for every step of thermal treatment.

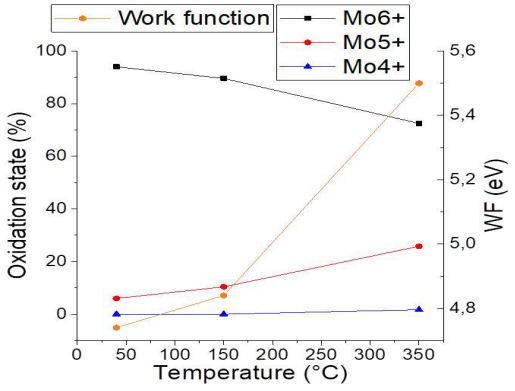


(a) *Thermal deposited $MoO_x$.*

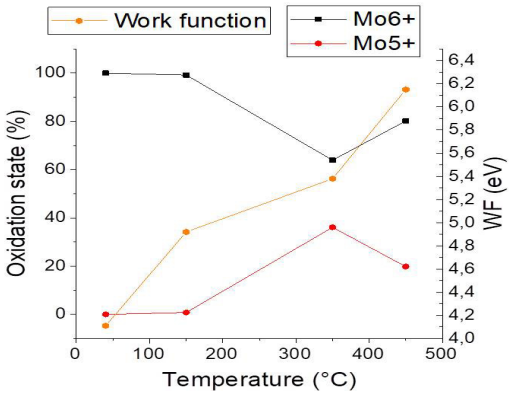


(b) *Sputtered $MoO_x$.*

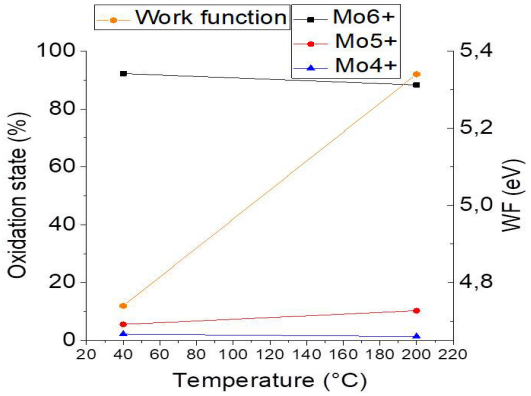


(c) *Sputtered $MoO_x$, in situ annealed at 350°C.*

Figure 5.14: Oxidation state proportions and work function evolution with annealing temperature for the three sample of molybdenum oxide.

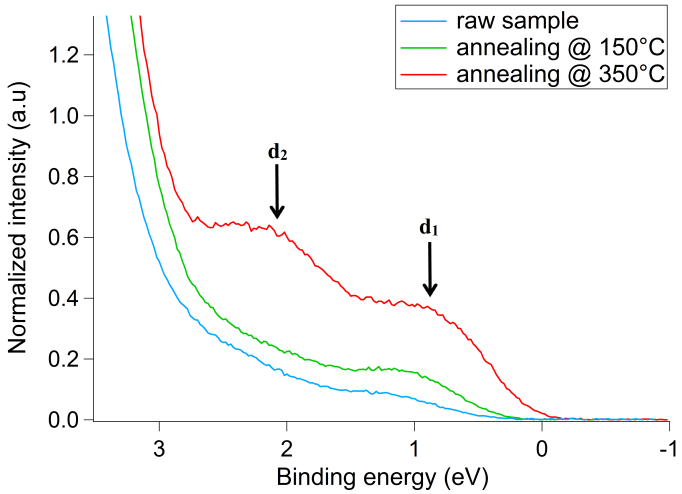


(a) *Thermal deposited $MoO_x$. On the line referred to the sample annealed at 350°C two peaks are visible, indicated as $d_1$, just below Fermi energy, and $d_2$, at an higher binding energy, respectively associated with singly and doubly occupied d-states.*

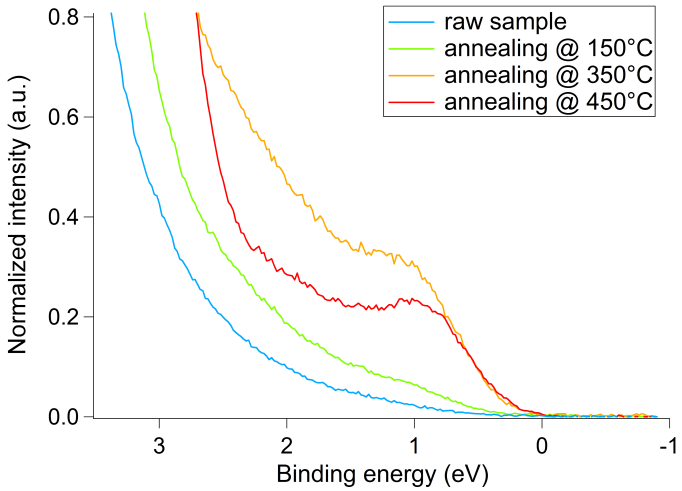


(b) *Sputtered $MoO_x$.*

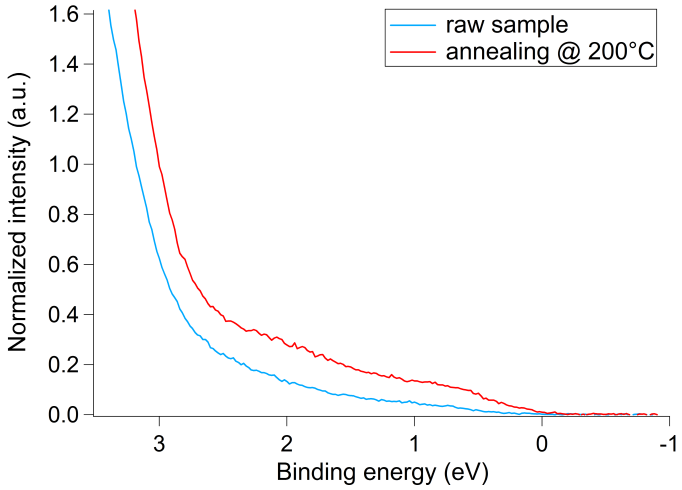


(c) *Sputtered $MoO_x$, in situ annealed at 350°C.*

Figure 5.15: Valence band evolution with annealing temperature: zoom on the structure due to the defect states.

1. For all the samples, thermal treatment results in a decrease of the surface contamination with an almost complete adsorbate removal at 350-450°C, as it is clear from the evolution of carbon peak (figure 5.11) and C:O percent ratio (table 5.5).
   This also results in a rise of oxygen peak intensity at higher temperatures since the O1s photoemitted electrons are no more screened by carbon contaminants, so that this is not incompatible with the growing presence of O-vacancy defect states explained below[6].

2. Peak positions are the same for the three samples and they do not evolve significantly with thermal treatment, within the limits of energy resolution. They are comparable to previously reported results of 232.5 eV for $Mo^{6+}$, 231.6 eV for $Mo^{5+}$ and 229.7 eV for $Mo^{4+}$ for sputtered $MoO_x$ [6].

3. For every sample (except for sputtered oxide annealed at 350°C) the growth of $Mo^{5+}$ percentage confirms compound reduction at every annealing step. In some cases - thermal annealed at 350°C and pre-annealed sputtered - also $Mo^{4+}$ oxidation state is present. These results are summarized in the graphs in figure 5.14.

4. Peaks get broader at higher temperatures, as summarized in fwhm data of table 5.5. This is a challenging result to interpret, since previous research[6] reported an evident decrease of peak width, at least around 500°C, as a consequence of improved crystalline quality.

5. As annealing temperature continues to increase, every sample shows a growing work function (figure 5.14). This seems to be true regardless of the preparation method, because for all the three samples work functions are the same at every annealing step.

6. The evolution of the valence band structure of the different samples with annealing temperature can be seen in figure 5.15, where magnification focuses on the structure closer to Fermi level. According to previous research[2], changes in valence band occupation with annealing temperature at these lower binding energies is due to intra-gap O-vacancy defects, while the most evident VB cutoff main contribution comes from O2p orbitals. Graphs in figure 5.15 and data in table 5.5 show that the increasing presence of defect states creates a band below conduction band bottom and enhances the conductivity of the material with temperature.
   In particular, the position of the so-called $d_1$ defect band, due to single occupancy of Mo4d levels by oxygen vacancy states[2], moves towards lower binding energies just below $E_F$ with annealing temperature together with a simultaneous increase of VB edge peak intensity. Another intra-gap level $d_2$, due to doubly occupied Mo4d, gives rise to a peak around a binding energy of 2 eV. It is clearly visible only for high temperature annealing, especially in the case of thermal deposited $MoO_x$ at 350°C (5.15a), where two defect-linked valence band edges can be located at 0.14 eV ($d_1$) and 0.45 eV ($d_2$). This is in agreement with the presence of $Mo^{4+}$ oxidation state in the latter sample.

7. An analysis of oxide stoichiometry unexpectedly reveals the increase of oxygen proportion as annealing treatment is performed, which is consistent with work function increase but in opposition to the reduction of the material inferred from oxidation states. In fact, data in table 5.5 show that initial substoichiometric oxides ($MoO_x$

with $x<3$) become superoxidized ($x>3$) after 350°C heating. This could be partially linked to the loss of O1s photoelectron screening by carbon contaminant removal at high temperatures, so that the intensity increase of O1s peak (from 45/50% at room temperature to ∼70% at 450°C in percent concentration) is far more evident than the one of Mo3d (Mo concentration changes from 18/19% at room temperature to ∼25% at 450°C in percent concentration).
However, recent studies[25] carried out on molybdenum oxide on silicon demonstrated a direct proportionality between O:Mo ratio and work function. In order to compare them to our results we should take into account the data reported in table 5.6, referred to $MoO_x$ deposited on the same substrate, annealed up to 500°C. They reveal a O:Mo ratio increase from $x \sim 2.6$ to $x \sim 3.2$-3.5 and a WF rise from less than 4.5 eV to more than 6 eV, similarly to $MoO_x$ on ITO measurements (see graphs in figure 5.16).
Whereas experimental conclusions of ref. [25] (figure 5.16c) report that WF and O:Mo ratio grow with annealing up to 200°C and then start to decrease from 200 to 400°C, the similar trend of these two quantities is in agreement with our results and can represent an experimental confirmation to the theoretical model explained in section 2.1 (illustrated in figure 2.1).
At this regard it is important to underline that our annealing treatment was performed in Ultra High Vacuum and it is therefore not totally comparable to the one under oxygen atmosphere in ref. [25].
Figure 5.17 shows our experimental work function data from UPS on different samples (RT and *in situ* annealed sputtered and thermal deposited; on ITO and Si substrate) on the graph based on the relationship between stoichiometry and WF modelled in ref. [2]. The points are scattered over wide ranges of work function and O-deficiency, so that an analytical function fit by eq. 2.9 was not successfully realized. Moreover, our measurements comprehend some superoxidized samples with O-deficiency $x>0$. This is not contemplated in the theoretical model, where it would result in negative arguments in logarithms of eq. 2.9 (section 2.1). However, it is possible to see a general decrease of WF data versus $x$, with a trend roughly comparable to the theoretical one, even if the stoichiometric work function $WF_0$ is different for Greiner's[2] and our samples, so that there is a vertical offset between trends describing the two data sets: this is possibly due to changes in preparation techniques and growth substrates.

8. Sputtered samples prove to be more stable than thermal deposited ones under UV light, while stability increases with annealing temperature. In fact, the percentage of $Mo^{6+}$ oxidation state is generally lower after beam exposure - UV rays help O-vacancy creation resulting in oxide reduction, but the decrease is less important comparing sputtered to thermal samples or annealed to not annealed ones. For example, a 7% drop in $Mo^{6+}$ oxidation state is measured for raw thermal oxide, whereas it is only by 2.1% for sputtered. In the same way, sputtered oxides treated by 450°C annealing and 350°C *in situ* annealing + 200°C heating undergo almost no effect due to UV photons. The only measure out of the trend is a $Mo^{6+}$ decrease of only 0.4% for thermal deposited $MoO_x$ heated at 150°C, whereas it is of 2.5% for 350°C annealed. It is worth underlining that the first annealing step should be carefully interpreted due to the important effect of contaminant desorption on vacuum level position.

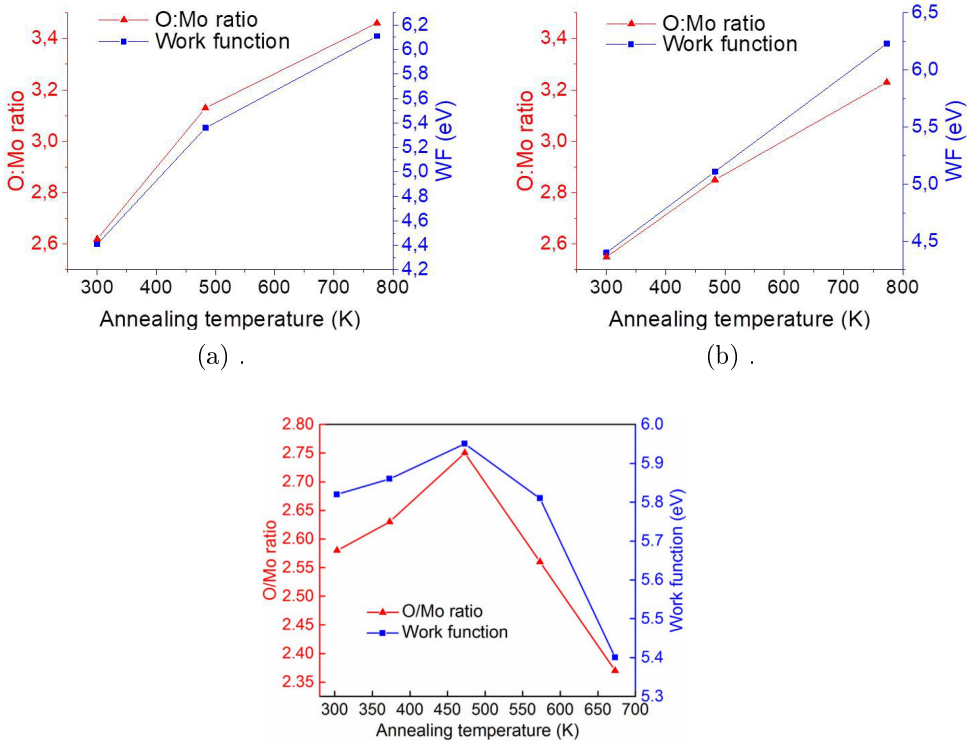


Figure 5.16: Oxidation state proportions and work function evolution with annealing temperature for molybdenum oxide on Si. (a) refers to thermal deposited sample and (b) to sputtered one, both analyzed at LRS in 2016, while (c) concerns comparative experimental data from ref. [25]. The three graphs reveal a similar evolution for O:Mo ratio and work function, even if in (c) a drop is visible after 450 K, whereas a constant increase can be seen in (a) and (b). Temperature scale in Kelvin.

9. Also differences between sputtered oxides according to the annealing method could be inferred, even if the crucial measurement on in-XPS-chamber 350°C annealed sample was afflicted by a machine breakdown which prevented UV effect study. It is possible to notice that *in situ* and in-XPS annealed samples have compatible work functions - respectively 5.34 and 5.38 eV after carbon desorption - but the latter proved to be more reduced (36.1% vs 10.3% of $Mo^{5+}$ state), even if the role of $Mo^{4+}$ should be further understood.

These results agree with the previous knowledge about the reduction of molybdenum oxide by annealing and UV exposure. It is important to point out that, in the perspective of an application in solar cells, the change of $MoO_x$ properties under UV light is not a desirable feature of the material, whereas the annealing-induced evolution is a lab-controllable method which allows to tailor compound characteristics in a predictable way. Therefore, sputtering deposition proves to be more efficient and reliable as a growing technique due to the little influence of UV rays on the produced samples, especially after thermal treatment.

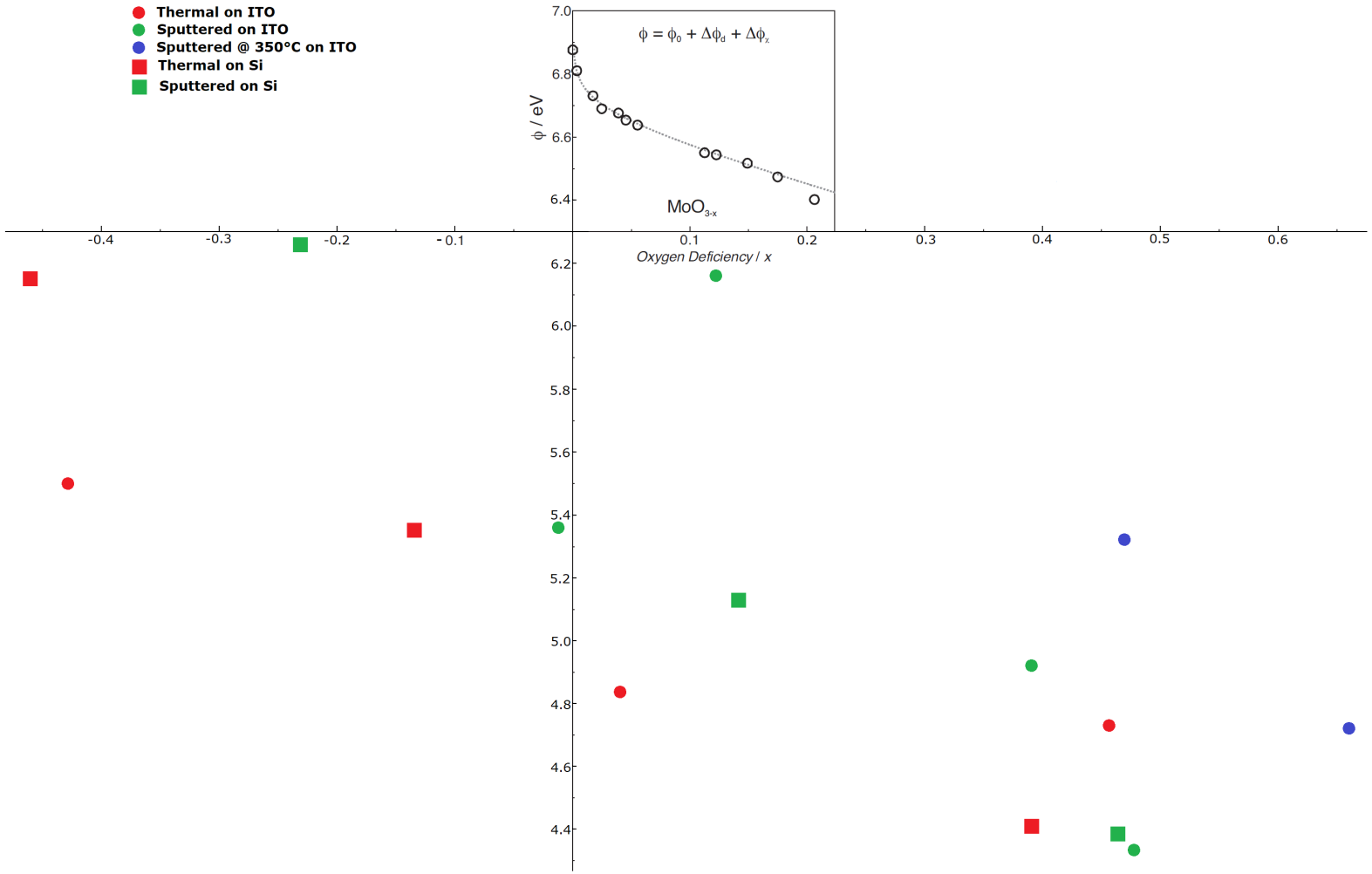


Figure 5.17: Graph of theoretical trend describing the relationship between O-vacancies and work function (dashed line), fitting experimental data (black circles) from Greiner *et al.* (ref. [2]), with extended axes and insertion of our UPS measurements referred to different analyzed samples. Even if it is not possible to fit our data by the equation reported on the chart (eq. (2.9) in section 2.1) due to the high degree of data set dispersion and the presence of negative values of O-deficiency, a qualitative agreement with the logarithmic/linear work function decrease with O:Mo ratio drop can be noticed from the graph. The vertical offset between our and Greiner's measurements is due to different sample characteristics resulting in changes of stoichiometric work function $\Phi_0$.

### 5.1.3 LEEM/XPEEM

#### Protocol

Different samples grown on ITO were analyzed to collect data about their chemical and electronic properties:

1. $MoO_x$ on ITO from sputtering, subsequently treated by annealing at 350°C (thickness ∼30 nm);

2. $MoO_x$ on ITO from thermal deposition, treated by annealing at 350°C (thickness ∼30 nm).

All the samples were previously put in the preparation chamber and heated at T ∼ 130°C in order to free the surface from contaminants.

LEEM images and spectra of every sample were acquired focusing an electron beam on the oxide surface. From the nanometric-resolved reflection drop maps, work function differences on the surface could be examined as well as their evolution during annealing, analyzing specific ROIs or single pixels with different electron absorption properties and calculating cutoff positions on associated spectra. In order to extract quantitative data, relative work function was determined on STV scale by the intersection between the linear fits to the 100% elastically reflected electrons and to the drop-off when $WF_{sample}$ is overcome[26]. Since

$$WF_{sample} = STV + WF_{cath},$$

a measurement of $WF_{cath}$, the cathode work function of the instrument, is needed to obtain absolute $WF_{sample}$ values. According to the calibration procedure described in ref. [28], STV of LEEM drop-off and $WF_{sample}$ from UPS for the same gold on silicon reference sample were compared, to get

$$WF_{cath} = 3.38eV.$$

$MoO_x$ LEEM data could hence be plotted on work function scale by a 3.38 eV translation.

In a similar way, switching from electron gun to synchrotron X-ray beam and setting suitable photon energy and kinetic energy scan interval (STV), different orbitals were investigated by XPEEM: $Mo3d_{3/2}$-$Mo3d_{5/2}$ (with a typical photon energy $h\nu$ of 400 or 650 eV), O1s (with $h\nu = 650$ eV), valence band and secondary electron cutoff (typically with $h\nu = 100$ eV).

The technique provided a contextual recording of surface map where the electron emission for every point could be visualized, with an estimated resolution of ∼100 nm. The images were then analyzed tracing different ROIs and studying emission spectra for selected zones and the procedure was repeated for every sample before and after annealing steps and with different oxygen contents in the chamber. Both for valence band and secondary spectra, cutoff positions could be located by the intersection between a linear fit on the slope and the horizontal tangent to the background, in a similar way to UPS analysis.

#### Results

LEEM examples relative to sputtered 30 nm thick $MoO_x$ are shown in figure 5.18. Whereas reflection drop-off is stable and work function homogeneous on the same surface,

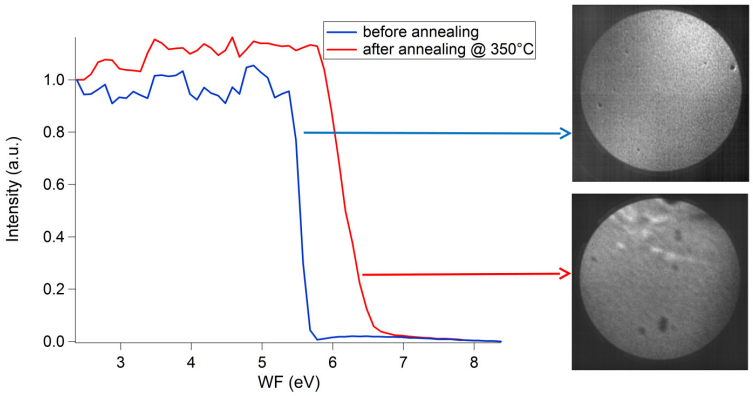


Figure 5.18: Normalized LEEM spectra on the calibrated WF scale referring to the whole sample surface before and after annealing for sputtered $MoO_x$, with the corresponding surface maps. STV = 2 and 2.4 eV respectively, corresponding to an energy straight after the drop-off start; FOV = 20 $\mu$m. The small black and white features appearing after annealing are probably due to surface physical defects as scratches.

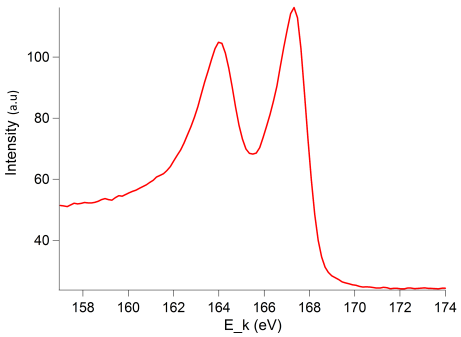


(a)

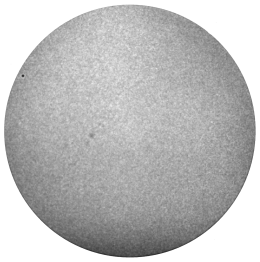

(b)

Figure 5.19: Mo3d peaks for thermal deposited $MoO_x$ heated at ~130°C, at a photon energy of 400 eV (a) and XPEEM map obtained by summing the images acquired at every STV step (b, FOV = 10 $\mu$m).

spectra registered for an overall ROI before and after 350°C annealing can be compared. It is apparent that at high temperature LEEM cutoff moves in the direction of higher kinetic energies, and a difference of ~0.5 eV in the position of the signal drop appears. Calibration procedure allowed to obtain quantitative data for work functions:

- 5.41 and 5.86 eV for sputtered sample before and after 350°C annealing,
- 4.70 and 5.67 eV before and after the same treatment on thermal deposited $MoO_x$.

As for XPEEM maps, since all the analyzed $MoO_x$ samples were uniform and no displacement in peak positions on different regions was measured, only ROIs extended over the whole surface were examined. As an example, an homogeneous XPEEM map and corresponding Mo3d peaks (split by spin-orbit coupling) extracted by analysis of an overall ROI are shown in figure 5.19.

Also secondary electron cutoffs are homogeneous on every analyzed sample, even after the high temperature heating, and no regions with different characteristics in the colour map were detected. However, it proved impossible to extract quantitative data because of problems to determine a well-established calibration method for the instrument and a lack of photon energy reproducibility. Further measurements to solve some of these issues are therefore needed, but the synchrotron facility was not accessible after the data elaboration which revealed them.

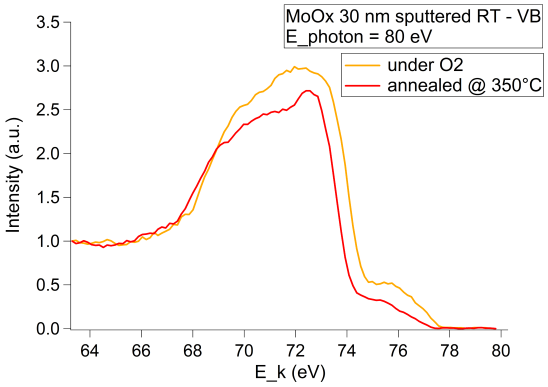


Figure 5.20: Sputtered $MoO_x$ sample valence band comparison before and after the annealing treatment at 350°C. Spectra are normalized at 1 and 0 at respective ends.

The chart in figure 5.20 compares sputtered $MoO_x$ valence bands at room temperature and after the annealing cycle. It is important to point out that before thermal treatment the sample was held under an oxygen-rich atmosphere ($P_{O_2} \sim 2{\times}10^{-8}$ Torr).

Focusing on the right shoulders accounting for defect states, a decrease of their intensity after annealing (without $O_2$) is evident. The main cutoff displaced towards lower kinetic energies in the post-treatment measurement (by 0.5 eV in this example).

### Discussion

Data collected from synchrotron techniques on molybdenum oxide allow to draw some main conclusions:

1. From the whole set of studies on $MoO_x$ (LEEM, Mo3d and secondary cutoff) at every heating treatment stage, it appears that no crystallites or regions with different chemical and electrical properties are present on the surface and samples do not change during annealing cycle. Oxidation degree and work function are therefore homogeneous throughout the material.

2. $MoO_x$ valence band evolves with thermal treatment, but in a direction which is opposite to the expectations[5][6]. In fact, the samples oxidize instead of being reduced (figure 5.20), as can be seen from the disappearance of the defect states in the extreme part of the valence band[2] and VB edge displacement towards lower kinetic energies (i.e. higher binding energies). Since the samples were kept under oxygen during most of the measurements, high annealing temperature enhances oxidation effectiveness with the consequential filling of O-vacancy defect states and decrease of their contribution to conduction. This could be true also for the analyses performed without oxygen (as in the case of annealed sample in figure 5.20), since gas molecules can remain and react on the oxide surface also after the $O_2$ flux removal.

3. Work function differences emerge before and after annealing and they are compatible with UPS measurements (for example 0.45 eV in sputtered $MoO_x$ from LEEM and 0.46 eV from UPS, comparing 100-150°C and 350°C heated samples). They indicate an evolution of oxide properties due to thermal treatment.

## 5.1.4 Conclusion on $MoO_x$

The ensemble of experimental techniques used to characterize $MoO_x$ samples reveals an important difference between compounds according to their growth substrate.

Whereas, during annealing on silicon, grain structures and corresponding surface potential contrast (KPFM) develop on the surface, ITO-deposited $MoO_x$ proves to have a greater thermal stability in topography and potential measurements. This is confirmed by XPEEM, which did not reveal any crystallites with different emission properties, and by LEEM, which gave access to quantitative work function data for different surface sites. XPS and UPS results are compatible with the LEEM ones and highlight work function increase, reduction of oxidation degree and defect state rise during annealing, in line with previous research[5][6].

It is however important to discuss in more detail Photoemission Spectroscopy results, since the demonstration of oxide reduction appears to be incompatible with work function and oxygen proportion rise. In fact, as proposed by Greiner's model[2], WF should decrease with O-deficiency for electronegativity and donor concentration considerations, with an initial steep logarithmic drop for nearly stoichiometric compounds and a following linear trend. Experimental data presented in ref. [25] and visible in figure 5.16c can be regarded as a proof of this fact, even if only in the linear regime, since the logarithmic one is probably verified for tiny degrees of non-stoichiometry[2]. Even if it was not possible to analytically verify the agreement between our results and model equation (2.9) due to a great statistical dispersion in a limited quantity of measurements - just three or four for every sample, graphs in figures 5.16a and 5.16b confirm the direct proportionality between O:Mo ratio and molybdenum oxide work function.

At the same time, the simultaneous verification of oxidation state decrease and filling of intra-gap states due to O-vacancies can be compatible with WF and O:Mo growth if we take into consideration High-Resolution TEM and LEEM data of previous studies illustrated in section 2.2[6]. In fact, together with the elimination of carbon contamination and its screening effect on O1s photoelectron so that oxygen presence is more easily revealed by XPS at higher temperatures, a possible explanatory hypothesis is that reorganization of oxide structure takes place during annealing. This is supposed to result in a nearly stoichiometric (and eventually superoxidized $MoO_x$ with $x>3$) substrate with high degree of crystallinity and elevated work function and an ensemble of substoichiometric surface grains with a range of work functions, lower than $MoO_3$ according to the theory. Therefore, it is not inconsistent with expectations that XPS and UPS reveal the increase of Mo ions with reduced oxidation degree ($Mo^{5+}$ and $Mo^{4+}$) and the appearance of a defect band near the bottom of CB - depending on surface layer - together with an overall rise of O:Mo ratio and WF - a global property depending mainly on the bulk substrate. In fact, Photoemission measurements were performed by means of Ultraviolet photons of 21.22 eV and 1486.70 eV X-ray light, with respective probing depths - layer thicknesses providing 95% of the overall signal - of around 15 and 75 Å[29]. This means that both surface amorphous and bulk crystalline phase could be analyzed, since substoichiometric grains involve the first 40 Å according to ref. [6], but they are not homogeneous on the whole sample and do not completely cover it.

If this interpretation is correct, it is expected to distinguish on LEEM maps different regions with higher and lower work functions, in agreement with results of previous research (as shown, for example, in figure 2.2). The fact that, on the contrary, Low Energy Electron Microscopy performed at SOLEIL did not reveal any relevant grain structure could be however due to a poor instrumental resolution (around a hundred of nanometers, comparable to the extension of expected domains with different WF[5][6]). Another element which seems to be in disagreement with this explanation is the increase of peak broadening (fwhm) with annealing temperature, a proof of deteriorated structural

order in the layer, even it is not incompatible with a high-quality crystalline substrate covered with amorphous-like surface grains.

The techniques also investigated UV effects on the oxide and demonstrated the beam-caused reduction - photon energy triggers the creation of oxygen vacancies - and a greater influence on thermal deposited samples rather than on sputtered ones. Moreover, the role played by the annealing method emerges from XPS/UPS data, suggesting a greater reduction when the heating is rapid and not gradual and slow as in the *in situ* procedure, even if stoichiometry differences should be carefully examined by further research. As demonstrated, electrical property evolution with heating depends on the substrate (Si vs ITO) and this points out the importance of performing characterization for materials engineering directly on the same compound supposed to be employed in real devices, because of the great impact of deposition layer on $MoO_x$ crystalline reconstruction during annealing.

Finally, the improved stability of sputtered molybdenum oxide under UV beam exposure provides an important indication in order to develop more efficient and reliable photovoltaic cells.

## 5.2 Titanium oxide

### 5.2.1 AFM

#### Protocol

In order to understand the surface structure of $TiO_2$ samples for a comparison with molybdenum oxide, simple AFM measurements were performed at the University of Southern Denmark by Dr. Ahmadpour and analyzed at INSP. Sputtered $TiO_2$ on ITO samples previously analyzed at SOLEIL synchrotron facility were studied: 215°C and 360°C annealed inside the beamline preparation chamber and high temperature deposited at 355°C, as explained below in section 5.2.3.

Grain dimensions were extracted with the same method explained in section 5.1.1, while for roughness the difference between the minimum and the average surface height calculated by Gwyddion analysis software was considered.

#### Results

The topographical maps are visible in figure 5.21. The three samples feature a similar morphology and no surface evolution with the annealing stages is evidenced. Grain shape resembles the one of $MoO_x$/ITO samples, as can be seen from a comparison between figures 5.8d and 5.21, for instance.

#### Discussion

By a quantitative analysis of AFM images, the results shown in table 5.7 were obtained. The three samples have similar grain size and roughness parameters and no effect of thermal treatment can be proved. Since also $MoO_x$ deposited on ITO appears not to be influenced by annealing, it is probable that the substrate plays an important role in determining oxide behavior. Also in this case, as already pointed out for molybdenum oxide, it is visible that grain morphology closely resembles the ITO underlayer as shown in ref. [26].

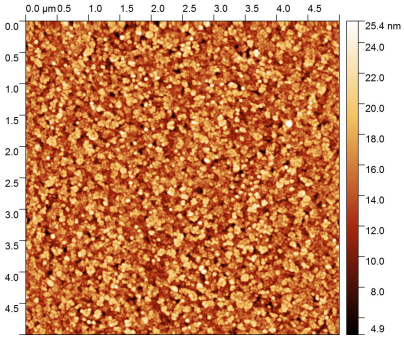


(a) *Morphology map of 215°C annealed sputtered sample ($1^{st}$ step); color scale from 4.9 nm (black) to 25.4 nm (white).*

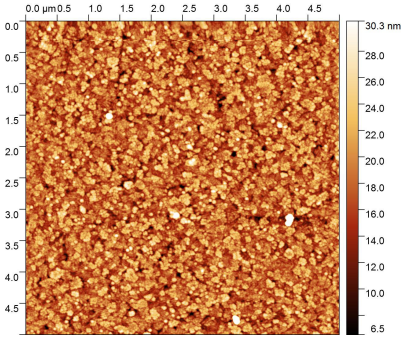


(b) *Morphology map of 360°C annealed sputtered sample ($2^{nd}$ step); color scale from 6.5 nm (black) to 30.3 nm (white).*

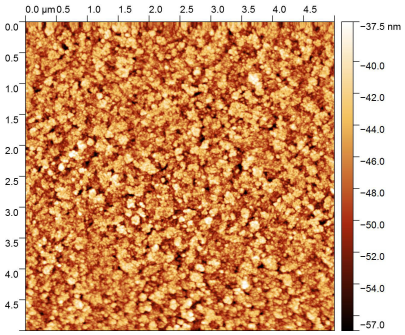


(c) *Morphology map of 355°C sputtered sample; color scale from -57.0 nm (black) to -37.5 nm (white).*

Figure 5.21: 5 $\mu$m×5 $\mu$m AFM images of $TiO_2$ on ITO.

| $TiO_2$/ITO (analyzed by XPEEM) | 42 nm @ 215°C | 42 nm @ 360°C | 45 nm *in situ* @ 355°C |
|---|---|---|---|
| Grain diameter (nm) | 38±9 | 25±8 | 25±5 |
| Aggregate diameter (nm) | 97±17 | 76±11 | 110±30 |
| Roughness (nm) | ∼14 | ∼17 | ∼17 |

Table 5.7: Morphological parameters measured by AFM on $TiO_2$/ITO.

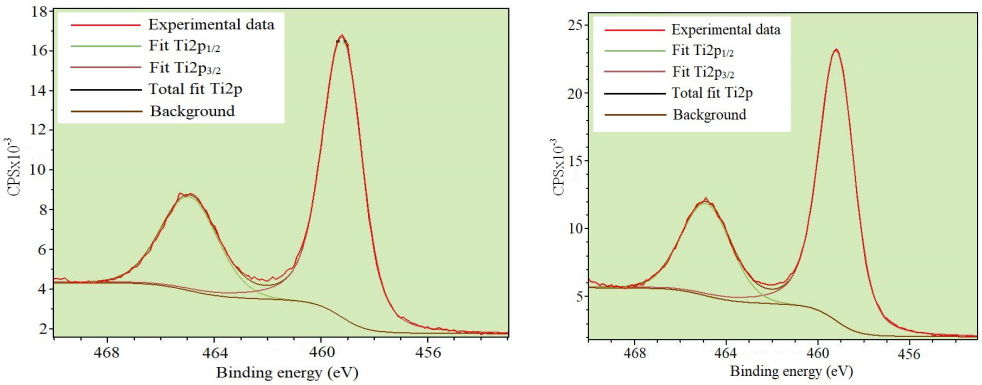


(a) *Raw sample of titanium oxide.*

(b) *Sample of titanium oxide after annealing at 250°C in the XPS vacuum chamber.*

Figure 5.22: Peaks of Ti2p for $TiO_2$ sample sputtered at 355°C, in particular $Ti2p_{1/2}$ at higher and $Ti2p_{3/2}$ at lower binding energies, respectively. Intensity is expressed in counts per second.

### 5.2.2 XPS/UPS

#### Protocol

XPS and UPS measurements were performed at LRS with the same method explained in section 5.1.2 for $MoO_x$. Analyzed samples contemplated $TiO_2$ sputtered both at room temperature and at 355°C, whereas inside XPS vacuum chamber a soft annealing at 250°C was performed to eliminate surface contamination.

XPS overview, Ti2p and O1s spectra were acquired, as well as UPS valence band and secondary electron cutoff scans.

#### Results

In figure 5.22 examples of Ti2p peaks are visible in the case of 355°C deposited oxide before and after annealing at 250°C. Peak positions were identified at 530.6 eV for O1s, 465.0 eV for $Ti2p_{1/2}$ and 459.3 eV for $Ti2p_{3/2}$, which did not change after 250°C treatment. Similar spectra and binding energies were obtained for the same oxide sputtered at room temperature, as summarized in table 5.8 together with work function, valence band edge energy and O:Ti ratio of the analyzed samples.

#### Discussion

Photoemission Spectroscopy data, as reported in table 5.8, reveal a slight increase of 0.3-0.4 eV in work function after heating at 250°C, probably due to desorption of surface contaminants. At the same time, no role seems to be played by preparation procedure, since $TiO_2$ samples sputtered both at room and at elevated temperature show the same work function, valence band position and WF evolution with heating. Also oxygen and titanium binding energies remain unchanged within XPS resolution before and after soft annealing and regardless of the deposition method.

As for oxide stoichiometry, it could be regarded as stable around an O:Ti ratio of 2.5 for different synthesis techniques and heating temperatures, even if it can be argued

| Sample | T (°C) | WF (eV) | VB (eV) | O1s (eV) | Ti2p$_{1/2}$ (eV) | Ti2p$_{3/2}$ (eV) | O:Ti |
|---|---|---|---|---|---|---|---|
| Sputt. RT | raw | 3.8 | | 530.7 | 464.8 | 459.1 | 2.55 |
| | 250 | 4.2 | 3.5 | 530.5 | 464.7 | 459.0 | 2.3 |
| Sputt. 355°C | raw | 3.9 | | 530.6 | 465.0 | 459.3 | 2.5 |
| | 250 | 4.2 | 3.2 | 530.6 | 465.0 | 459.3 | 2.5 |

Table 5.8: Experimental results for $TiO_2$ samples analyzed by XPS/UPS. Work functions, valence band positions, oxygen and titanium peak binding energies and O:Ti ratio are shown before and after the soft annealing treatment.

that for sputtering at room temperature reduction takes place after 250°C treatment (O:Ti ratio drops to 2.3). This is a possible hint of a better chemical stability of the material when prepared under heating (at 355°C), but the oxygen proportion change is slight and it could be related to contaminant desorption - also water molecules and other O-compounds are present on the surface before soft annealing.

A different experimental technique is therefore needed to get a deeper comprehension of chemical and electrical properties of the material: in this context Raman, Infrared or X-ray Absorption Spectroscopy measurements can be helpful since they allow to recognize crystalline phase in titanium oxides like anatase and rutile.

### 5.2.3 LEEM/XPEEM/XAS

#### Protocol

The ∼45 nm thick titanium oxide samples on ITO analyzed by synchrotron techniques are listed below:

1. sputtered $TiO_2$ treated by one-step annealing at 360°C;
2. sputtered $TiO_2$ treated by two-step annealing at 215°C and 360°C;
3. sputtered $TiO_2$ deposited at 355°C.

In a similar way to $MoO_x$, they underwent heating at T ∼ 130°C to free the surface from contaminants. A constant amount of oxygen in the chamber was needed in order to preserve $TiO_2$ stoichiometry and avoid substantial changes in oxidation state of the material. An $O_2$ pressure between $1\times10^{-8}$ and $3\times10^{-8}$ Torr was therefore maintained even during heating.

LEEM technique was employed to investigate the samples and their evolution with annealing stages and extraction of work functions was carried out as for $MoO_x$ (section 5.1.3).

With regard to XPEEM, in addition to O1s orbital, valence band and secondary cutoff, Ti2p$_{1/2}$-Ti2p$_{3/2}$ peaks were investigated using a typical photon energy of 650 eV. Image treatment and spectra analysis were the same as the aforementioned $MoO_x$ ones (section 5.1.3).

However, the most important data for $TiO_2$ were collected by XAS technique, scanning a photon energy interval with a fixed STV (typically 1.4, 1.6 or 1.8 eV). In this case normalization - spectrum division by the current on a filter in front of the beam - was necessary to remove any effect of undulator peaks during the photon energy scan.

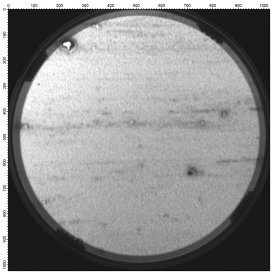

(a) *LEEM image of $TiO_2$ at room temperature (FOV = 20 $\mu m$, STV = 0.45 eV).*

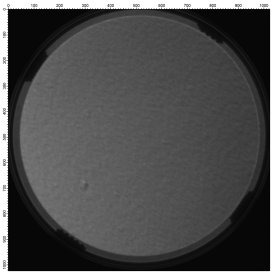

(b) *LEEM image of $TiO_2$, two-step annealed at 215 and 360°C (FOV = 10 $\mu m$; STV = 1.7 eV).*

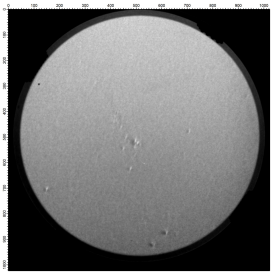

(c) *LEEM image of $TiO_2$ deposited at 355°C (FOV = 20 $\mu m$; STV = -0.3 eV).*

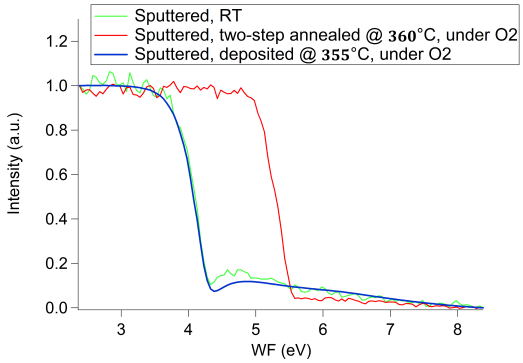


(d) *Normalized LEEM spectra. Comparison of background random pixels from 5.23a and 5.23b and overall ROI from 5.23c.*

Figure 5.23: LEEM images and spectra relative to the sputtered $TiO_2$ samples ((a) before and (b) after two-step annealing and (c) high temperature deposited).

Secondary electron emission maps were recorded in XAS analysis and various ROIs were traced on them, so that their associated spectra allowed to compare areas with different characteristics on the surface.

### Results

In figure 5.23 an example of LEEM can be seen. At ambient temperature (fig. 5.23a) the sample appears homogeneous except for minor features (probably structural defects or scratches). After 360°C annealing a fine texture is visible on the surface, but no distinct regions are found (fig. 5.23b). It was therefore decided to analyze a random background pixel of both maps (excluding defects). Figure 5.23c shows the surface map of high temperature deposited $TiO_2$: the same surface homogeneity with minor defects can be noticed so that an overall ROI was selected for the analysis. From a comparison of the three spectra (fig. 5.23d) a change in work function of ∼1.2 eV after two-step annealing at 360°C could be quantified - WF passes from 3.84 to 5.02 eV, even if special attention should be paid to the fact that images 5.23a and 5.23b were acquired at different fields of view, which proved to affect results in previous measurements. On the other hand, 355°C-deposited oxide revealed the same WF as the room temperature one, i.e. 3.8 eV.

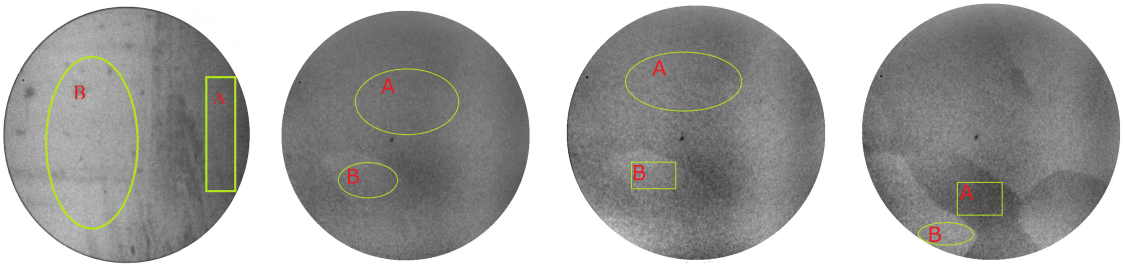


(a) *Sputtered $TiO_2$ at room temperature. $E_{photon}$=480eV, FOV=20μm, STV=3.4eV.*

(b) *Sputtered $TiO_2$ sample two-step annealed at 360°C. $E_{photon}$=459.14eV, FOV=20μm, STV=1.8eV.*

(c) *Sputtered $TiO_2$ sample two-step annealed at 360°C. $E_{photon}$=460.87eV, FOV=20μm, STV=1.8eV.*

(d) *Sputtered $TiO_2$ sample two-step annealed at 360°C. $E_{photon}$=461.68eV, FOV=20μm, STV=1.8eV.*

Figure 5.24: XPEEM maps (a) before and (b)(c)(d) after two-step annealing of $TiO_2$ samples, registered during secondary cutoff scan, with the indication of analyzed ROIs. (b), (c) and (d) were acquired with different photon energies.

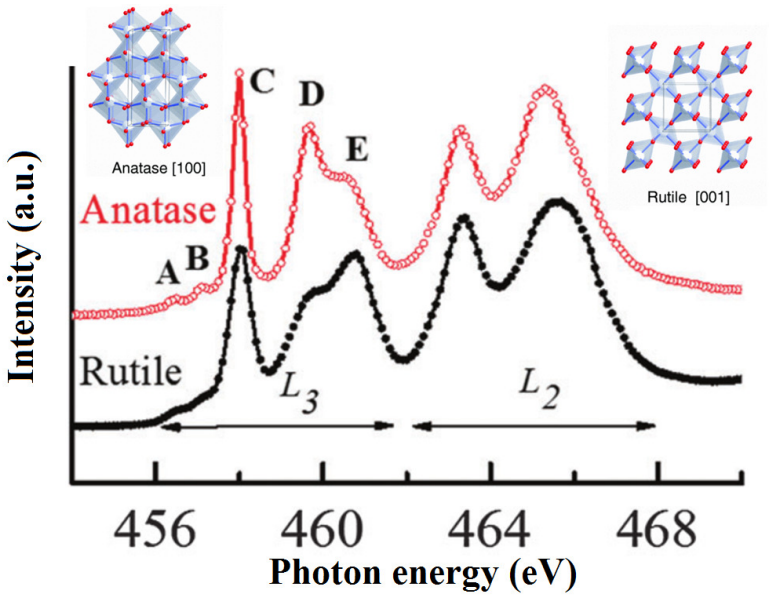


Figure 5.25: $TiO_2$ anatase and rutile absorption spectra with the details of crystalline structure of the two phases. Spin-orbit coupling accounts for the splitting between $Ti2p_{3/2}$-Ti3d and $Ti2p_{1/2}$-Ti3d transition peaks (respectively $L_3$ and $L_2$ regions). $L_3$ is further split into C and D/E sub-peaks for crystal-field interaction, whereas other symmetry reasons divide D and E features - with reversed height relationships between them for rutile and anatase. A and B pre-edge peaks are due to core-hole interaction and typical of anatase phase. Illustration from [3].

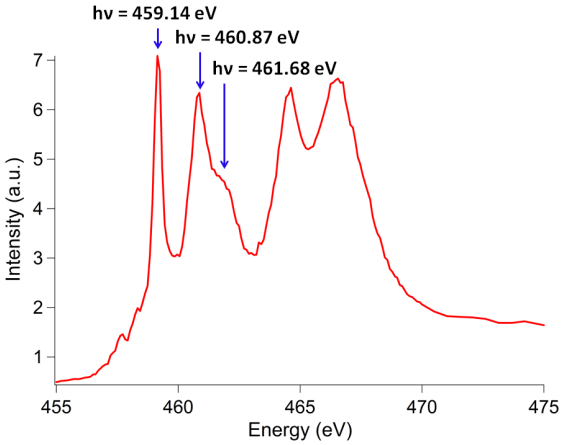


Figure 5.26: The graph shows an example of $TiO_2$ XAS spectrum, referred to two-step annealed sample (ROI A in figure 5.29d), with the indication of the energies of the main peaks. Photons of the same $h\nu$ were used for secondary cutoff measurements.

The images and graphs provided in figure 5.24 shows the sample evolution during annealing according to XPEEM in secondary cutoff energy range. Before thermal treatment the surface appears homogeneous (different colours of the ROIs in figure 5.24a are probably due to contamination or surface defects, but their spectra proved to be similar), whereas separate domains of polycrystallites are visible after heating. In particular, they become evident using the photon energy of 461.68 eV, corresponding to the second $e_g$ $Ti2p_{3/2}$ peak in the XAS spectrum (see figures 5.25 and 5.26), as explained below.

Figure 5.27 illustrates the valence band evolution in one-step and two-step annealed $TiO_2$ samples. Only a slight displacement towards higher kinetic energies $E_K$ is visible for the main cutoff in figure 5.27a, whereas it proves to be stable in 5.27b. On the other hand, an important change appears for defect state band, which moves to lower $E_K$ and whose intensity decreases until it almost disappears with growing annealing temperature and oxygen pressure.

Figure 5.26 provides an example of $TiO_2$ XAS spectrum, that can be compared to literature data as anatase and rutile phase absorption peaks in figure 5.25 - proving to highly resemble anatase ones. Two couples of peaks are visible at lower and higher energies (∼459-463 eV and ∼463-469 eV), accounting for electronic transitions between $Ti2p_{3/2}$ and Ti3d and between $Ti2p_{1/2}$ and Ti3d, respectively. Keeping the focus on $Ti2p_{3/2}$, a pre-edge double feature at ∼458 eV can be noticed on its left: this is typical of $TiO_2$ anatase phase, originating from poorly-screened-3d/2p-core-hole interaction and specific crystal symmetry[3]. Splitting of $Ti2p_{3/2}$ into two sub-peaks at 459.14 and around 461 eV is due to crystal-field interaction, which divides Ti3d into $t_{2g}$ and $e_g$ sub-bands with different symmetries[4]. The latter determines two further features at 460.87 and 461.68 eV for symmetry reasons, because $e_g$ orbitals point towards O2p in the oxide structure. These sub-peaks provide information about long, medium and short range crystalline order[4].

Figures 5.28, 5.29 and 5.30 show absorption surface map and XAS spectra of one-step, two-step annealed and high temperature deposited $TiO_2$. Whereas for the latter and before annealing the surface appeared homogeneous, the thermal treatment performed inside the beamline preparation chamber resulted in the formation of different domains, that were separately analyzed in single ROIs. In the graphs 5.28c and 5.29c, spectra of not annealed and 215°C annealed samples exhibit four peaks (two couples referred to $Ti2p_{3/2}$ and $Ti2p_{1/2}$, respectively), but for all post-annealed oxides - both on the beamline at 360°C and during deposition at 355°C - typical anatase features appear (pre-edge and further splitting, as aforementioned). This is visible in figures 5.28c, 5.29f and 5.30b.

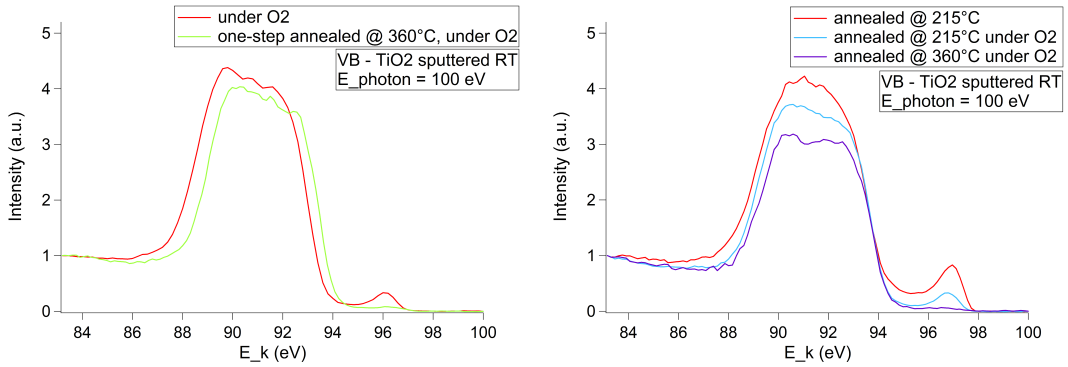


(a) *One-step annealed sputtered $TiO_2$ sample.*

(b) *Two-step annealed sputtered $TiO_2$ sample.*

Figure 5.27: Sputtered $TiO_2$ sample valence band comparison before and after the annealing treatment. The spectra are normalized at 1 and 0 at both ends.

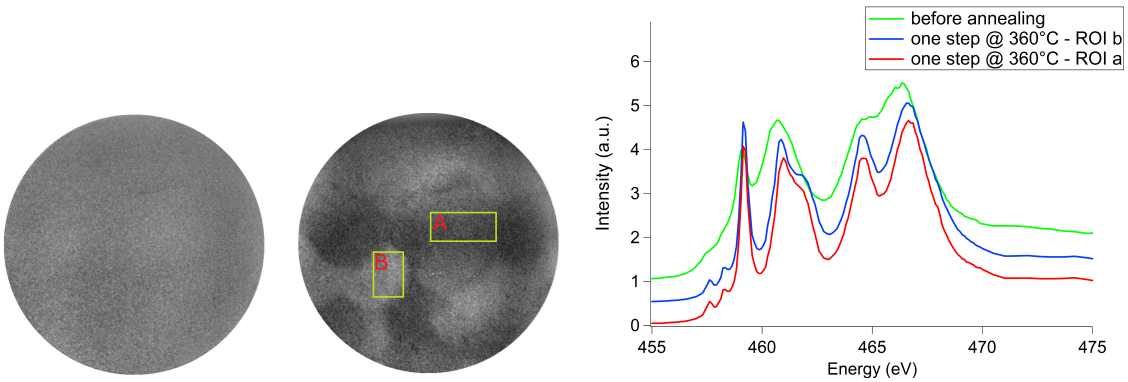


(a) *Sputtered $TiO_2$ sample at room temperature ($E_{photon}$=461.78eV, FOV=20µm, STV=1.6eV). An overall ROI was analyzed.*

(b) *Sputtered $TiO_2$ sample one-step annealed at 360°C, with the indication of the analyzed ROIs ($E_{photon}$=461.78eV, FOV=20µm, STV=1.8eV).*

(c) *Sputtered $TiO_2$ XAS spectra of the highlighted ROIs in the previous images. Graphs are vertically translated.*

Figure 5.28: XAS surface images and spectra of $TiO_2$ following the evolution before and after one-step annealing.

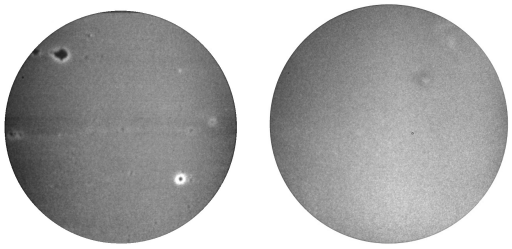

(a) *Sputtered $TiO_2$ sample at room temperature ($E_{photon}$=461.78eV, FOV=20$\mu$m).*



(b) *Sputtered $TiO_2$ sample annealed at 215°C ($E_{photon}$=461.78eV, FOV=20$\mu$m).*

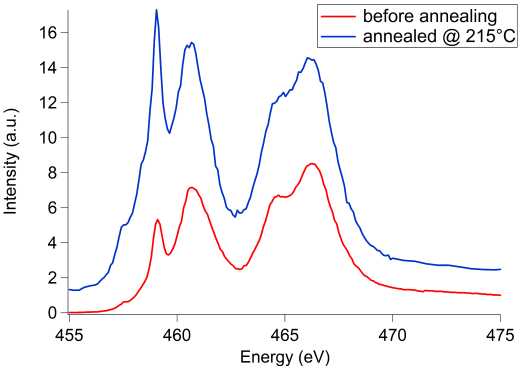


(c) *Sputtered $TiO_2$ XAS spectra of overall ROIs of 5.29a and 5.29b. Graphs are vertically translated.*

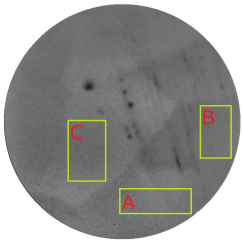


(d) *Sputtered $TiO_2$ sample two-step annealed at 360°C, with the indication of the analyzed ROIs ($E_{photon}$=461.78eV, FOV=20$\mu$m).*

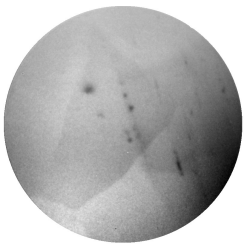

(e) *Sputtered $TiO_2$ sample two-step annealed at 360°C (FOV=20$\mu$m). By changing the photon energy to $E_{photon}$=460.36eV contrast inversion appears with respect to 5.29d.*

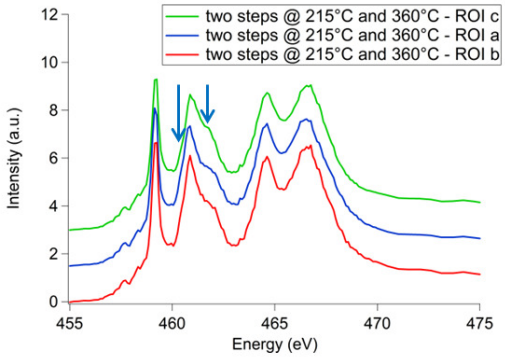


(f) *Sputtered $TiO_2$ XAS spectra of the highlighted ROIs in figure 5.29d, with labels of 460.36 and 461.78 eV photon energies used to acquire 5.29d and 5.29e. Graphs are vertically translated.*

Figure 5.29: XAS surface images and spectra of $TiO_2$ following the evolution during two-step annealing. Images were acquired at STV = 1.4 eV.

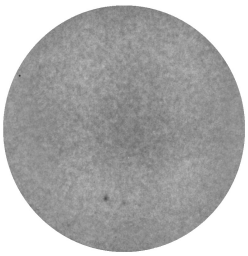

(a) *355°C sputtered $TiO_2$ ($E_{photon}$=461.78eV, FOV=20μm, STV=1.6eV). An overall ROI was analyzed.*

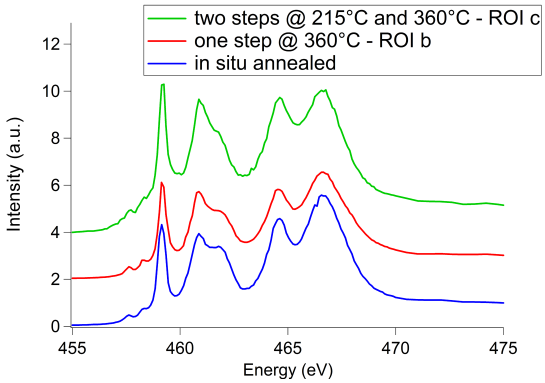


(b) *Comparison between XAS spectra of the three $TiO_2$ samples. An overview region considered for in situ annealed sample in figure 5.30a, whereas dark ROIs for two-step and one-step annealed ones, respectively ROI A shown in figure 5.29d and B in 5.28b. Graphs are vertically translated.*

Figure 5.30: XAS surface image of *in situ* annealed $TiO_2$ and spectra comparison between the three annealed samples.

Moreover, figures 5.29d and 5.29e provide an instance of contrast inversion: changing the photon energy by around 1 eV, surface regions of higher electron emission become darker and vice-versa.

### Discussion

Valence band analysis reveals sample oxidation during annealing performed in $O_2$-rich atmosphere, whereas LEEM spectra highlight a work function increase of the order of 1 eV after annealing, but no changes for high temperature deposited oxide.

Unlike molybdenum oxide, on $TiO_2$ samples crystalline domains appear after 360°C heating, except for the case of 355°C deposition. These regions are well-distinguishable on the frames acquired at photon energies corresponding to XAS $Ti2p_{3/2}$ peaks, especially with $h\nu = 461.68$ eV (figure 5.24), which suggests that surface differences lay on structural order and crystalline interactions these sub-peaks are related to.

Secondary electron XPEEM and XAS (figures 5.24, 5.28 and 5.29) agree that main differences between surface domains arise around $Ti2p_{3/2}$-$e_g$ peak; another element supporting this interpretation is the contrast inversion observed when scanning different energies on the same $Ti2p_{3/2}$ sub-peak (figure 5.29).

Secondary cutoff calculations for selected ROIs in figure 5.24 do not reveal any work function difference between domains. This fact suggests that inhomogeneity in emission intensity is probably due to changes in molecular symmetries between crystallites which give rise to different electronic densities at structures corresponding to $e_g$ sub-peaks.

Further research is therefore useful to deepening a comparative analysis of crystalline structures developed during annealing and elevated temperature deposition.

Analyzing in further details XAS spectra, it is possible to understand the evolution of the oxide structure: starting from amorphous $TiO_2$ at room temperature, at 215°C minor pre-edge features and the increase of $t_{2g}/e_g$ intensity ratio begin to appear (5.29c), until full anatase characteristics are visible in 360°C annealed and 355°C deposited samples.

An exam of right $e_g$ sub-peak shape in graph 5.30b (blue line referred to *in situ* annealed $TiO_2$) and XPEEM image comparison suggest a more complete anatase re-

construction and a more homogeneous surface structure (lack of distinct domains) for sample deposited at high temperature and a less ordered crystalline phase for annealed ones.

Finally, beam damage detected on annealed and high-temperature deposited samples deserves a comment. In fact, in the former case repeated displacements on oxide surface during measurements were needed to avoid spectra modifications caused by X-ray light used as a probe. On the contrary, results acquired from $TiO_2$ synthesized at 355°C proved to remain considerably more stable even after photon exposure of about one hour.
This fact provides interesting hints to create a suitable deposition technique for the fabrication of robust materials for solar devices.

### 5.2.4 Conclusion on $TiO_2$

Titanium oxide proves to have a more complex behavior than $MoO_x$ at high temperatures. Even if the small amount of XPS/UPS measurements prevents any conclusive answer about work function changes and oxide reduction, LEEM data suggest that WF increases during annealing over 350°C, but not when the same high temperature is set during deposition. This gives interesting indications to develop suitable growth and post-growth treatments.

Even if the topography analyzed by AFM did not change after heating - a fact that is probably linked to the ITO substrate, the numerous domains appearing on the surface are likely to be due to different crystalline reconstruction: $TiO_2$ evolves from amorphous to anatase phase, but with various long and short range patterns accounting for emission intensity heterogeneity on the sample and for $Ti2p_{3/2}$-$e_g$ sub-peak shape. This is the reason why the expression *domains of polycrystallites* was used throughout the previous discussion: regions with different emission properties and probably different crystalline reconstructions detected by XPEEM and XAS measurements have an extension of the order of several micrometers (∼10 $\mu$m), but they are likely to consist of nanometric grains as those revealed by AFM (∼30 nm), which do not show in their morphology the domains they belong to.

In order to achieve a deeper control of $TiO_2$-based device fabrication it is therefore crucial to understand in further studies the origin of different crystalline domains revealed by the presented measurements and the properties they can provide as well as the different effects of beam damage determined on annealed and high-temperature deposited samples.

# Chapter 6

# General conclusion and perspectives

The ensemble of data collected on $MoO_x$ and $TiO_2$ illustrated in this thesis shed light on the properties of these oxides and on how they can be exploited in organic or hybrid photovoltaics.

For both materials work function changes induced by annealing is confirmed: this thermal treatment effect on energy bands is especially useful in the case of $MoO_x$ for designing hole-extracting layers, which need oxide Fermi level pinning to organic semiconductor HOMO to assist the flow of positive charges. XPS and UPS data on this compound also demonstrate its reduction during thermal treatment and the improvement of conduction properties with the filling of defect states - two important characteristics in solar cells and other electronic devices. Nevertheless, it is crucial that O-vacancy defect states appearing below conduction band with annealing do not expand beyond it: in fact, if oxide Fermi energy enters CB and the material shows a metallic character, the hole-selective properties of $MoO_x$ could be destroyed and short-circuits could appear inside the solar device.

Another remarkable result of this research is about the influence of the substrate on structure reconstruction during annealing. In fact, $MoO_x$ deposited on silicon proves to evolve both in crystal grain size and in surface work function, whereas oxides grown on ITO maintain their structural properties almost constant while work functions vary. Further studies are therefore needed to understand interactions between TMOs and their deposition layers, focusing in particular on substrates that can be employed in organic solar cell engineering - in this regard data on silicon are not as interesting for applications as those on conductive ITO.

Moreover, experimental results suggest that deposition techniques and thermal treatments determine different materials properties. For example, high temperature annealed and sputtered molybdenum oxides show an improved stability under UV light - an advantage for OPV, whereas work function of $TiO_2$ deposited at elevated temperature does not substantially change in the observed temperature range as in the case of annealed oxide and it is more stable to beam damage.

Follow-up research is also needed to analyze the properties of crystalline domains that arise during annealing on titanium oxide surface - but not on $MoO_x$. They do not seem to derive from macroscopic morphology, according to AFM data, but are likely to be linked to atomic symmetries developed during the phase transition from amorphous to anatase phase at high temperature.

In this context, different experimental techniques are requested to study the properties of these materials with a better resolution, beyond the one attained by XPEEM

(∼100 nm). For example, further diffraction studies with $\mu$m-beam size could be promising to discover molecular order in oxide structures.

However, the main result of this research is related to the possibility of tailoring electrical properties of Transition Metal Oxides by simple thermal treatments. It is therefore essential to continue studying these materials to reach deeper understanding of their crystalline and energy band structure, to get full control on them and to discover which characteristics are the most suitable for photovoltaic applications.

# Bibliography


[1] M.T. Greiner, Z.-H. Lu. *Thin-film metal oxides in organic semiconductor devices: their electronic structures, work functions and interfaces.* NPG Asia Materials (2013) 5.

[2] M.T. Greiner *et al. Transition Metal Oxide Work Functions: The Influence of Cation Oxidation State and Oxygen Vacancies.* Adv. Funct. Mater. 22 (2012) 4557-4568.

[3] C.L. Chen *et al. Electronic properties of free-standing $TiO_2$ nanotube arrays fabricated by electrochemical anodization.* Phys. Chem. Chem. Phys., 17 (2015) 22064.

[4] J. Liu *et al.. $TiO_2$ Nanotube Arrays for Photocatalysis: Effects of Crystallinity, Local Order and Electronic Structure.* BNL JA 108391 (2015).

[5] A.L.F. Cauduro *et al.. Work function mapping of $MoO_x$ thin-films for application in electronic devices.* Ultramicroscopy 000 (2017) 1-5.

[6] A.L.F. Cauduro, L. Bossard-Giannesini, H. Cruguel, N. Witkowski *et al.. Crystalline Molybdenum Oxide Thin-Films for Application as Interfacial Layers in Optoelectronic Devices.* ACS Mater. Interfaces 9 (2017) 7717-7724.

[7] H. Lee *et al.. Interfacial electronic structure for high performance organic devices.* Current Applied Physics 16 (2016) 1533-1549.

[8] *Solar Cell Parameters and Equivalent Circuit.* https://ocw.tudelft.nl/wp-content/uploads/solar_energy_section_9_1_9_3.pdf

[9] A. Wilke *et al.. Correlation between interface energetics and open circuit voltage in organic photovoltaic cells.* Appl. Phys. Lett. 101 (2012) 233301.

[10] P. Kofstad. *Approximate correlation between heats of formation of cation and oxygen vacancies and thermochemical properties of oxides.* J. Phys. Chem. Sol.28 (1967) 1842.

[11] G. Campet *et al. Electronegativity versus Fermi energy in oxides: the role of formal oxidation states.* Mater. Lett. 58 (2004) 437.

[12] A. Stevanovic *et al.. Photoluminescence of $TiO_2$: Effect of UV Light and Adsorbed Molecules on Surface Band Structure.* J. Am. Chem. Soc. 134 (2012) 324-332.

[13] G. Xiong *et al.. Photoemission Electron Microscopy of $TiO_2$ Anatase Films Embedded with Rutile Nanocrystals.* Adv. Funct. Mater. 17 (2007) 2133-2138.

[14] M. Ahmadpour. *Metal-Oxide Based Interlayers for Organic and Perovskite Photovoltaics.* PhD thesis, University of Southern Denmark (2017).

[15] W. Melitz *et al.*. *Kelvin probe force microscopy and its application.* Surface Science Reports 66 (2011) 1-27.

[16] L. Aigouy *et al.*. *Les nouvelles microscopies. À la découverte du nanomonde.* Belin, ch. 2.

[17] Bruker. *AFM Nanoscope user guide.* Application Note number 140. *PeakForce Kelvin Probe Force Microscopy.*

[18] Bruker. *PeakForce Tapping.* https://www.bruker.com/products/surface-and-dimensional-analysis/atomic-force-microscopes/modes/modes/imaging-modes/peakforce-tapping/overview.html

[19] B. Pittenger. *Nondestructive characterization of advanced polymeric materials using spectroscopy and atomic force microscopy.* https://www.bruker.com/fileadmin/user_upload/8-PDF-Docs/SurfaceAnalysis/AFM/Webinars/20150323C_ENwebinar.pdf

[20] L. Aballe, M. Foerster. *Working principles of LEEM-PEEM.* https://indico.cells.es/indico/event/24/session/2/contribution/1/material/slides/0.pdf.

[21] A. Nilsson *et al.*. *X-ray absorption spectroscopy and X-ray Raman scattering of water and ice: an experimental view.* Journal of Electron Spectroscopy and Related Phenomena 177 (2010) 99-129.

[22] P. Klapetek *et al. Gwyddion user guide.* http://gwyddion.net/documentation/user-guide-en/editing-correction.html

[23] P. Klapetek *et al. Gwyddion user guide.* http://gwyddion.net/documentation/user-guide-en/statistical-analysis.html

[24] W.M.H. Sachtler *et al. The work function of gold.* Surface Science 5 (1966) 221-229.

[25] B. Han *et al. Effect of post-annealing on the properties of thermally evaporated molybdenum oxide films: Interdependence of work function and oxygen to molybdenum ratio.* Materials Science in Semiconductor Processing 75 (2018) 166-172.

[26] A.L.F. Cauduro. *Growth, Properties and Applications of $MoO_x$ Thin-Films.* PhD thesis, University of Southern Denmark (2016).

[27] D. Briggs, M.P. Seah. *Practical Surface Analysis, Auger and X-ray Photoelectron Spectroscopy.* John Wiley & Son (1990).

[28] B. Ünal *et al.*. *Work function of a quasicrystal surface: Icosahedral Al-Pd-Mn.* J. Vac. Sci. Technol. A 27 (2009) 1249.

[29] F. Borgatti. *Photoelectron Spectroscopy.* University of Bologna (2016).

[30] *HybriD Mode. Rebirth of Force Spectroscopy: Advanced Nanomechanical, Electrical, Optical, Thermal and Piezoresponse Studies.* https://www.ntmdt-si.com/data/media/files/products/brochures/HybriD_Mode/Brochure_HybriD_A4_en.pdf

# Appendix A

# Peak Force and Surface Potential KPFM Tapping mode and Potential Offset in surface work function measurements

Within the context of KPFM analyses, it is also interesting to compare images acquired using different microscopy modes. In addition to Peak Force KPFM-AM, also standard Tapping mode (AM Surface Potential) was employed for XPS2 sample annealed at 500°C. Set parameters were the same for the two series of measurements: a lift scan height of 50 nm, a scan rate of 1 Hz and 512 samples per line. To exploit another possibility offered by KPFM technique, a potential offset was also applied to the tip during the scan. It is thus useful to compare the results of all acquisition parameter combinations: Peak Force (PF) or Surface Potential (SP) mode with or without potential offset. Since the mean potential level was ∼-150 mV for Peak Force mode, the chosen offset was -150 mV, whereas it was +150 mV for Surface Potential mode, whose image had a mean potential of ∼+150 mV.

As done to calculate height roughness and potential contrast in section 5.1.1, two images were recorded with the same mapping conditions (only one of them is showed in figure (A.1)) and six profiles were extracted both from topography and from potential data: the most representative grain boundaries were chosen. All the steps were analyzed to calculate their height (vertically in nanometer or millivolt scale, called $\Delta z$) and their steepness (the horizontal distance separating the lowest and the highest profile points, called $\Delta x$). Since all these quantities are differences between two positions, their associated error is twice the uncertainty of every point (typically two divisions in the vertical scale and half of a division in the horizontal due to the different level of fluctuation in the profiles). Finally, the weighted average of the six measures was calculated, together with its error.

The significant parameter to estimate the performance of every topography and potential acquisition mode is the *resolution*, defined as

$$\frac{\Delta z}{\Delta x},$$

expressed respectively as a dimensionless quantity or in mV/nm. Its associated uncer-

| | Potential offset = 0 | Potential offset = ±150 mV |
|---|---|---|
| PF | Top. = (1.3±0.5); Pot. = (0.18±0.04)mV/nm | Top. = (1.2±0.5); Pot. = (0.24±0.08)mV/nm |
| SP | Top. = (0.9±0.3); Pot. = (0.1±0.2)mV/nm | Top. = (0.8±0.3); Pot. = (0.11±0.18)mV/nm |

Table A.1: Topography and potential resolutions calculated for Peak Force and Surface Potential Tapping modes, with and without the application of a potential offset.

tainty was calculated according to propagation of error as

$$\frac{\Delta z}{\Delta x}\sqrt{(\frac{\Delta(\Delta z)}{\Delta z})^2+(\frac{\Delta(\Delta x)}{\Delta x})^2},$$

where $\Delta(\Delta z)$ and $\Delta(\Delta x)$ are the estimated errors for $\Delta z$ and $\Delta x$, respectively.

Figure A.1 shows the images recorded with the different techniques and table A.1 summarizes the resolution results. In particular some conclusions can be drawn:

1. The application of a potential offset does not change the acquisition resolution nor the image quality (results are consistent considering the error bars).

2. According to theoretical expectations, classic Tapping mode provides a lower resolution and this fact is especially evident in potential maps, whereas for topography Surface Potential performance is worse but consistent with Peak Force one.

3. As can be seen in figure A.2, the most important difference in resolution is noticeable in potential steps. In the Surface Potential case (figure A.2d) the fluctuation in the profile forced us to consider a greater error than some scale divisions (typically 10 mV for every point in the vertical scale and 100 nm in the horizontal). Therefore the calculated resolution implies an extremely wide error bar (wider than the resolution itself, see table A.1).

4. CPD levels are reversed in the two modes: this makes more difficult a comparison between sample work functions.

It was thus decided not to apply any potential offset, due to the slight changes recorded, and to use Peak Force KPFM maps in data processing in order to achieve better resolution and color map readability, especially in potential images.

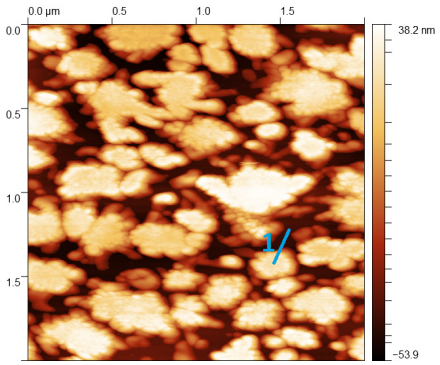


(a) *Peak Force topography with the indication of the profile analyzed in figure A.2; no potential offset; color scale ranges from -53.9 nm (black) to 38.2 nm (white).*

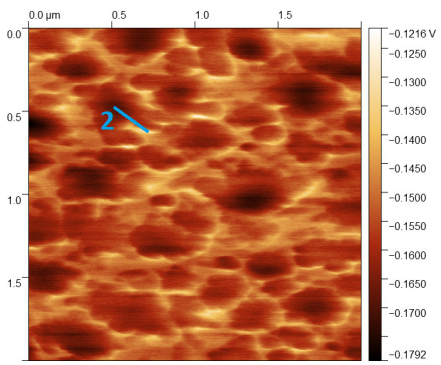


(b) *Peak Force potential with the indication of the profile analyzed in figure A.2; no potential offset; color scale from -179.2 mV (black) to -121.6 mV (white).*

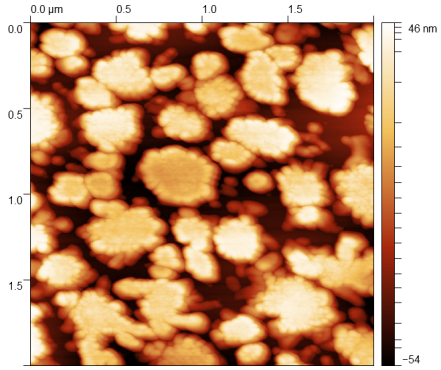


(c) *Peak Force topography; potential offset = -150 mV; color scale from -54 nm (black) to 46 nm (white).*

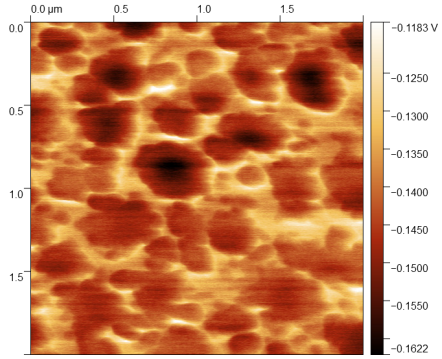


(d) *Peak Force potential; potential offset = -150 mV; color scale from -162.2 mV (black) to -118.3 mV (white).*

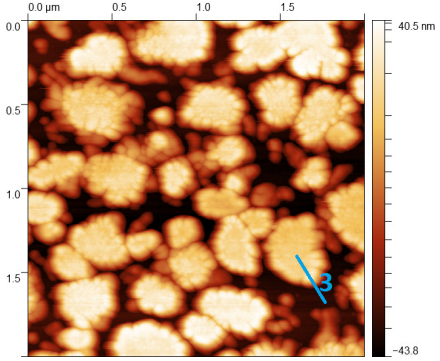


(e) *Surface Potential topography with the indication of the profile analyzed in figure A.2; no potential offset; color scale from -43.8 nm (black) to 40.5 nm (white).*

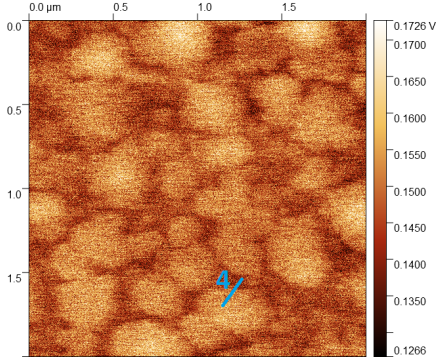


(f) *Surface Potential potential with the indication of the profile analyzed in figure A.2; no potential offset; color scale from 126.6 mV (black) to 172.6 mV (white).*

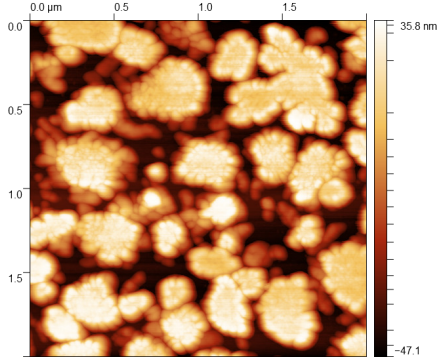


(g) *Surface Potential topography; potential offset = 150 mV; color scale from -47.1 nm (black) to 35.8 nm (white).*

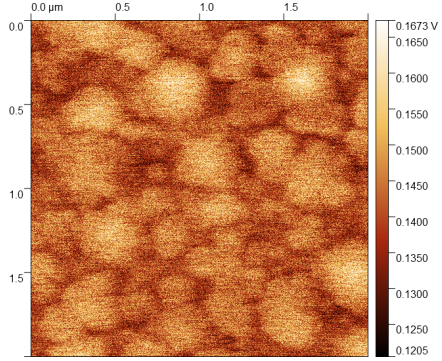


(h) *Surface Potential potential; potential offset = 150 mV; color scale from 120.5 mV (black) to 167.3 mV (white).*

Figure A.1: Comparison between 2 $\mu$m $\times$ 2 $\mu$m topography and potential maps acquired in Peak Force and Surface Potential KPFM modes with and without potential offset (XPS2 sample annealed at 500°C).

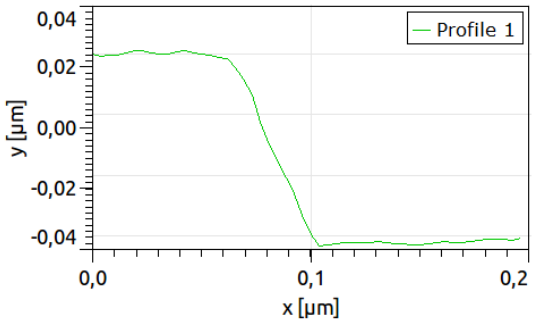


(a) *Peak Force topography profile referred to the line traced on image A.1a.*

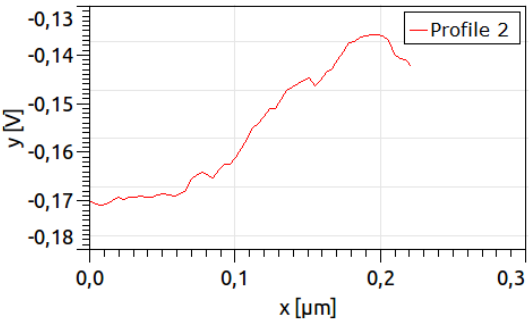


(b) *Peak Force potential profile referred to the line traced on image A.1b.*

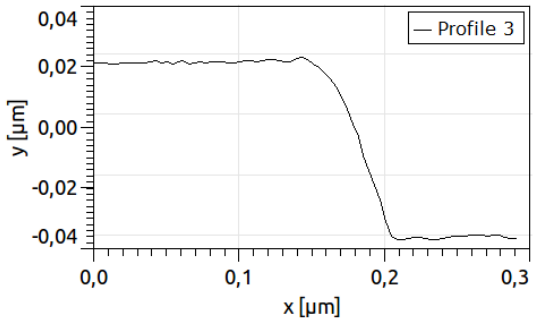


(c) *Surface Potential topography profile referred to the line traced on image A.1e.*

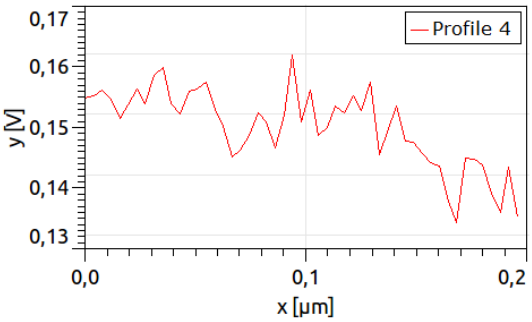


(d) *Surface Potential potential profile referred to the line traced on image A.1f.*

Figure A.2: Topography and potential profiles acquired in Peak Force and Surface Potential KPFM modes without potential offset (XPS2 sample annealed at 500°C).

# Appendix B

# Boundary effects and adhesion properties in KPFM maps

After understanding how the annealing cycles induce crystallization and formation of surface aggregates, an interesting question about the chemical composition of these grains should be faced. In fact, a comparison between topographical and potential images reveals that sample features in both maps are similar and so that work function differences between surface grains and the substrate are suggested. Can these results be influenced by boundary artifacts? In fact, tip-sample interaction producing potential KPFM images involves capacitive effects when the tip scans a step between grains and substrate. Moreover, the topography of the sample determines a specific distribution of surface charges that can affect electrical interaction during measurements - for example, valleys can act as 'mechanical traps' for electrons.

In order to understand better physical and chemical characteristics of the materials under examination, adhesion KPFM maps were also analyzed. This property is mapped during a scan as the force needed to get the tip 'unstuck' after an approach to the surface. It is measured as the difference between the approach and the withdraw in the potential applied to the tip in the feedback loop[30]. Adhesion gives a qualitative image of chemical composition of surface features, because different compounds on the sample differently interact with the tip, even if adhesion could also be influenced by water particles trapped during a scan.

An example of this analysis is shown in figure B.1, referred to substoichiometric $MoO_x$ on ITO annealed at 500°C (sample XPS1 as referred to throughout this thesis). As explained in paragraph 5.1.1, topography and potential average roughness were extracted from KPFM images taking into account only medium-sized grains and the corresponding features in CPD maps (orange in the color map of fig. B.1). However, also higher peaks are visible on the surface (∼90 nm vs. ∼40 nm of height roughness in the present example) and they are associated with lower potential regions (∼25 mV vs. ∼17 mV of potential roughness). Whereas ordinary grains can be detected in adhesion map too (figure B.1c), shape and size of the highest nanoaggregates (light yellow) are recognizable there, but their adhesion level is the same as other grains (similar colors). This could mean that the peculiar features appearing after 500°C annealing are only due to crystallization process that leads to an increasing level of clustering on the surface, but without changing oxide chemical composition. From this set of images (figure B.1) it is however challenging to detect real chemical differences between surface grains and the substrate to support the hypothesis of different crystallization between them[6].

About this fact, in paragraph 5.1.1 it was specified that during image analysis and profile extraction only roughness referred to grain cores was measured. In fact, it is true that boundary regions are often affected by convolution effects: the tip interacts both with the substrate and with grains so that the recorded height and CPD level are not the real ones. In the case of adhesion, edge regions could show specific interaction properties because, for example, it is easier for the tip to release moisture molecules at the borders, where they are pinned down by fewer similar particles and morphological 'trapping' structures. This could be seen, for instance, in XPS2 annealed at 500°C shown in figure B.2, where edge zones prove to be stiffer in adhesion maps (darker in figure B.2c). Even if a qualitative inspection of the image reveals the presence of regions of different color at grain borders in topography and adhesion maps, these 'boundary' regions are far more extended in potential image (a CPD dark brown or black area in the middle of the grain can only be seen in wider aggregates): this fact could be interpreted as a demonstration of boundary artifacts and of the importance of performing roughness measurements reasonably far from the borders and only on wide grains. In fact, in addition to the specific characteristics of every interaction (van der Waals, adhesion force, electrical interactions) resulting in different resolutions, in topography and adhesion acquisition the tip makes a closer approach to the surface and convolution affects smaller regions, whereas during the lift scan (CPD mapping) the more retracted tip experiences grain and substrate cross-talk effects on wider regions. These observations suggest that for roughness and CPD calculations small grains (for example, those with a diameter of less than a hundred nanometers for potential map in figure B.2b) should not be considered: they are so narrow that all their area is affected by boundary effects so that they are below the resolution limit of the method.

In general, we can therefore conclude that, except for border regions where capacitive and convolution artifacts prevent a rigorous measurement of sample properties (especially concerning potential), grains formed after annealing are chemically homogeneous and the main chemical difference on sample surface is between the aggregates and the substrate. Nevertheless, as shown by the majority of the acquired maps like the one in figure B.2c, all the grains emerging on the surface have roughly the same adhesion properties as the substrate, so that no information in support of oxide crystallization (as presented in ref. [6]) could be extracted. In any case, this is not a conclusive interpretation, since different $MoO_x$ stoichiometries do not necessarily exhibit different adhesion properties - which are significantly linked to adsorbate presence due to topography - and since the real highly-crystalline 'substrate' may not be directly identified with the lowest regions in surface topography. Moreover, the carbon contamination and the presence of moisture affecting KPFM on air should be taken into account.

It is important to underline that, even if mapping adhesion force allows to investigate chemical properties on the surface with a good resolution, only qualitative information can be extracted from these images, so that other complementary techniques as XPS and XPEEM are fundamental in order to understand which compounds and crystalline phases the sample is made of and how they evolve during annealing.

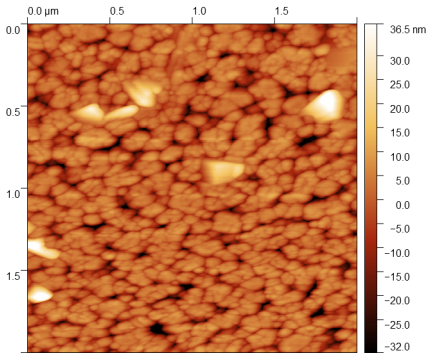


(a) *Color scale from -32.0 nm (black) to 36.5 nm (white).*

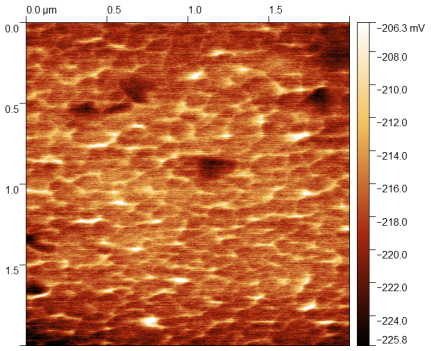


(b) *Color scale from -225.8 mV (black) to -206.3 mV (white).*

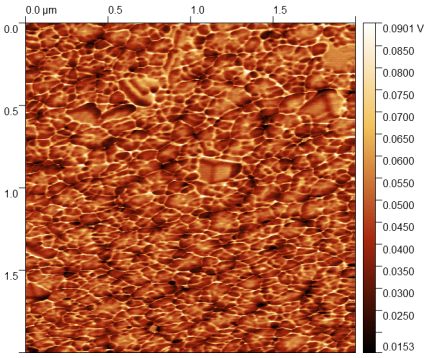


(c) *Color scale from 15.3 mV (black) to 90.1 mV (white).*

Figure B.1: KPFM images of XPS1 $MoO_x$ on Si annealed at 500°C (size: 2 $\mu$m × 2 $\mu$m): topography (a), potential (b) and adhesion (c) maps.

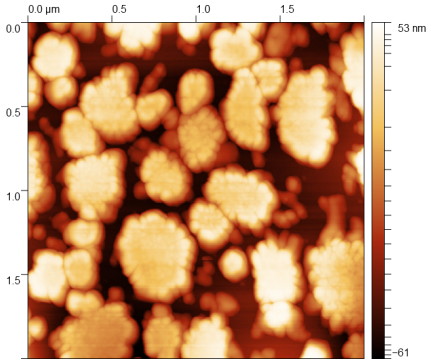


(a) *Color scale from -61 nm (black) to 53 nm (white).*

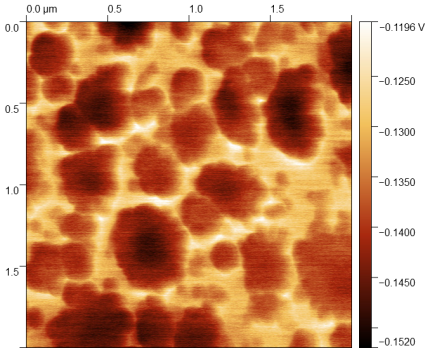


(b) *Color scale from -152.0 mV (black) to -119.6 mV (white).*

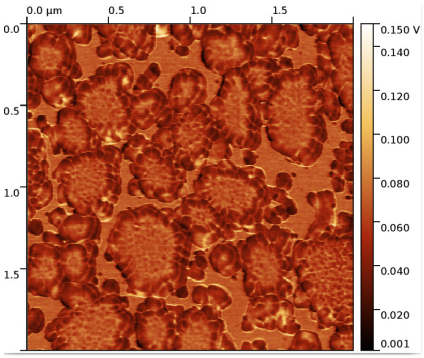


(c) *Color scale from 1 mV (black) to 150 mV (white).*

Figure B.2: KPFM images of XPS2 $MoO_x$ on Si annealed at 500°C (size 2 $\mu$m $\times$ 2 $\mu$m): topography (a), potential (b) and adhesion (c) maps.